Thesis

Geometrical Responses in Topological Materials

Hiroaki Sumiyoshi

Department of Physics, Kyoto University

December, 2016

Abstract

Recent both theoretical and experimental studies have revealed that topological materials such as topological insulators and superconductors, graphene, and Weyl semimetals exhibit characteristic transport properties associated with the geometrical structures of the wave functions of the electrons in the real and momentum spaces. In addition to applying electromagnetic fields, these responses are also caused by external forces, such as applying a temperature gradient, twisting the sample, making dislocations in the lattice. Theoretically, they are described by the technique of the differential geometry. Based on these backgrounds, in this work, we theoretically, studied two geometrical transport phenomena in topological materials, using this technique.

First, we study the thermal Hall effect in superconductors with broken time-reversal-symmetry. The thermal Hall effect is the thermal analog of the Hall effect and the production of a temperature gradient by the transverse temperature gradient. This effect is useful for detecting the topological feature of the superconductors rather than the Hall effect, since the number of electrons is not conserved and then electromagnetic responses hardly grasp it. We derive a formula for the thermal Hall coefficients, represented by the Berry curvature of the Bogoliubov-de Gennes Hamiltonian. We also applied it to two-dimensional chiral superconductors, and found that in the low temperature limit, the thermal Hall coefficients are quantized as, $\kappa_{xy} = c\pi T/6$, where c is one-half of the bulk Chern number defined from the Bogoliubov-de Gennes Hamiltonian and corresponds to the central charge of the Majorana edge mode. It reproduces the result of a previous study based on edge calculations. Moreover it can be applied to any superconductors even with nodes including Weyl superconductors, and therefore useful for exploring broad types of topological materials.

Second, we propose a new topological response, referred to as the torsional chiral magnetic effect, in Weyl semimetals. Weyl semimetals are materials that are charac-

terized by one or more pairs of Weyl cones protected by topological numbers. Various exotic transport phenomena associated with the chiral anomaly, which is one of the most important features of Weyl semimetals, have been theoretically predicted and some of them have been observed in experiments. Among them the chiral magnetic effect has been discussed in broad areas of physics, including nuclear and nonequilibrium physics. It is the generation of a ground state current in the presence of a magnetic field even without an electric field. The theories of this effect contain subtle points: it can be derived based on the linearized effective field theory but its no-go theorem in solid state electron systems was proved. On the other hand, the torsional chiral magnetic effect is the generation of a ground state current due to emergent magnetic fields arising from an edge or screw dislocation line. We investigate it by the linear response theory based on a linearized effective model with background geometry. We, furthermore, perform a numerical calculation based on a tight-binding model of Weyl semimetals with a dislocation, and establish that this effect is indeed possible even in realistic solid state systems, in sharp contrast to the chiral magnetic effect due to a magnetic field. We also discuss how it avoids the no-go theorem. We also propose experimental setups for the detection of this novel effect.

This thesis is organized as follows. In Chapter 1 we describe the overview of the topological materials, topological superconductors, Weyl semimetals and Weyl superconductors. In Chapter 2 we review the theory of the differential geometry and application to condensed matter systems. Our results on the thermal responses in superconductors with broken time-reversal-symmetry are presented in Chapter 3. A theory on a new topological response in Weyl semimetals caused by dislocations, i.e. the torsional chiral magnetic effect, is developed in Chapters 4. Chapter 5 is dedicated to the conclusion of this thesis on geometrical responses in topological materials.

Contents

Abstract **1**

List of publications **5**

1 Introduction: topological superconductors, and Weyl semimetals and superconductors **6**

1 Topological superconductor with broken time-reversal symmetry 7

2 Weyl semimetals and superconductors 8

2 Geometrical response in condensed matter physics **21**

1 Differential geometry 21

2 Emergent geometry in condensed matter systems 27

3 Geometrical response in topological systems 37

4 Summary and motivations of our studies 54

3 Bulk approach for the thermal Hall effect in time-reversal-symmetry broken superconductor **56**

1 Model, symmetry, and preliminaries 58

2 Energy current operator 60

3 Thermal Hall conductivity 63

4 Summary 66

4 Torsional chiral magnetic effect in a Weyl semimetal with a topological defect **67**

1 Linear response theory based on field theory in curved space-time . . . 67

2 Spectral asymmetry and ground state current in the presence of screw dislocation 72
3 Numerical calculation 74
4 Comment on no-go theorem of the chiral magnetic effect 77
5 Experimental implications 79
6 Summary 82
7 Appendix: Derivation of torsional responses from linear response theory 82
8 Appendix: Analytical calculation on ground state current in the presence of screw dislocation 88

5 Conclusion **92**

Acknowledgment **100**

List of publications

Published papers related to the thesis

1. Hiroaki Sumiyoshi and Satoshi Fujimoto
   Quantum Thermal Hall Effect in a Time-Reversal-Symmetry-Broken Topological Superconductor in Two Dimensions: Approach from Bulk Calculations
   J. Phys. Soc. Jpn. **82**, 023602 (2013).

2. Hiroaki Sumiyoshi and Satoshi Fujimoto
   Torsional Chiral Magnetic Effect in a Weyl Semimetal with a Topological Defect
   Phys. Rev. Lett. **116**, 166601 (2016).

Published papers not included in the thesis

3. Hiroaki Sumiyoshi and Satoshi Fujimoto
   Giant Nernst and Hall effects due to chiral superconducting fluctuations
   Phys. Rev. B **90**, 184518 (2014).

4. T. Yamashita, Y. Shimoyama, Y. Haga, T. D. Matsuda, E. Yamamoto, Y. Onuki, H. Sumiyoshi, S. Fujimoto, A. Levchenko, T. Shibauchi, and Y. Matsuda
   Colossal thermomagnetic response in the exotic superconductor URu_2Si_2
   Nat. Phys. **11**, 17 (2015).

5. Yohei Ibe and Hiroaki Sumiyoshi
   Chiral Magnetic Effect due to Inhomogeneous Magnetic Fields in Noncentrosymdmetric Weyl Semimetals
   arXiv 1605.04567 (2016).

Chapter 1

Introduction: topological superconductors, and Weyl semimetals and superconductors

This thesis is on "geometrical" responses in topological materials. As widely known, the theory of the differential geometry is an useful mathematical technique for the description of the effect of gravity in high-energy physics. Also in condensed matter physics, this theory is useful for the description of geometrical responses: e.g. the thermal response or responses caused by lattice dislocations, rotation, or twist. Moreover, applying it to topological materials such as integer and fractional quantum Hall states (IQHSs and FQHSs), topological insulators and superconductors (TIs and TSCs), graphenes, and Weyl semimetals (WSMs). Recent both theoretical and experimental works have revealed their rich and exotic transport properties. In this thesis, we especially argue the thermal Hall effect (THE) in superconductors with broken time-reversal-symmetry, and propose new transport phenomena in WSMs caused by dislocations.

In the following sections in this chapter, we review the topological materials, TSCs, WSMs, and WSCs. We also give the summary on theory of the differential geometry and their applications to condensed matter systems in the next chapter.

1 Topological superconductor with broken time-reversal symmetry

The bulk energy spectra of the TIs and TSCs are fully gapped. However, they are distinguished from trivial systems such as normal insulators and fully gapped normal superconductors by integer topological numbers, and, without closing the gapes, cannot be adiabatically deformed into trivial systems. The classification of possible TIs or TSCs in any dimensions and with three types of local symmetries is given in Ref.[1]. In this section we review the TSCs that are classified as two-dimensional class C and D TSCs in this classification, which have particle-hole symmetry but break time-reversal-symmetry.

These TSCs are characterized by the first Chern number or TKNN number [2] defined from the Bloch wave functions of the Bogoliubov-de Gennes (BdG) Hamiltonian in the occupied bands. On the edge of the system, there are chiral gapless edge modes, the number of which is equal to the bulk TKNN number. These properties are very similar to those of the Chern insulators (CIs), which are classified as the class A TIs (Fig.1.1). However, there are crucial differences in the elementary excitations and transport properties. Indeed, the elementary excitation of the TSCs is the excitation of the Bogoliubov quasiparticles in the edge chiral Majorana modes and the creation of this quasiparticles is equivalent to the annihilation of them as

$$\gamma_k^\dagger = \gamma_{-k}, \tag{1.1.1}$$

and then the quasiparticles at low energy are charge neutral and cannot by excited by electric field. Therefore electromagnetic response hardly grasps the topological nature of the TSCs unlike the CIs, and in this thesis we discuss the thermal transport, which is described by the theory of geometry as mentioned in Chapters 2 and 3.

At the end of this section, we review possible candidate materials of the TSCs with broken time-reversal-symmetry. The spineless chiral $p + ip$ superconductors are the two-dimensional class D TSCs, and Sr_2RuO_4 [3], a thin film of ^{3}He A phase[4], and Moore-Read $\nu = 5/2$ fractional quantum Hall states [5] are their candidate systems. The singlet chiral $d + id$ superconductors are that of class C TCSs [1]. Moreover, it is found that, even if the superconducting pairing is the trivial s-wave, we can obtain the class D TSCs when the system has strong spin-orbit interaction and Zeeman magnetic

field [6, 7, 8].

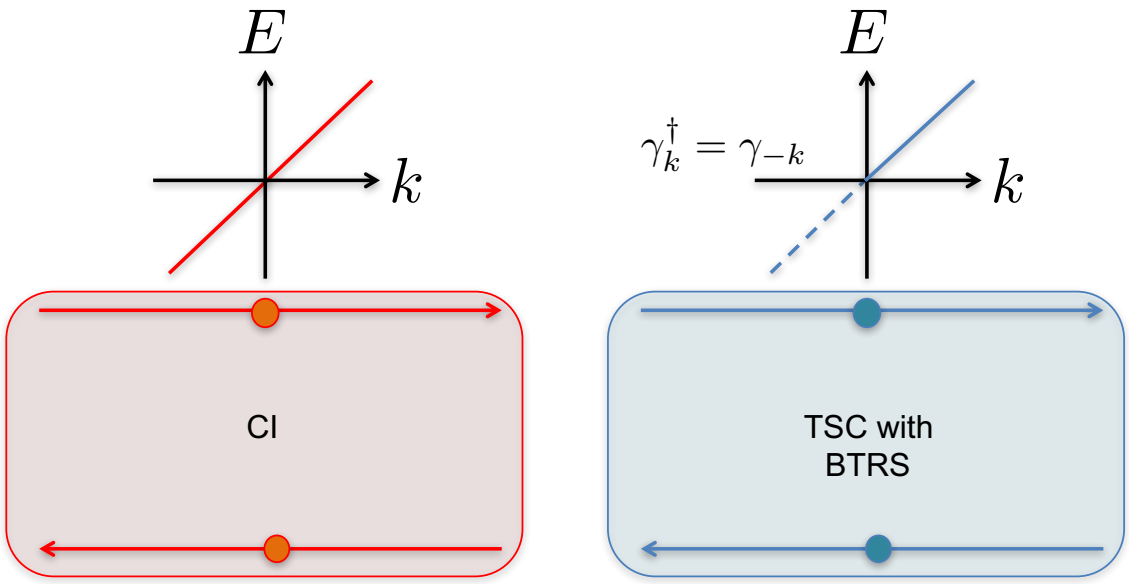

Figure 1.1: CI (left) and TSC with broken time-reversal symmetry (right). Their bulks are fully gapped, but they have chiral and Majorana gapless edge modes, respectively.

2 Weyl semimetals and superconductors

WSMs are three-dimensional materials that have Weyl modes in the Brillouin zone (BZ). The Hamiltonian for a Weyl mode is, around a certain point $\boldsymbol{\lambda} = (\lambda_1, \lambda_2, \lambda_3)$ in the BZ, which is called the Weyl point, given by

$$H_{Weyl}(\boldsymbol{k}) = \sum_{i,j=1,2,3} (k_i - \lambda_i) v_{ij} \sigma_j - \lambda_0, \tag{1.2.1}$$

in the linear order of $(\boldsymbol{k} - \boldsymbol{\lambda})$. Here σ_i is the Pauli matrix, v_{ij} is the velocity matrix, and λ_0 corresponds to the energy shift of the Weyl modes. The Weyl mode has a monopole charge in the momentum space. Indeed, supposing that S is an arbitrary spheres surrounding the Weyl point, the surface integral of the Berry flux through S, which is the Chern number, is quantized as

$$\Phi_S := \frac{1}{2\pi} \int_S \boldsymbol{b} \cdot d\boldsymbol{S} = \chi \in \mathbb{Z}, \tag{1.2.2}$$

where

$$\chi = \mathrm{sgn}[\det(v_{ij})], \tag{1.2.3}$$

is called the chirality of the Weyl mode. Here the Berry curvature is defined by the rotation of the Berry connection as

$$\boldsymbol{b} = \boldsymbol{\nabla} \times \boldsymbol{a}, \tag{1.2.4}$$

and the Berry connection is defined by,

$$\boldsymbol{a} = i \left\langle u \left| \frac{\partial u(\boldsymbol{k})}{\partial \boldsymbol{k}} \right\rangle \right., \tag{1.2.5}$$

where $|u(\boldsymbol{k})\rangle$ is the Bloch wavefunction in the lower band of the Weyl Hamiltonian (1.2.1). The remarkable point is that this monopole charge protects the Weyl node. In other words by weak perturbation without the pair annihilation with a Weyl node with opposite chirality, this node cannot be changed into a gapped mode, which has zero Chern number (see Fig.1.2). [1] In this sense, WSMs are called topological materials, although they are gapless unlike TIs and TSCs. We also comment that in realistic lattice systems a single Weyl node cannot appear alone. Instead, one or more pairs of Weyl nodes with opposite chiralities can appear and the sum of the Chern numbers of all Weyl nodes is always zero following from the Nielsen-Ninomiya's theorem [9, 10].

In this section, we review this topological semimetal, focusing on the characteristic transport phenomena caused by the chiral anomaly. We also comment on WSCs, of which dispersions in the BdG space are the same as those of WSMs.

[1] If there is no node in the region surrounded by S, one Berry connection can be defined over this region. Then, following form the Stokes' theorem, we obtain $\Phi_S = \int_S \boldsymbol{b} \cdot d\boldsymbol{S} = \frac{1}{2\pi} \int_{\partial S} \boldsymbol{a} \cdot d\boldsymbol{l} = 0$. Here, we used that S has no boundary and then $\partial S = \phi$. Therefore, the Chern number of gapped modes are always zero. See also Fig.1.2.

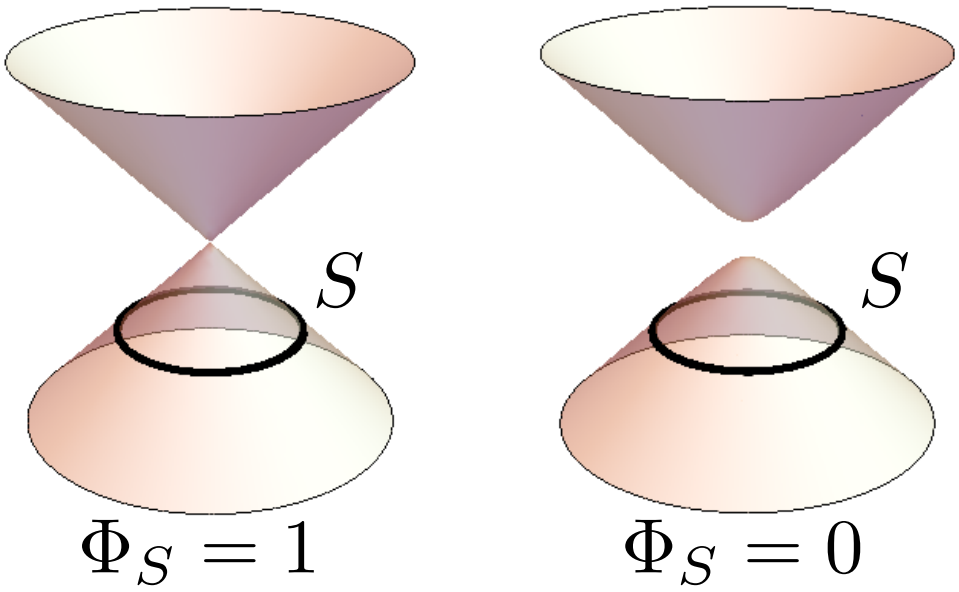

Figure 1.2: Weyl node protected by the topological number. (left) Weyl node, which has the Chern number 1 and (right) gapped state, which has the Chern number 0.

2.1 Chiral anomaly and topological responses

In this subsection, we introduce exotic transport phenomena associated with the chiral anomaly in WSMs: the anomalous Hall effect (AHE), chiral magnetic effect (CME), and negative longitudinal magnetoresistance (NLMR). To see this, we will derive these responses from the chiral anomaly. Now we consider a simple model for a WSM with a gauge potential $A_\mu = (A_0, A_1, A_2, A_3)$, whose Hamiltonian is given by

$$H^{WSM} = \begin{pmatrix} (-i\boldsymbol{\partial} + \boldsymbol{\lambda} + e\boldsymbol{A}) \cdot \boldsymbol{\sigma} - \lambda_0 - eA_0 & 0 \\ 0 & -(-i\boldsymbol{\partial} - \boldsymbol{\lambda} + e\boldsymbol{A}) \cdot \boldsymbol{\sigma} + \lambda_0 - eA_0 \end{pmatrix}. \tag{1.2.6}$$

This model has a pair of Weyl nodes with different chiralities. We supposed that the Weyl points are at $\pm\boldsymbol{\lambda}$ in the BZ and the energy shifts for the Weyl nodes are $\pm\lambda^0$, respectively. Here, $\boldsymbol{\sigma} = (\sigma_1, \sigma_2, \sigma_3)$ are the Pauli matrices. This system is, in terms of the action, represented by

$$S^{WSM}[\bar{\psi}, \psi; A_\mu; \lambda_\mu] = \int d^3x dt \bar{\psi}\gamma^\mu (i\partial_\mu - eA_\mu - \lambda_\mu \gamma^5)\psi, \tag{1.2.7}$$

where γ^μ ($\mu = 0, 1, 2, 3$) are the 4×4 gamma matrices, which satisfy the anticommutation relations $\{\gamma^\mu, \gamma^\nu\} = 2\eta^{\mu\nu}$ with $\eta^{\mu,\nu} = diag(1, -1, -1, -1)$. The definitions of $\bar{\psi}$ and γ^5 are given by $\bar{\psi} = \psi^\dagger\gamma^0$ and $\gamma^5 = i\gamma^0\gamma^1\gamma^2\gamma^3$, respectively. Here we adopted the chiral representation of the gamma matrices:

$$\gamma^0 = \begin{pmatrix} 0 & \mathbf{1}_2 \\ \mathbf{1}_2 & 0 \end{pmatrix}, \tag{1.2.8}$$

$$\gamma^i = \begin{pmatrix} 0 & \sigma_i \\ -\sigma_i & 0 \end{pmatrix} \quad \text{for} \quad i = 1, 2, 3, \tag{1.2.9}$$

where $\boldsymbol{I}_2$ is the 2×2 identity matrix. From this action of the fermion and gauge fields, we define the effective action of the gauge field by the path integration over the fermion fields as

$$e^{iS_{eff}^{WSM}[A_\mu;\lambda_\mu]} = \int \mathcal{D}[\bar{\psi}, \psi] e^{iS^{WSM}[\bar{\psi},\psi;A_\mu;\lambda_\mu]}, \tag{1.2.10}$$

which contains all informations of the electromagnetic responses of this WSM obtained by its variation with respect to A_μ. To calculate S_{eff}^{WSM}, we perform the chiral rotation:

$$\psi = e^{ie\theta(x)\gamma^5/2}\psi', \quad \psi^\dagger = \psi'^\dagger e^{-ie\theta(x)\gamma^5/2}, \tag{1.2.11}$$

with

$$\theta(x) = x^\mu\lambda_\mu. \tag{1.2.12}$$

After the chiral rotation, the action of the WSM, S^{WSM}, becomes that of the Dirac semimetal (DSM), which have a helical massless Dirac mode in the BZ:

$$S^{WSM}[\bar{\psi}, \psi; A_\mu; \lambda_\mu] = S^{DSM}[\bar{\psi}', \psi'; A_\mu], \tag{1.2.13}$$

with

$$S^{DSM}[\bar{\psi}, \psi; A_\mu] = \int d^3x dt \bar{\psi}\gamma^\mu(i\partial_\mu - eA_\mu)\psi. \tag{1.2.14}$$

However, this does not mean that the effective action for the WSM is equal to that for the DSM, since we have to consider the Jacobian of the path integral measure defined by

$$\mathcal{D}[\bar{\psi}, \psi] = \mathcal{J}\mathcal{D}[\bar{\psi}', \psi']. \tag{1.2.15}$$

Calculating $\mathcal{J}$ by using the Fujikawa method [11], we obtain that the difference between the effective actions of the WSM and DSM is given by the θ-term as

$$S_{eff}^{WSM}[A_\mu] = S_{eff}^{DSM}[A_\mu] + S_\theta[A_\mu;\lambda_\mu], \tag{1.2.16}$$

$$S_\theta[A_\mu;\lambda_\mu] = e^2 \int dx^3 dt \frac{\theta(x)}{16\pi^2} \varepsilon^{\mu\nu\rho\lambda} F_{\mu\nu} F_{\rho\lambda}. \tag{1.2.17}$$

Here $S_{eff}^{DSM}[A_\mu]$ is the effective action for the DSM defined by

$$e^{iS_{eff}^{DSM}[A_\mu]} = \int \mathcal{D}[\bar{\psi},\psi] e^{iS^{DSM}[\bar{\psi},\psi;A_\mu]}. \tag{1.2.18}$$

Then the contributions to the charge and current densities of the θ-term is

$$\begin{aligned} j^\mu =& \frac{\delta S[A_\mu;\lambda_\mu]}{\delta A_\mu} \\ =& \frac{e^2}{4\pi^2} \varepsilon^{\mu\nu\rho\lambda} \partial_\nu \theta(x) F_{\rho\lambda}. \end{aligned} \tag{1.2.19}$$

Then, the contribution to the current density is given by

$$\boldsymbol{j} = \frac{e^2}{2\pi^2} \boldsymbol{\lambda} \times \boldsymbol{E} + \frac{e^2}{2\pi^2} \lambda_0 \boldsymbol{B}. \tag{1.2.20}$$

The first and second terms correspond to the AHE and CME, respectively. In the following subsections we will describe their details.

2.1.1 Anomalous Hall effect

The AHE from the first therm of Eq.(1.2.20) is easily understood by the following picture. Suppose that the Weyl points are separated in the z direction as $\boldsymbol{\lambda} = (0, 0, \lambda_z)$ and the energy shifts for the Weyl nodes are 0 as shown in Fig.1.3. The Chern numbers of $k_x k_y$-planes are equal to 1 when the planes are sandwiched by the Weyl points (red plane in Fig.1.3) and 0 otherwise (blue plane in Fig.1.3). Therefore the contribution to the Hall coefficient, σ_{xy}, of a $k_x k_y$-plane is given by

$$\sigma_{xy}(k_z) = \frac{e^2}{2\pi} 1_{\{\lambda_z < k_z < \lambda_z\}}, \tag{1.2.21}$$

where $1_{\{\dots\}}$ is the indicator function, and then the total Hall coefficient is given by

$$\begin{aligned} \sigma_{xy}^{WSM} =& \int_{2\pi/a}^{2\pi/a} \frac{dk_z}{2\pi} \sigma_{xy}(k_z) \\ =& \frac{e^2}{2\pi^2} \lambda_z, \end{aligned} \tag{1.2.22}$$

where a is the lattice constant. This reproduces the first therm of Eq.(1.2.20).

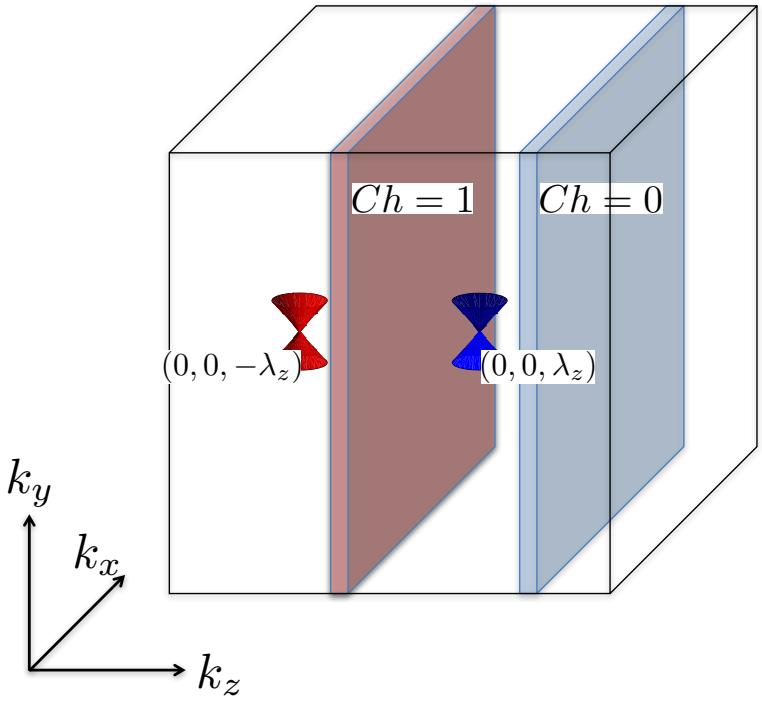

Figure 1.3: BZ of the WSM. The Chern number of a $k_x k_y$-plane is equal to 1 when this plane is sandwiched by the Weyl points (red plane) and 0 otherwise (blue plane).

2.1.2 Chiral magnetic effect and its no-go theorem

The second term of Eq.(1.2.20) represents the CME, which is the generation of current parallel to an applied magnetic field even in the absence of electric fields. [2] This effect was originally considered in the context of the nuclear physics, and expected to play an important role in heavy ion collision experiments [13, 14]. It also caused a stir in nonequilibrium statistical physics, since it leads to the existence of the ground state current which, recently, attracts a renewed interest in connection with the realization of quantum time crystals [15], and then the CME has been studied from this point of view [16, 17]. However, unfortunately, their results are negative for its realization: the macroscopic ground state current in realistic WSMs is always absent, and then

[2] In some papers the chiral anomaly induced negative magnetoresistance described in the next subsection is also referred to as the CME [12]. However, in this thesis we use this terms in the narrow sense, i.e. the generation of ground state current in the absence of electric field.

the CME can never occur for a static and uniform magnetic field. In the following sentences, we will describe the physical picture of the CME and show why it does not work in realistic lattice systems.

We consider a model for inversion-symmetry-broken WSMs (Fig.1.4.a). It has a pair of Weyl nodes of which the Weyl points are at the gamma point in the BZ, but these Weyl nodes have different energy shifts, $\pm\lambda_0$:

$$H = \begin{pmatrix} H_L & 0 \\ 0 & H_R \end{pmatrix} \tag{1.2.23}$$

with

$$H_s = \chi_s(-i\boldsymbol{\partial} + e\boldsymbol{A}) \cdot \boldsymbol{\sigma} - \chi_s\lambda_0, \tag{1.2.24}$$

where $s = L, R$ is the index of the chirality, $\chi_L = 1$ and $\chi_R = -1$, and $\boldsymbol{\sigma} = (\sigma_x, \sigma_y, \sigma_z)$ are the Pauli matrices. Moreover we apply a uniform magnetic field parallel to the z axis, $\boldsymbol{B} = (0, 0, B_z)$, and adopt the gauge $\boldsymbol{A} = (-yB_z/2, xB_z/2, 0)$. Even in the presence of this magnetic field, the momentum in the z direction, k_z, remains a good quantum number. Then the Hamiltonian can be partially diagonalized as

$$H_s = \sum_{k_z} \left[H_s(k_z) - \chi_s\lambda_0\right], \tag{1.2.25}$$

with

$$H_s(k_z) = \chi_s \left[(-i\partial_x + eA_x)\sigma_x + (-i\partial_x + eA_y)\sigma_y + k_z\sigma_z\right]. \tag{1.2.26}$$

Eq.(1.2.26) is coincident with the two-dimensional massive Dirac model with the Dirac mass k_z, and the whole eigenvalues are Landau-quantized as

$$E_s^{\pm n}(k_z) = \pm\sqrt{2\omega_B^2 n + k_z^2}, \quad \text{for} \quad n = 1, 2, 3, \cdots \tag{1.2.27}$$

$$E_s^0(k_z) = \chi_s k_z, \tag{1.2.28}$$

with the cyclotron $\omega_B = \sqrt{eB_z}$ (see, for example, Ref.[18] for the derivation). Here the density of state, or the Landau degeneracy factor, is given by

$$D = \frac{B_z L_x L_y}{2\pi}, \tag{1.2.29}$$

where L_i $(i = x, y, z)$ is the length of the sample in the i-direction. The remarkable point is that the former eigenvalues (1.2.27) have their counterparts as $E_s^{\pm n}(k_z) = -E_s^{\mp n}(k_z)$,

but the later eigenvalue (1.2.28) has no counterpart. This phenomena is called the parity anomaly. Then moving k_z, we obtain the full spectrum for Eq.(1.2.23), which consists of the chiral modes due to the parity anomaly and other symmetric modes as shown in Fig.1.4.b. We can derive the CME immediately form this spectrum. Owing to the symmetry, $E_s^{\pm n}(k_z) = E_s^{\pm n}(-k_z)$, the electrons in these symmetric modes do not contribute to the ground state current in the z-direction, j_z. Then, we focus only on the chiral modes (Fig.1.4.c). We introduce a momentum cutoff as $-\Lambda < k_z < \Lambda$, and then find that there is a difference in the number density of the right-moving and left-moving electrons, [3]

$$\begin{aligned}\Delta n =& \frac{1}{L_x L_y L_z} \sum_{-\Lambda<k_z<-\Lambda+2\lambda_0} D \\ =& \frac{e\lambda_0}{2\pi^2} B. \end{aligned} \tag{1.2.30}$$

Therefore, the grand state current density is

$$\begin{aligned} j_z =& e\Delta n \\ =& \frac{e^2}{2\pi^2}\lambda_0 B \end{aligned} \tag{1.2.31}$$

This reproduces the CME derived from the chiral anomaly, the second term of the right-hand-side of Eq.(1.2.20).

This derivation of the CME was based on the linearized model of WSMs. However, in realistic lattice systems, it does not work. In lattice systems, we have to impose the periodic boundary conduction at the deep inside the Fermi see, $k_z = \pm\pi$, on the band structure as shown in Fig.1.4.d, rather than the momentum cutoff. Generally, we can prove that the net equilibrium current is always absent in lattice systems with arbitrary band structure and at any temperature [16, 17].

Nevertheless, there are chiral anomaly induced transport phenomena in lattice systems other than the AHE. One is the longitudinal negative magnetoresistance (LNMR) described in the next subsection and the other is the generation of local current due to inhomogeneous magnetic field [19] or fictitious magnetic field arising from dislocations (Ref.[20] and Chapter 4).

[3] In this model the Fermi velocity is $v_F = 1$.

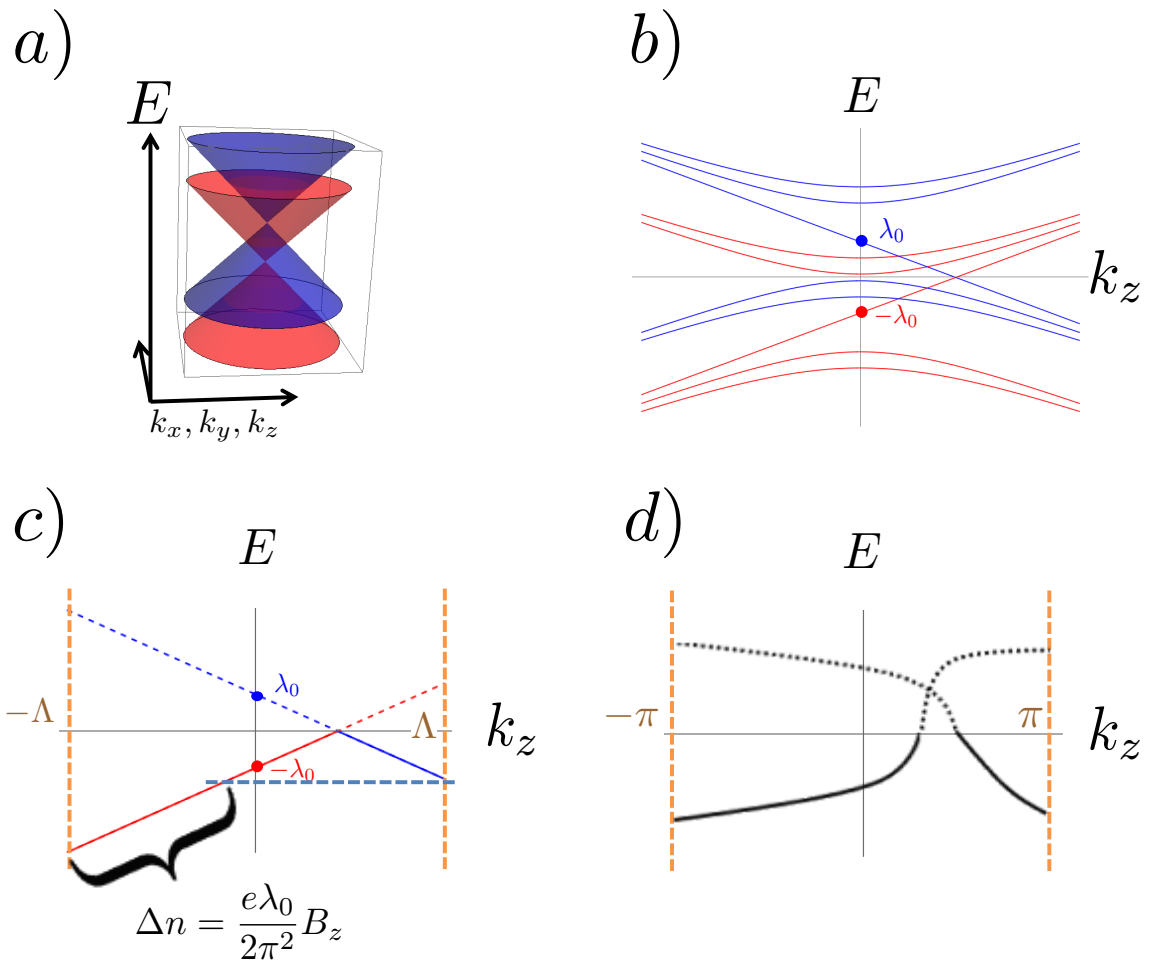

Figure 1.4: a) Band structure of the WSM with broken inversion-symmetry. b) Full spectrum of the WSM in the presence of a uniform magnetic field parallel to the z-axis. c) Chiral modes due to the parity anomaly. d) Band structure of a realistic lattice system. In Figs.c and d, the solid lines and curves represent occupied bands and dashed ones valence bands.

2.1.3 Longitudinal negative magnetoresistance

As shown in the previous subsection, the ground state current cannot occur owing to the periodicity deep inside the Fermi sea in the BZ. However, a chiral anomaly-induced transport phenomena that is donated by the electrons on the Fermi *surfaces* is possible in nonequilibrium states. An example is the longitudinal negative magnetoresistance (LNMR) due to the chiral anomaly, which was theoretically predicted in Ref.[21]. Re-

cently, it has been experimentally observed in many candidate materials for WSMs and DMSs [21, 22, 12, 23, 24, 25]. Here we note that this response can occur in DSMs as well as WSMs.

Now we explain the theory of the LNMR, and introduce magnetoresistance measurements of $Bi_{1-x}S_x$ and TaAs, which are candidate materials for the DSM and WSM, respectively. We consider a WSM or a DMS in the presence of a magnetic field parallel to the z-axis. As discussed in the previous subsection, the spectrum contains D-degenerate right-moving and left-moving chiral modes as shown in Fig.1.5. Here $D = BL_xL_y/2\pi$ (1.2.29). Now, we consider the quantum limit so that only the chiral modes cross the Fermi level, and calculate the conductivity using the Boltzmann equation. Here, we assume that the Fermi velocities for these modes are given by $\pm v_F$, respectively, and (k_z, R) and (k_z, L) indicate the electron with the wave number k_z in the right-moving and left-moving modes, respectively. Then the semiclassical equation is given by

$$\dot{z} = (-\chi_s)v_F, \quad \dot{k_z} = eE_z \tag{1.2.32}$$

where $\chi_L = +1$ and $\chi_R = -1$. Therefore the Boltzmann equation for the semiclassical distribution function, $f(k_z, s, z, t)$ is given by [26]:

$$\frac{\partial f(k_z,s,z,t)}{\partial t} + (-\chi_s v_F)\frac{\partial f(k_z,s,z,t)}{\partial z} - eE_z\frac{\partial f(k_z,s,z,t)}{\partial k_z} = I_{coll}[f], \tag{1.2.33}$$

where the right-hand-side is the collision term. Here we use the relaxation-time approximation

$$I_{coll}[f] = -\frac{f(k_z,s,z,t) - f_0(k_z,s)}{\tau}, \tag{1.2.34}$$

where f_0 is the Fermi distribution function and τ is the relaxation time. At $t \gg \tau$, the solution for this equation is given by

$$\bar{f}(k_z,s) = f_0(k_z,s) - e\tau E_z\frac{\partial f_0(k_z,s)}{\partial k_z}. \tag{1.2.35}$$

Therefore the contribution to the current is

$$\begin{aligned} J_z =& \sum_{k_z,s}(-e\chi_s v_F)\bar{f}(k_z,s) \\ =& \frac{e^2\tau v_F L_z}{2\pi}E_z \end{aligned} \tag{1.2.36}$$

at zero temperature. Moreover, assuming that the D-degeneracy of the chiral modes contribute to the conductivity equally, we obtain that the current density is

$$j_z = \sigma_{zz} E_z, \tag{1.2.37}$$

with

$$\sigma_{zz} = \frac{e^3 \tau v_F}{(2\pi)^2} B_z. \tag{1.2.38}$$

This means that the magnetoconductivity increases as the magnitude of the longitudinal magnetic field increases, This behaves quite differently from that of the conventional magnetoresistance, and is called the LNMR. Here we note that the picture above works if $\omega_B \gg \mu, T$ when the intervals of the Landau levels are sufficiently larger than other energy scales, the chemical potential μ and temperature T. In the opposite limit $\mu \gg \omega_B$, magnetoconductivity increases as the magnitude of the longitudinal magnetic field increases, but $\sigma_{zz} \propto B_z^2$ [27].

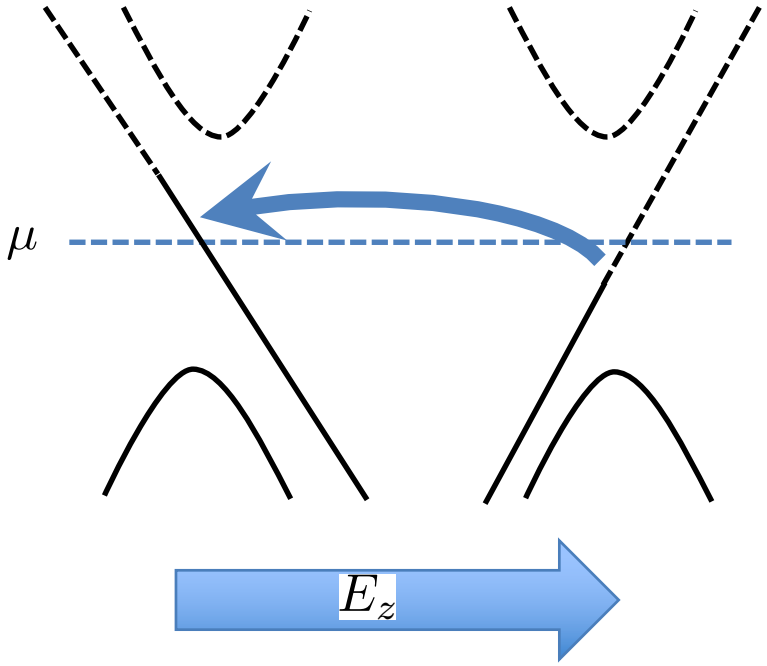

Figure 1.5: Mechanism of the LNMR. μ is the chemical potential. The solid lines and curves represent occupied bands and dashed ones valence bands.

Finally, we introduce the experimental studies of the LNMR. In Fig.1.6, we show the magnetoresistance measurements on, $Bi_{1-x}Sb_x$ [22] and TaAs [25], which are candidate

materials for the DSM and WSM, respectively. In both cases, when the direction of the magnetic fields are nearly parallel to that of the electric fields the negative magnetoresistance has been observed. Therefore these measurements provide strong evidence for the chiral-anomaly-induced transport phenomena.

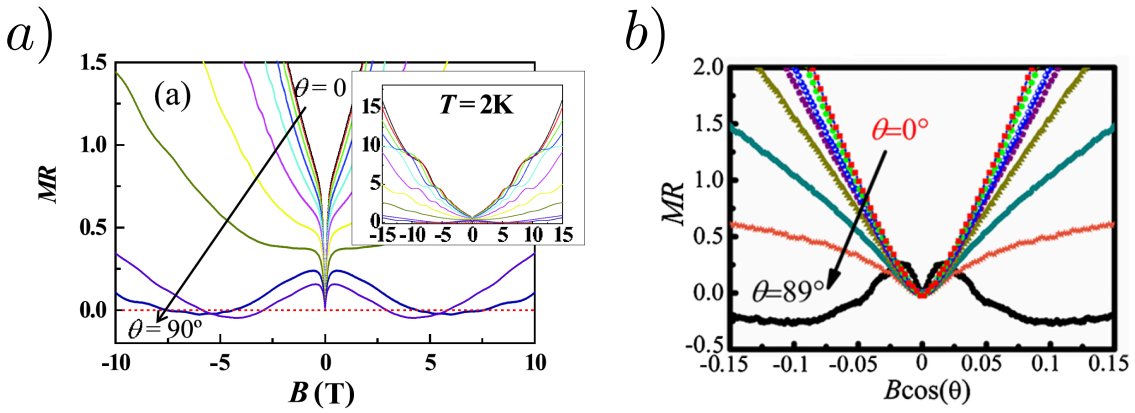

Figure 1.6: Magnetoresistances of (a) $Bi_{1-x}Sb_x$ and (b) TaAs. In both case, $\theta = 90°$ corresponds to $\boldsymbol{B} \parallel \boldsymbol{E}$. Reproduced form Refs.[22, 25].

2.2 Weyl superconductors

WSCs (or Weyl superfluids) have one or more pairs of the Weyl nodes with opposite chirality in the BdG momentum space. There are a few candidate materials for them. One is the A-phase of ^{3}He, which is a well known material for a long time [4]. Moreover, recent both experimental and theoretical studies have supported that the pairing symmetry of the heavy fermion superconductor URu_2Si_2 is the chiral $d_{xz}+id_{yz}$ wave and this compound is a WSC. Here we refer to these studies. The broken time-reversal-symmetry of the paring state was examined by the Kerr effect measurement [28]. Furthermore, the measurement of the Nernst effect also provides supporting evidence for the chiral paring state [29, 30]. In Ref.[29], it is reported that a colossal Nernst signal was observed near and above the transition temperature $T_c \sim 1.5K$ for URu_2Si_2. This signal cannot be understood by the Aslamazov-Larkin mechanism, conventional mechanism of superconducting fluctuation (Fig.1.7.a). On the other hand, the chiral fluctuation mechanism, which was introduced in our theoretical paper [30] and characteristic of chiral superconductors, can successfully explain this signal (Fig.1.7.b).

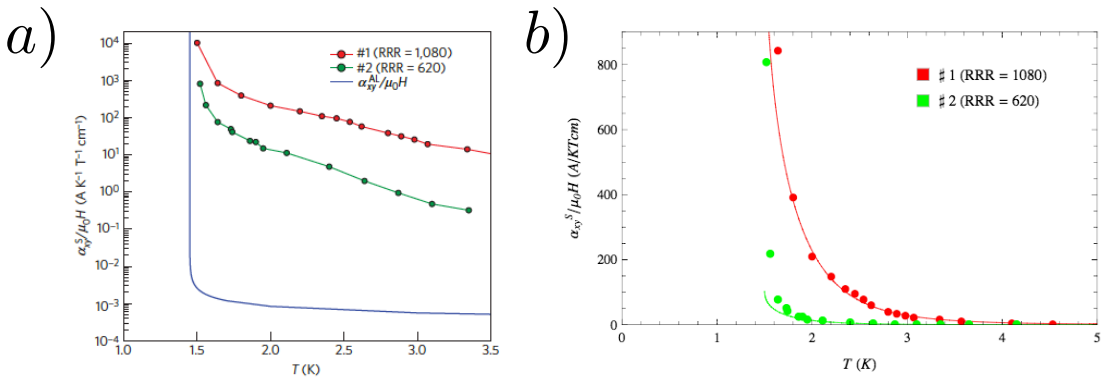

Figure 1.7: a) Transverse Peltier coefficients of URu_2Si_2 samples with different purities (red dots for a $RRR = 1080$ sample and green for $RRR = 620$ one). The solid line is the calculated result based on the Aslamazov-Larkin mechanism. b) Theoretical results of transverse Peltier coefficients due to the chiral fluctuation mechanism [30] (solid lines), which successfully explain the experimental data (circles). These figures are reproduced from Ref.[29].

Chapter 2

Geometrical response in condensed matter physics

The gravity can be understood as the consequence of curved spacetimes. Therefore the mathematical formalism of the differential geometry is widely used for descriptions of the gravity in the fields of cosmology and high-energy physics. Also in condensed matter physics, it is useful for describing various phenomena in materials. We introduce the formalism of the differential geometry in Sec.2.1, and its applications to condensed matter systems, especially, topological materials in Secs.2.2 and 2.3. Finally, in Sec.2.4 we summarize this chapter and, based on it, describe the motivations of our studies.

1 Differential geometry

In this section, we review the theory of the differential geometry, focussing on manifold with torsion and vielbein formalism.

1.1 Affine connection

In this subsection, we heuristically introduce the concept of the affine connection, which is a fundamental quantity that characterizes geometrical structures of curved space-times. Now we consider a "parallel transport" of a vector. In a flat space-time, we can

naturally define a parallel transport of a tangent vector $V(p) \in T_p(\mathbb{R}^D)$

$$V(p) := V^\mu(p)\frac{\partial}{\partial x^\mu(p)} \to \tilde{V}(p') := \tilde{V}^\mu(p')\frac{\partial}{\partial x^\mu(p')} \tag{2.1.1}$$

with

$$\tilde{V}^\mu(p') = V^\mu(p). \tag{2.1.2}$$

Here $p \in \mathbb{R}^D$ and $p' \in \mathbb{R}^D$ are different point in the flat space-time as shown in Fig.2.1.a. However, in a curved space-time, or manifold, such naive definition dose not work, since the definition using a local coordinate $\{x^\mu\}$ on the manifold is different from that using another $\{x'^\mu\}$. To solve this problem, we introduce connection coefficients $\Gamma^\mu_{\ \nu\lambda}$ and redefine the parallel transport as

$$\tilde{V}^\mu(p') = V^\mu(p) - \varepsilon\Gamma^\mu_{\ \nu\lambda}(p)W_p^\nu V^\lambda(p) \tag{2.1.3}$$

Here we suppose p' is very close to p and then we can write the difference vector in the coordinate $\{x^\mu\}$ as $x^\mu(p') - x^\mu(p) = \varepsilon W_p^\mu + \mathcal{O}(\varepsilon^2)$, where the tangent vector $W_p := W_p^\mu\partial_\mu$ indicates the direction from p to p'. Moreover, by supposing the transformation law of the connection coefficients under change of the coordinate $\{x^\mu\}$ from to $\{x'^\mu\}$ as

$$\Gamma'^\mu_{\ \nu\lambda} = \frac{\partial x^\kappa}{\partial x'^\nu}\frac{\partial x^\theta}{\partial x'^\lambda}\frac{\partial x'^\mu}{\partial x^\eta}\Gamma^\eta_{\ \kappa\theta} + \frac{\partial^2 x^\kappa}{\partial x'^\nu \partial x'^\lambda}\frac{\partial x'^\mu}{\partial x^\kappa}, \tag{2.1.4}$$

the definition of parallel transport is independent of the choice of the coordinate.

Using the parallel transport, we can compare two tangent vectors on different points $p, p' \in M$, and therefore define a derivative of a vector field $V \in \mathcal{X}(M)$ with respect to the tangent vector $W_p \in T_pM$ at $p \in M$. This derivative is called an affine connection or a covariant derivative, and defined as

$$(\nabla_{W_p}V)(p) = \lim_{\varepsilon\to 0}\frac{V(p') - \tilde{V}(p')}{\varepsilon}, \tag{2.1.5}$$

or using Eq.(2.1.4),

$$(\nabla_{W_p}V)(p) = \left(\frac{\partial V^\mu}{\partial x^\nu}W_p^\nu + \Gamma^\mu_{\ \nu\lambda}(p)W_p^\nu V^\lambda(p)\right)\frac{\partial}{\partial x^\mu}. \tag{2.1.6}$$

Moreover, moving $p \in M$, we obtain a $\mathbb{R}$-bilinear map from $\mathcal{X}(M) \times \mathcal{X}(M)$ to $\mathcal{X}(M)$, which also called an affine connection and satisfy

$$\nabla_{fW} V = f \nabla_W V, \tag{2.1.7}$$

$$\nabla_W (fV) = f \nabla_W V + W[f] V \tag{2.1.8}$$

for arbitrary vector fields $V, W \in \mathcal{X}(M)$ and smooth functions $f \in C^\infty(M)$.

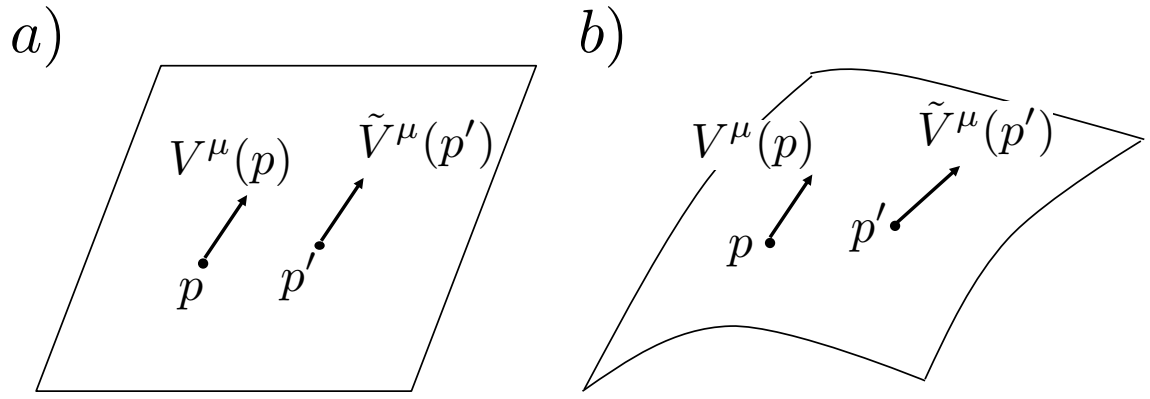

Figure 2.1: Parallel transports of vectors in a) flat and b) curved spacetime.

1.2 Curvature and torsion

We define $\mathbb{R}$-bilinear and $\mathbb{R}$-trilinear maps from $\mathcal{X}(M) \times \mathcal{X}(M)$ and $\mathcal{X}(M) \times \mathcal{X}(M) \times \mathcal{X}(M)$ to $\mathcal{X}(M)$ as

$$T(X, Y) := \nabla_X Y - \nabla_Y X - [X, Y], \tag{2.1.9}$$

$$R(X, Y, Z) := \nabla_X \nabla_Y Z - \nabla_Y \nabla_X Z - \nabla_{[X,Y]} Z, \tag{2.1.10}$$

where the Poisson braket of vectors field $V = V^\mu \partial_\mu, W = W^\mu \partial_\mu \in \mathcal{X}(M)$ is given by $[V, W] = \{V^\nu \partial_\nu (W^\mu) - W^\nu \partial_\nu (V^\mu)\} \partial_\mu$. The point is that they are not merely $\mathbb{R}$-bilinear (trilinear), but $(1, 2)$- and $(1, 3)$-tensors since

$$T(fX, Y) = T(X, fY) = f T(X, Y), \tag{2.1.11}$$

$$R(fX, Y, Z) = R(X, fY, Z) = R(X, Y, fZ) = f R(X, Y, Z), \tag{2.1.12}$$

hold for any smooth functions $f \in C^\infty(M)$. Here we define the torsion and curvature coefficients as the expansion coefficients with respect to the basis $\{\partial_\mu\}_{\mu=1,2,\cdots,D}$ and

defined by $T(\partial_\mu, \partial_\nu) = T^{\lambda}_{\ \mu\nu}\partial_\lambda$ and $R(\partial_\mu, \partial_\nu, \partial_\lambda) = R^{\kappa}_{\ \lambda\mu\nu}\partial_\kappa$. Following from Eqs.(2.1.11) and (2.1.12), they transform covariantly under change of the coordinate $\{x^\mu\} \to \{x'^\mu\}$:

$$T'^{\lambda'}_{\ \mu'\nu'} = \frac{\partial x^\mu}{\partial x'^{\mu'}}\frac{\partial x^\nu}{\partial x'^{\nu'}}\frac{\partial x'^{\lambda'}}{\partial x^\lambda}T^{\lambda}_{\ \mu\nu} \tag{2.1.13}$$

$$R'^{\kappa'}_{\ \lambda'\mu'\nu'} = \frac{\partial x^\mu}{\partial x'^{\mu'}}\frac{\partial x^\nu}{\partial x'^{\nu'}}\frac{\partial x^\lambda}{\partial x'^{\lambda'}}\frac{\partial x'^{\kappa'}}{\partial x^\kappa}R^{\kappa}_{\ \lambda\mu\nu}. \tag{2.1.14}$$

1.3 Metric

In this subsection, we introduce the concept of the metric, which also characterizes the geometrical structures of curved space-time, and explains the relationship between it and the affine connection. The metric is a $(0, 2)$-tensor, which is represented by using a coordinate $\{x^\mu\}$ as

$$g = g_{\mu\nu}dx^\mu \otimes dx^\nu. \tag{2.1.15}$$

When g is positive-definite, the set of the manifold and the metric, (M, g), is called a Riemannian manifold, and if one dimension has an opposite sign to that of the rest, it is called Lorentzian manifold. In this thesis we discuss the latter.

Now we suppose that the Lorentzian manifold (M, g) has the affine connection ∇, and show that we may put restrictions on the possible form of the affine connection. We impose that the metric is preserved by parallel transport:

$$X[g(Y, Z)] = g(\nabla_X Y, Z) + g(Y, \nabla_X Z), \tag{2.1.16}$$

for arbitrary vector fields $X, Y, Z \in \mathcal{X}(M)$. If this condition is satisfied, we say that the affine connection is compatible with the metric. Using this condition we find that the affine connection is written as

$$\Gamma^{\mu}_{\ \nu\lambda} = \mathring{\Gamma}^{\mu}_{\ \nu\lambda} + K^{\mu}_{\ \nu\lambda}, \tag{2.1.17}$$

where $\mathring{\Gamma}^{\mu}_{\ \nu\lambda}$ is the Christoffel symbol defined by

$$\mathring{\Gamma}^{\mu}_{\ \nu\lambda} = \frac{1}{2}g^{\mu\kappa}(\partial_\nu g_{\lambda\kappa} + \partial_\lambda g_{\nu\kappa} - \partial_\kappa g_{\nu\lambda}), \tag{2.1.18}$$

and $K^{\mu}_{\ \nu\lambda}$ are called the contorsion defined by

$$K^{\mu}_{\ \nu\lambda} = \frac{1}{2}(T^{\mu}_{\ \nu\lambda} + T_{\lambda}^{\ \ \mu}{}_{\nu} + T_{\nu}^{\ \ \mu}{}_{\lambda}). \tag{2.1.19}$$

Here $g^{\mu\nu}$ is the inverse matrix of $g_{\mu\nu}$ and $T^{\lambda}{}_{\mu\nu}$ is the torsion tensor defined in the previous subsection. The derivation of Eq.(2.1.17) is described in, for instance, Ref.[31].

The equation (2.1.17) is important. Indeed, we obtain directly from this equation the fundamental theorem of Riemannian geometry: on a Lorentzian manifold (M, g), there is a unique torsionless affine connection compatible with the metric, and it is given by $\Gamma^{\mu}{}_{\nu\lambda} = \mathring{\Gamma}^{\mu}{}_{\nu\lambda}$. Here we used $K^{\mu}{}_{\nu\lambda} = 0$ if the torsion is zero. On the other hand, if we do not impose the torsionless condition, more than one affine connections compatible with the metric are possible.

1.4 Vielbein and spin connection

In the previous subsections, we use the affine connection and metric to characterize curved space-time. On the other hand, in this subsection, we introduce another formalism of vielbeins and spin connections. They offer two merits in application to condensed matter systems: 1. Using them we can define Lorentz transformations at each point in the space-time. Therefore we obtain the field theory of Dirac particles on curved space-times, which is an effective theory for some condensed matter systems. 2. This formalism can describe manifolds even with non-zero torsions, which sometimes emerge in condensed matter systems as described in Sec.2.2, although the metric lack the information of the torsion following from the fundamental theorem of Riemannian geometry as mentioned in the previous subsection.

First, we give the definitions of the vielbeins $\{e^{\alpha}\}_{\alpha=\bar{0},\bar{1},\cdots,\overline{D-1}}$ and the spin connections $\{\omega^{\beta}{}_{\alpha}\}_{\alpha,\beta=\bar{0},\bar{1},\cdots,\overline{D-1}}$. They are one-forms on a D-dimensional manifold M with a metric g and an affine connection ∇, which are compatible to the metric. The vielbeins are, at each point $p \in M$, the basis of the dual space T_p^*M. And their dual vectors $\{e_{\alpha}\}_{\alpha=\bar{0},\bar{1},\cdots,\overline{D-1}} \subset \mathcal{X}(M)$(which are also called vielbeins) are at each point $p \in M$, orthonormal basis of T_pM:

$$g_p(e_{\alpha}(p), e_{\beta}(p)) = \eta_{\alpha,\beta},, \tag{2.1.20}$$

with $\eta_{\alpha\beta} = \mathrm{diag}(1, -1, -1, \cdots)$. The expansion coefficients e^{α}_{μ} and e^{μ}_{α}, which are defined via $e^{\alpha} = e^{\alpha}_{\mu} dx^{\mu}$ and $e_{\alpha} = e^{\mu}_{\alpha}\partial_{\mu}$ respectively, are also called vielbeins, and the formers are the inverse matrix of the laters $e^{\alpha}_{\mu} e^{\mu}_{\beta} = \delta^{\alpha}_{\beta}$.[1] The dual of the vielbeins, called co-vielbeins

[1] In this chapter, $\mu, \nu, \lambda, \kappa$ and $\alpha, \beta, \gamma, \delta$ represent the indices in the coordinate and local orthogonal (or Lorentz) frames, respectively.

(or vielbein one-form or, simply, vielbeins), $\{e^\alpha\}_{\alpha=\bar{0},\bar{1},\cdots,\overline{D-1}} \subset A^1(M)$ preserves

$$\langle e^\alpha(p), e_\beta(p)\rangle = \delta^\alpha_\beta \tag{2.1.21}$$

at each point $p \in M$. The spin connections $\{\omega^\beta{}_\alpha\}_{\alpha,\beta=\bar{0},\bar{1},\cdots,\overline{D-1}}$ are defined by

$$\omega^\beta{}_\alpha := \omega_\mu{}^\beta{}_\alpha dx^\mu \tag{2.1.22}$$

with

$$\nabla_{e_\alpha} e^\beta = \omega_\mu{}^\beta{}_\alpha dx^\mu. \tag{2.1.23}$$

There are useful expressions of the torsions and curvatures using the vielbeins and spin connections. The torsions and curvatures have antisymmetry relations: $T(X,Y) = -T(Y,X)$ and $R(X,Y,Z) = -R(Y,X,Z)$. Therefore we can construct two-forms as

$$T^\alpha := \frac{1}{2}\langle T(e_\beta, e_\gamma), e^\alpha\rangle e^\beta \wedge e^\gamma \tag{2.1.24}$$

$$R^\alpha{}_\beta := \frac{1}{2}\langle R(e_\gamma, e_\kappa, e_\beta), e^\alpha\rangle e^\gamma \wedge e^\kappa, \tag{2.1.25}$$

which are called the torsion two-form and the curvature two-form, respectively. They can be rewritten with the vielbeins and spin-connections as

$$T^\alpha = de^\alpha + \omega^\alpha{}_\beta \wedge e^\beta \tag{2.1.26}$$

$$R^\alpha{}_\beta = d\omega^\alpha{}_\beta + \omega^\alpha{}_\gamma \wedge \omega^\gamma{}_\beta, \tag{2.1.27}$$

where these formulas are called Cartan's structure equations.

1.5 Local Lorentz symmetry and Dirac particle on curved space-time

As mentioned in the previous subsection, the formalism of differential geometry with the vielbein and spin connection makes it possible to construct the field theory of Dirac particles in curved space-times. The action of Dirac particle field ψ in curved space-time coupled with gauge field A_μ is given by

$$S^{curved}_{Dirac} = \int Vol\left[\frac{1}{2}\bar{\psi}\gamma^\alpha \nabla_{e_\alpha}\psi - \frac{1}{2}\overline{\nabla_{e_\alpha}\psi}\gamma^\alpha\psi - m\bar{\psi}\psi\right], \tag{2.1.28}$$

where the volume form Vol is defined as

$$Vol := e^{\bar{0}} \wedge e^{\bar{1}} \wedge \cdots \wedge e^{\overline{D-1}}, \tag{2.1.29}$$

and we used the notations

$$\nabla_{e_\alpha}\psi := \langle e_\alpha, \nabla\psi \rangle, \tag{2.1.30}$$

$$\nabla\psi := i(d\psi) + \frac{1}{4}\omega_{\alpha\beta}\gamma^{\alpha\beta}\psi + eA\psi. \tag{2.1.31}$$

Here γ^α is the Dirac gamma matrix, which preserves the Clifford algebra $\{\gamma^\alpha, \gamma^\beta\} = \eta^{\alpha\beta}$, and $\bar{\psi} := \psi^\dagger\gamma^{\bar{0}}$. As the Dirac action in a flat space-time has the global Lorentz symmetry, this action has the local Lorentz symmetry. Indeed, Eq.(2.1.28) is unchanged under the local Lorentz transformation:

$$\psi'(p) = \psi(p) + \frac{1}{4}\varepsilon_{\alpha\beta}\gamma^{\alpha\beta}\psi(p) \tag{2.1.32}$$

$$e'^{\alpha}(p) = e^\alpha(p) - \varepsilon^\alpha{}_\beta(p)e^\beta(p). \tag{2.1.33}$$

$$\omega'^{\alpha}{}_{\beta}(p) = \omega^\alpha{}_\beta(p) - \varepsilon^\alpha{}_\gamma(p)\omega^\gamma{}_\beta(p) - \omega^\alpha{}_\gamma(p)\varepsilon^\gamma{}_\beta(p) - d\varepsilon^\alpha{}_\beta(p) \tag{2.1.34}$$

Here the infinitesimal generator $\varepsilon_{\alpha\beta}(p)$ is, at each position $p \in M$, an asymmetric matrix.

2 Emergent geometry in condensed matter systems

In this section, we overview realizations in condensed matter systems of the differential geometry introduced in the previous section. Secs.2.2.1-2.2.3 are devoted to the explanation of setups for realizations of the torsion. We note that in the thesis we call the T^α_{i0}-type or T^α_{0i}-type torsions as the torsional electric field (TEF) and T^α_{ij}-types the torsional magnetic field (TMF), following the terminology in Refs.[32, 33, 20]. They are analogs of the electric field $F_{0i} = E_i$ and magnetic field $F_{ij} = \varepsilon^{ijk}B_k/2$. The summary of these sections are described in Tab. 2.1.

	torsion type	physical realization	reference
torsional electric field	$T^{\bar{0}}_{j0}$	temperature gradient	Sec.2.2.2
	$T^{\bar{i}}_{i0}$	compression, shrinking/enlarging	Sec.2.2.3
	$T^{\bar{i}}_{j0}$ $(i \neq j)$	rotation, twist, shear	Sec.2.2.3
torsional magnetic field	$T^{\bar{i}}_{ij}$	edge dislocation	Sec.2.2.1
	$T^{\bar{k}}_{ij}$ $(k \neq i, j)$	screw dislocation	Sec.2.2.1

Table 2.1: Types of torsions and their realization in condensed matter systems.

2.1 Strain and dislocation in crystalline systems

In this subsection, we show that vielbeins emerge owing to inhomogeneity of displacement vectors. Furthermore, based on this argument we also show that the TMF caused by dislocations.

We consider a deformed lattice shown in Fig. 2.2. We introduce the lattice frame, which is measured by an observer on the deformed lattice, and suppose that $\vec{x}(p)$ is the coordinate of the point p in the laboratory frame, $\vec{X}(p)$ is that in the lattice frame, and $\vec{u}$ is the displacement vector. Then, the relationship, $\vec{x}(p) \approx \vec{X}(p) + \vec{u}$, holds approximately. We also suppose that, without the strain, the Hamiltonian of the system is given by

$$H(-i\partial_{x^{\bar{1}}}, -i\partial_{x^{\bar{2}}}, -i\partial_{x^{\bar{3}}}). \tag{2.2.1}$$

Now we derive the Hamiltonian with the strain. For the observer on the deformed lattice, the lattice is not deformed. Then the Hamiltonian of the system is given by

$$H(-i\partial_{X^{\bar{1}}}, -i\partial_{X^{\bar{2}}}, -i\partial_{X^{\bar{3}}}). \tag{2.2.2}$$

Furthermore using the vielbeins, we can deform Eq.(2.2.2) into

$$H(-i\partial_{X^{\bar{1}}}, -i\partial_{X^{\bar{2}}}, -i\partial_{X^{\bar{3}}}) = H(-ie^i_{\bar{1}}\partial_{x^i}, -ie^i_{\bar{2}}\partial_{x^i}, -ie^i_{\bar{3}}\partial_{x^i}), \tag{2.2.3}$$

with

$$e_a^i := \frac{\partial x^i}{\partial X^a}, \tag{2.2.4}$$

or

$$e_i^a = \frac{\partial X^a}{\partial x^i} = \delta_i^a - \frac{\partial u^a}{\partial x^i}, \tag{2.2.5}$$

where e_i^a is the inverse of e_a^i, which satisfies

$$e_i^a e_b^i = \delta_b^a. \tag{2.2.6}$$

In this way, the emergent vielbein appears in systems of deformed lattices.

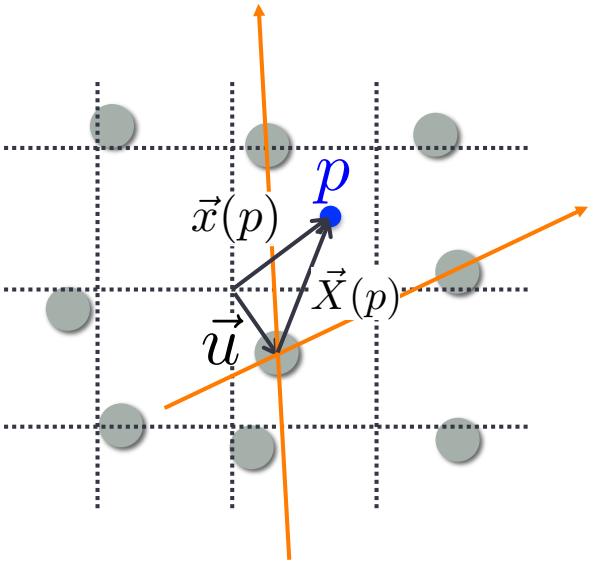

Figure 2.2: Deformed lattice and lattice frame (orange chart). $\vec{x}(p)$ is the coordinate of the point p in the laboratory frame and $\vec{X}(p)$ is that in the lattice frame, and $\vec{u}$ is the displacement vector.

Second we move on the spatial torsions or TMFs in crystalline systems. The torsion is given by $T_{ij}^a = \partial_i e_j^a - \partial_j e_i^a$, [2] and, following from Eq.(2.2.5), it can be rewritten with

[2]Compared with Eq.(2.1.26), this definition seems deficient in the term of the spin connection. In the systems of deformed lattice, they come from the inhomogeneity of the inter-band hopping. However, here we neglect them for simplicity.

the displacement vector as

$$T^a_{ij} = (\partial_j \partial_i - \partial_i \partial_j) u^a. \tag{2.2.7}$$

The point is that, if $u^a(\vec{x})$ is a well-defined function over the whole space, the torsion is always zero. Therefore, the multivaluedness of $u^a(\vec{x})$ is necessary for nonzero TMFs. Indeed, a topological defect such as dislocation causes the multivaluedness and therefore the TMF (see Fig.2.3). To see this point, we integrate the torsion over a disk D:

$$\begin{aligned} \int_D d\boldsymbol{S} \cdot \boldsymbol{T}^a_B &= -\oint_C du^a \\ &= -b^a_g. \end{aligned} \tag{2.2.8}$$

Here we introduced the three-dimensional vector, $(T^a_B)^i = \varepsilon^{ijk} T^a_{jk}/2$, and the Burgers vector of the dislocation, $\boldsymbol{b}_g$, and $\oint_C$ represent the counter integral along the circuit $C = \partial D$.

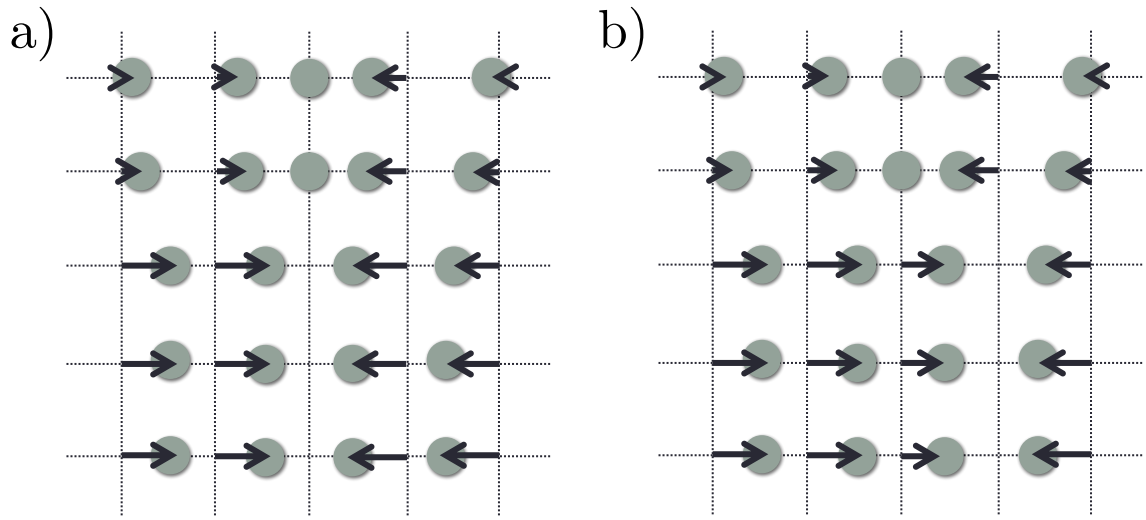

Figure 2.3: Displacement vectors of a lattice with an edge dislocation. a) and b) represent the same lattice but the displacement vectors (arrows) can be defined in different ways. Then the displacement vector field is multivalued.

The different types of dislocations cause different types of torsions. Indeed, considering a crystal with an edge dislocation (Fig.2.4.a), we find that the integral of torsion over the xy-plane is given by

$$\int dxdy T^{\bar{y}}_{xy} = -b_g \tag{2.2.9}$$

where $b_g = |\vec{b}_g|$ is the norm of the Burgers vector. Then in the continuum limit, the torsion is given by

$$\boldsymbol{T}_B^{\bar{y}} = -\boldsymbol{b}_g \delta(x, y). \tag{2.2.10}$$

Similarly, the torsion of the crystal with the screw dislocation (Fig.2.4.b) is given by

$$\int dxdy T_{xy}^{\bar{z}} = -b_g, \tag{2.2.11}$$

and, in the continuum limit,

$$\boldsymbol{T}_B^{\bar{z}} = -\boldsymbol{b}_g \delta(x, y). \tag{2.2.12}$$

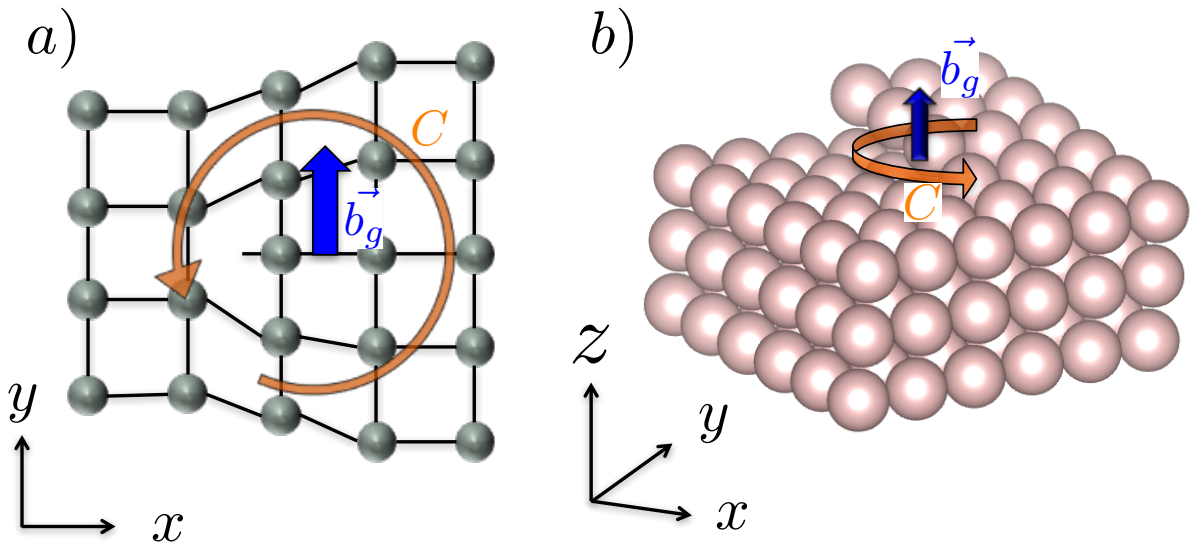

Figure 2.4: Displacement vectors of lattices with a) edge and b) screw dislocations. The orange arrows represent the path of the counter integrals C (see Eq.(2.2.8)), and the blue arrows represent the directions of the Burgers vectors $\vec{b}_g$.

2.2 Temperature gradient and thermal response

In the subsection, we show that the inhomogeneity of temperature can be described by the theory of the differential geometry and causes effective TEF. The theory of geometrical technique for thermal responses was found by Luttinger [34]. He introduced a fictitious gravitational field, which corresponds to the local temperature. Recently, this

technique has been developed using the vielbein formalism [32, 35]. Here we introduce the technique along these papers.

We suppose the original Hamiltonian is given by

$$H_0 = \int d^3x \psi^\dagger(\boldsymbol{x}) \hat{h} \psi(\boldsymbol{x}), \tag{2.2.13}$$

where $\psi^\dagger$ and ψ are the creation and annihilation operators of electrons, respectively, and $\hat{h}$ is the Hamiltonian operator. To discuss transport phenomena caused by inhomogeneity of temperature, we couple a fictitious gravitational field $\phi(\boldsymbol{x})$ with the system as

$$H_\phi = \int d^3x \left(1 + \phi(\boldsymbol{x})\right) \psi^\dagger(\boldsymbol{x}) \hat{h} \psi(\boldsymbol{x}), \tag{2.2.14}$$

Here the correspondence between the gravitational field and local temperature $T(\boldsymbol{x})$ is given by

$$\phi(\boldsymbol{x}) \sim \frac{T_0}{T(\boldsymbol{x})} - 1, \tag{2.2.15}$$

where T_0 is the average temperature of the system. Therefore the partition function is given by

$$Z = \mathrm{Tr}\left[e^{-H_\phi/T_0}\right]. \tag{2.2.16}$$

In the path integral representation, it can be transformed as

$$Z = \int \mathcal{D}\psi^\dagger \mathcal{D}\psi e^{-S_\phi[\psi^\dagger, \psi]}, \tag{2.2.17}$$

where the action $S_\phi[\psi^\dagger, \psi]$ is given by

$$S_\phi[\psi^\dagger, \psi] = \int_0^{1/T_0} d\tau d^3x \left[\psi^\dagger(\tau, \boldsymbol{x}) \partial_\tau \psi(\tau, \boldsymbol{x}) - \left(1 + \phi(\boldsymbol{x})\right) \psi^\dagger(\tau, \boldsymbol{x}) \hat{h} \psi(\tau, \boldsymbol{x})\right]. \tag{2.2.18}$$

Here this action corresponds to that of original Hamiltonian (2.2.13) coupled with the vielbeins given by

$$e_0^{\bar{0}} = 1 + \phi(\boldsymbol{x}), \tag{2.2.19}$$

$$e_\mu^\alpha = \delta_\mu^\alpha \quad \text{for others.} \tag{2.2.20}$$

In this way, we find that the local temperature corresponds to the vielbein as

$$\frac{T_0}{T(\boldsymbol{x})} \sim \left(1 + \phi(\boldsymbol{x})\right) \sim e_0^{\bar{0}}, \tag{2.2.21}$$

and, moreover, that the temperature gradient generates the TEF as

$$-\partial_i \log T(\boldsymbol{x}) \sim T_{i0}^{\bar{0}}. \tag{2.2.22}$$

2.3 Torsional electric field in fluid and lattice systems

In this subsection, we show that certain types of fluid dynamics and mechanical deformations of lattice can be described with other types of torsions.

The point is that fluid dynamics with an inhomogeneous velocity profile causes a dislocation in the space-time. We will show this heuristically. We consider two one-dimensional fluids with different velocity profiles shown in Fig. 2.5. Here one has a homogeneous velocity profile (Fig.2.5.a), and in the other the particles in the left-half side move left and those in the right-half side move right (Fig.2.5.b). Now we consider the paths of two particles, A and B, in the space-time in the both fluids. Their initial points are the same, I. First, A moves along the velocity field, and, second, is teleported right. On the other hand, B is teleported right before moves along the velocity field. In the homogeneous case (Fig.2.5.a), the end points of the two paths are the same, F. However, in the inhomogeneous case, even if the moving times and teleportation distances are equal in the two paths, the end points, F_A and F_B, are different (Fig.2.5.b). Therefore, there is, as it were, a "space-time edge dislocation", which causes the $T^{\bar{x}}_{0x}$.-type torsion.

We can also obtain a "space-time screw dislocation", which causes the $T^{\bar{y}}_{0x}$.-type torsion. Here we consider two-dimensional fluid, in which the particles in the left-half plane moves up, and those in the right-half plane moves down (Fig.2.6.a). In this case the stack of the snapshots of the fluid (Fig.2.6.b) is screw dislocation in the space-time.

Generally, the relationship between the velocity field, $\boldsymbol{v}$, and the torsional electric fields are given by

$$T^a_{0i} = -\partial_i v^a, \tag{2.2.23}$$

as discussed in Ref.[36]. Therefore, the inhomogeneous velocity field generates the torsional electric field.

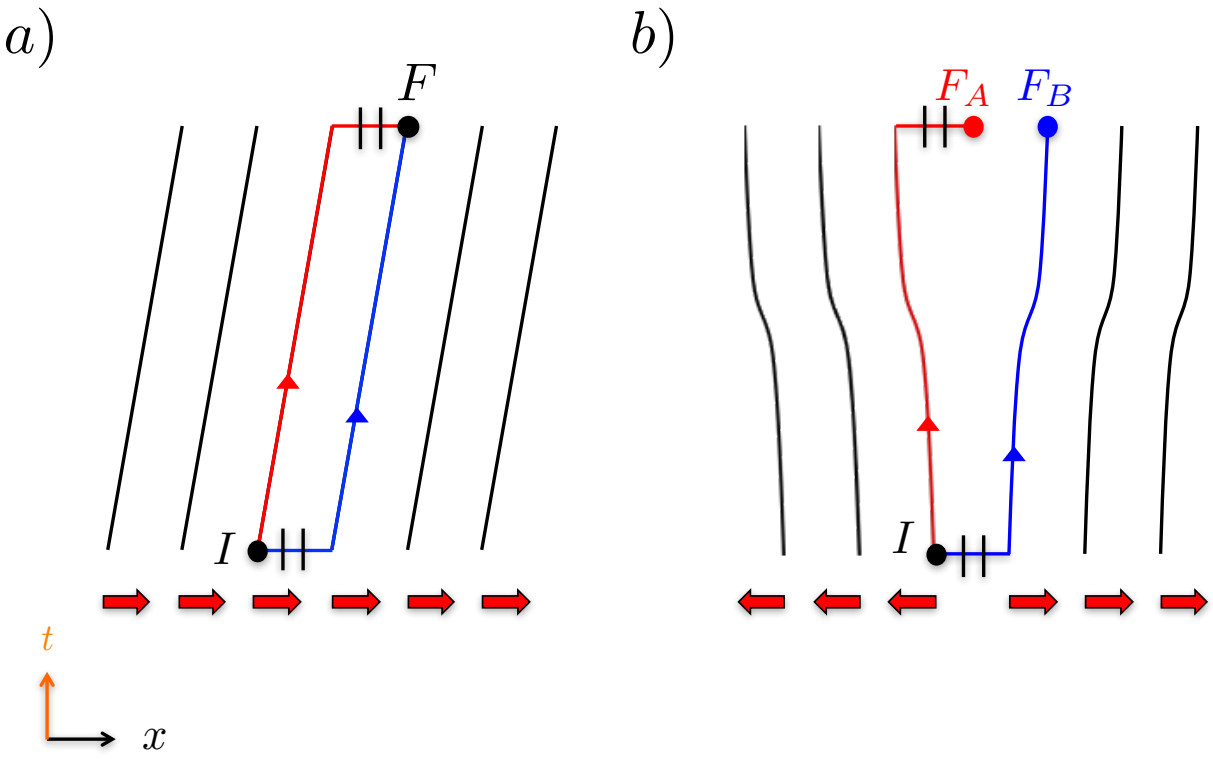

Figure 2.5: Dynamics of one-dimensional fluids with a) homogeneous and b) inhomogeneous velocity profiles. The paths of the particles, A(red) and B(blue), are shown in these figures. The horizontal axis is the spatial axis, and the vertical one is the temporal one. The red arrows represent the velocity field. The solid lines are the world-line of particles. In Fig.b, there is a "space-time edge dislocation", which causes a nonzero torsion, $T^{\bar{x}}_{0x}$.

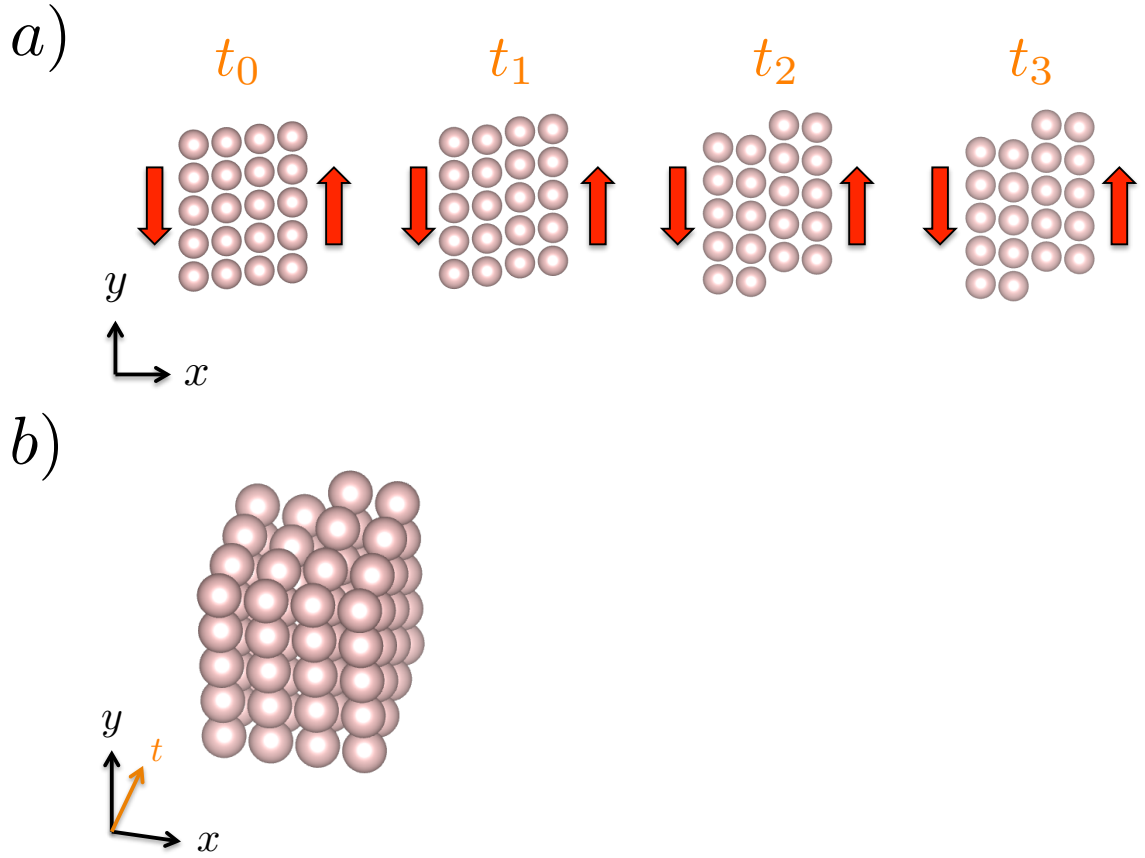

Figure 2.6: Dynamics of a two-dimensional fluid with an inhomogeneous velocity profile. a) Snapshots at $t = t_0, t_1, t_2, t_3$, with $t_0 < t_1 < t_2 < t_3$. b) Their stack. The red arrow represent the velocity field. There is the "space-time screw dislocation", which causes non-zero torsions, $T^{\bar{x}}_{0y}$ and $T^{\bar{y}}_{0x}$.

Now we move on how we can realize the space-time edge and screw dislocation. The setups for the $T^{\bar{i}}_{0i}$-type torsions are shown in Fig.2.7, and those for the $T^{\bar{i}}_{0j}$-type ($i \neq j$) ones in Fig.2.8.

In Fig.2.7.a, the solid domain wall pushes the fluid and the density wave travels up. Then, the velocity v_y is inhomogeneous along the y-direction, therefore $T^{\bar{y}}_{0y} = -\partial_y v^{\bar{y}} \neq 0$. There also a setup approachable for lattice systems as well as fluid systems, which is proposed in Ref.[37] (Fig.2.7.b).

In Fig,2.8.a the solid domain wall shaves the fluid, in Fig,2.8.b the whole system is rotated, where this setup is discussed in Ref.[38], and in fig.2.8.c the cylindrical sample

is shrunk or enlarged, where this setup is proposed in Ref.[39].

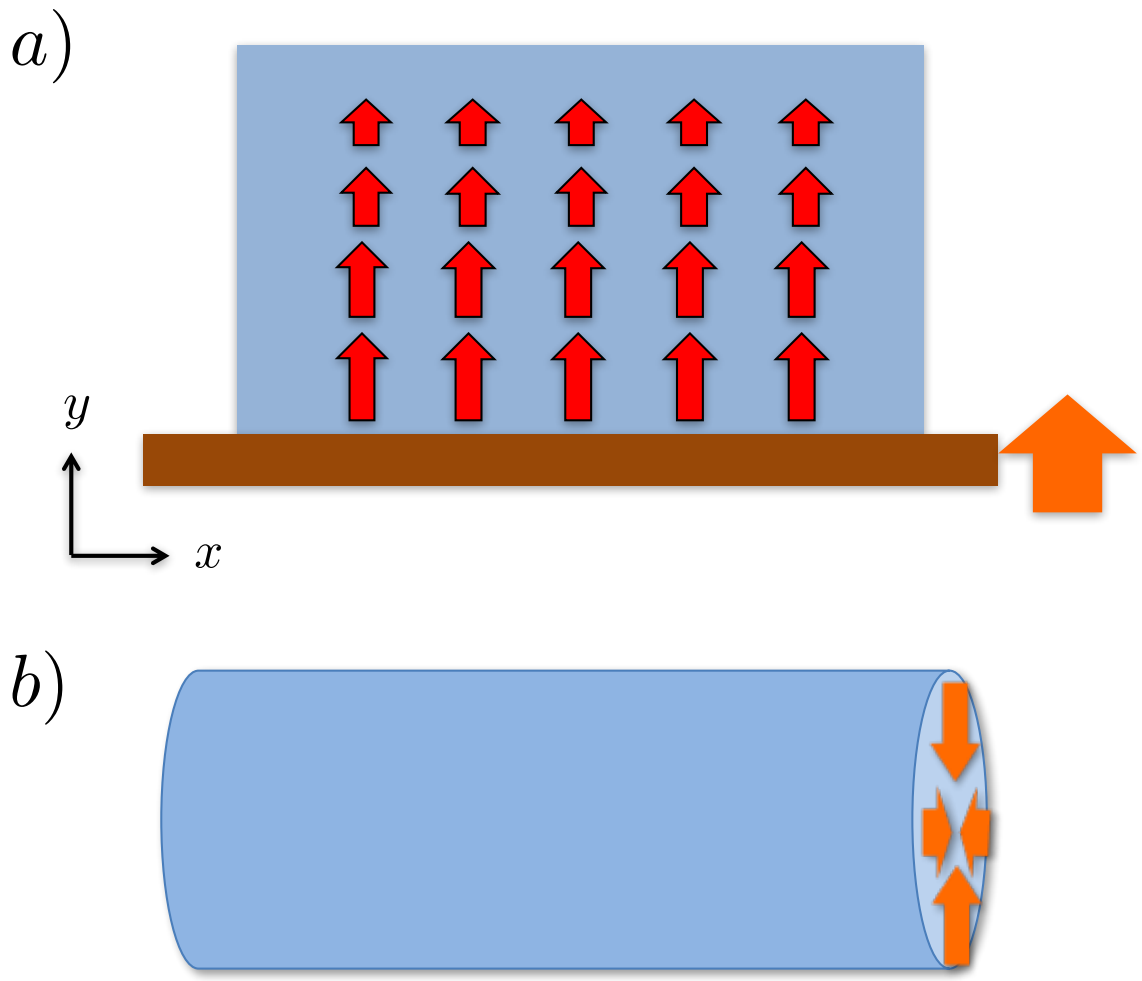

Figure 2.7: Setups for realization of the space-time edge dislocation in a) fluid and b) fluid or lattice systems. Red arrows represent the velocity of the fluid in Fig.a. In Fig.a, the solid domain wall (brown bar) push the fluid and causes density wave, and in fig.b the cylinder is shrunk or enlarged.

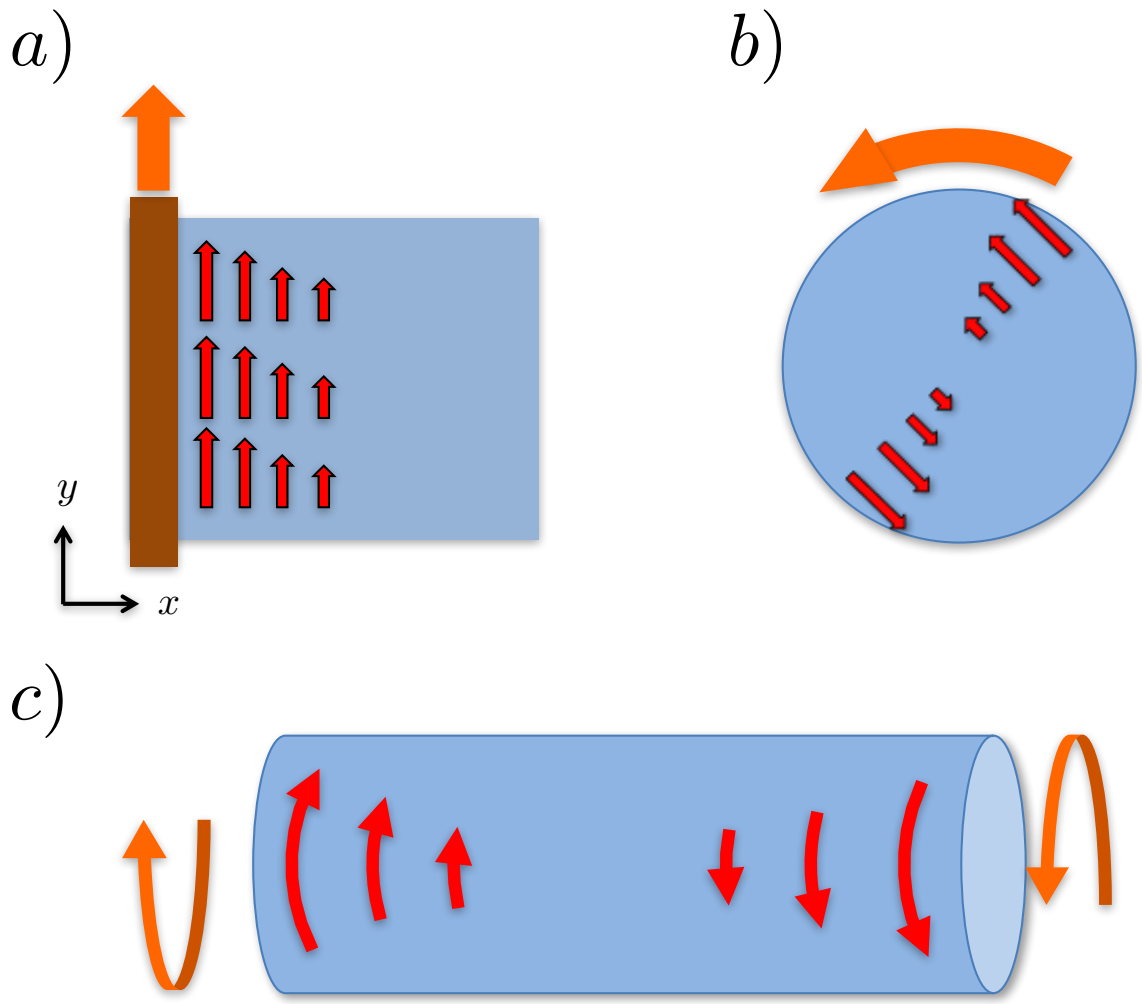

Figure 2.8: Setups for realization the space-time screw dislocation in a) fluid and b,c) fluid or lattice systems. Red arrows represent the velocity of the fluid in Fig.a and the fluid or atoms in Figs.b,c. In Fig.a, the solid domain wall (brown bar) on the fluid move horizontally, in Fig.b the sample is rotated, and the cylinder is twisted.

3 Geometrical response in topological systems

In the section, we review the works on geometrical response in topological systems, such as TIs, TSCs, and WSMs. Here we show that various dissipationless responses are described by topological actions with geometry.

3.1 Thermal transport in topological superconductors and gravitational chiral anomaly

In this subsection, we review the theories on the quantum thermal Hall effect (QTHE). This thermal response is characteristic of two-dimensional topological superconductors (TSC) with broken time-reversal symmetry (Sec.1.1).

The thermal Hall effect (THE) is the thermal analog of the Hall effect and the production of a heat current caused by a temperature gradient perpendicular to the current:

$$J_x^Q = \kappa_{xy}(-\partial_y T), \tag{2.3.1}$$

where the coefficient κ_{xy} is called the thermal Hall coefficient. Especially, the QTHE is the phenomena where the thermal Hall coefficient (divided by the temperature) is quantized as universal constant

$$\kappa_{xy} = c\frac{\pi T}{6}, \tag{2.3.2}$$

similar to the case of the Chern insulator (CI) or integer or fractional quantum Hall effect (IQHE or FQHE)

$$\sigma_{xy} = \nu\frac{e^2}{2\pi}. \tag{2.3.3}$$

Here c is the central charge of the edge theory and equal to $1/2$ for class C TSCs with the Chern number $C_1 = 1$, where we will refer to these points below, and σ_{xy} and ν represent the Hall coefficient and the filling factor, respectively. The QTHE was theoretically predicted in TSCs with broken TRS and was found to be associated with the gravitational Chern-Simons (GCS) theory and the chiral edge state [40]. Thus, it is similar to the CI, whose electric responses are described by the effective theory, Chern-Simons theory, and also understood by the chiral edge. However, this analog does not completely work as argued later (see also Fig.2.13).

3.1.1 QHE from Kubo formula, chiral anomaly, and edge theory

Before addressing the details of this point, we review the electric response and gauge theory of the QHE in two-dimensional CIs, and see that the QHE can be derived from various methods including the Kubo formula, Chern-Simons theory related to the

quantum anomaly, and pumping from a chiral edge mode to the opposite side one. Moreover we describe the relationship of these theories.

Kubo formula — First, we see that the QHE is directly derived from the bulk calculations of the Kubo formula. From the Kubo formula, the Hall coefficient is represented using the Berry curvature [41]:

$$\sigma_{xy} = -e^2 \sum_n \int_{BZ} \frac{d\boldsymbol{k}}{(2\pi)^2} f(E_n(\boldsymbol{k})) b_n(\boldsymbol{k}), \tag{2.3.4}$$

where n and $\boldsymbol{k}$ are the band index and the wave number, respectively, $E_n(\boldsymbol{k})$ is the energy value of the particle in the n-th band whose wave number is $\boldsymbol{k}$, $f(E)$ is the Fermi distribution function at temperature T, $\int_{BZ}$ represent the integral over the Brillouin zone. Here the Berry curvature is given by

$$b_n(\boldsymbol{k}) = \left(\frac{\partial}{\partial k_x} \langle u_{\boldsymbol{k}n} | \right) \left(\frac{\partial}{\partial k_y} | u_{\boldsymbol{k}n} \rangle \right) - (x \leftrightarrow y), \tag{2.3.5}$$

where $\langle u_{\boldsymbol{k}n}|$ and $|u_{\boldsymbol{k}n}\rangle$ are the bra and ket vectors of the Bloch state, respectively. Moreover, in the case of the CI in the low temperature limit, this formula is rewritten as

$$\sigma_{xy} = \frac{e^2}{2\pi} C_1(E_F) \tag{2.3.6}$$

where $C_1(E_F)$ is the first Chern number (or TKNN number)[2] defined as

$$C_1(E_F) = - \sum_{n:\text{occupiedband}} \int \frac{dk_x dk_y}{2\pi} b_n(\boldsymbol{k}) \in \mathbb{Z}, \tag{2.3.7}$$

and always an integer.

Chiral anomaly and Chern-Simons theory — Second, we see that this quantized Hall effect is understood as a consequence of the Chern-Simons (CS) theory, which is a topological field theory, of which action is given by

$$S_{CS} = \frac{C_1}{4\pi} \int d^2x dt \varepsilon^{\mu\nu\lambda} A_\mu \partial_\nu A_\lambda. \tag{2.3.8}$$

Indeed, its contribution to the current is

$$j^x = \frac{\delta S_{CS}}{\delta A^x} = \frac{C_1}{2\pi} E_y. \tag{2.3.9}$$

Here we set $e = 1$. The CS action is related to the chiral $U(1)$ anomaly of the higher dimensional Dirac model. To see it, we consider a $3 + 1$ dimensional massive Dirac model coupled with the $U(1)$ gauge field:

$$e^{iS_{eff}[m,A_\mu]} = \int \mathcal{D}[\bar{\psi},\psi] e^{iS[\bar{\psi},\psi,A_\mu,m]} \tag{2.3.10}$$

$$S[\bar{\psi},\psi,A_\mu,m] = \int dx^3 dt \bar{\psi}[\gamma^\mu(i\partial_\mu - A_\mu) - m]\psi, \tag{2.3.11}$$

where γ^μ is the 4×4 gamma matrices. We assume that the Dirac mass m depends on the coordinate z gradually and $m(z) > 0$ for $z > 0$, which and $m(z) < 0$ for $z < 0$ as shown in Fig.2.9, and we assume that this model is in a topologically nontrivial phase for $m > 0$ and in a topologically trivial phase for $m < 0$. The trivial and nontrivial phases are characterized by the θ term. To see this, we perform the chiral rotation on this Dirac model:

$$\psi = e^{i\phi\gamma_5/2}\psi', \quad \psi^\dagger = \psi'^\dagger e^{-i\phi\gamma_5/2}. \tag{2.3.12}$$

Under this rotation, the action becomes

$$S[\bar{\psi},\psi,A_\mu,m] = \int dx^3 dt \bar{\psi}'[\gamma^\mu(i\partial_\mu - A_\mu) - m(\cos\phi + i\gamma_5 \sin\phi)]\psi', \tag{2.3.13}$$

and, then, at $\phi = \pi$,

$$S[\bar{\psi},\psi,A_\mu,m] = S[\bar{\psi}',\psi',A_\mu,-m]. \tag{2.3.14}$$

However, we cannot conclude that the effective action with m is the same as that with $-m$:

$$S_{eff}[m,A_\mu] \neq S_{eff}[-m,A_\mu]. \tag{2.3.15}$$

It is because that this transformation costs the Jacobian $\mathcal{J}$ of the path integral measure,

$$\mathcal{D}[\bar{\psi},\psi] = \mathcal{J}\mathcal{D}[\bar{\psi}',\psi']. \tag{2.3.16}$$

This phenomena is called the chiral anomaly. Calculating $\mathcal{J}$ by using the Fujikawa method [11], we obtain the θ-term as the difference between the effective action of the trivial and nontrivial phase:

$$e^{iS_{eff}[A_\mu,m]-S_{eff}[A_\mu,-m]} = e^{iS_\theta[A_\mu]}, \tag{2.3.17}$$

$$S_\theta[A_\mu] := \int dx^3 dt \frac{\theta}{32\pi^2} \varepsilon^{\mu\nu\rho\lambda} F_{\mu\nu} F_{\rho\lambda} \tag{2.3.18}$$

with $\theta \equiv \pi \pmod{2\pi}$. Here there is the ambiguity of 2π in the value of θ since not only the π chiral rotation of ϕ but also the $\pi + 2n\pi$ ($\forall n \in \mathbb{Z}$) rotation transforms m to $-m$. When the system preserves time-reversal-symmetry, the transformation $\theta \to -\theta$ does not change the action, and therefore θ is always equal to 0 or $\pi \pmod{2\pi}$, which is the $\mathbb{Z}_2$-topological number that characterizes the three-dimensional class AII TI. From the surface viewpoint, this number characterizes the number of massless Dirac modes, and 0 (or π) corresponds to even (or odd) number of the modes, where two Dirac modes can pair-annihilate (and pair-create) by a perturbation. Now we weekly break the time-reversal-symmetry by, for example, doping magnetic impurities. The value of θ is no longer quantized as 0 or π, and we assume that $\theta(z)$ is a continuous function of z, the axis perpendicular to the surface (bottom of Fig.2.9). Applying integral by parts to Eq.(2.3.18) and taking the limit as $\theta(z) \to \pi H(-z)$, where H is the Heaviside step function, we obtain the effective action of the surface:

$$S_{surface}[A_\mu] = \frac{1}{2}\frac{1}{4\pi}\int dxdydt\varepsilon^{\mu\nu\lambda}A_\mu\partial_\mu A_\lambda. \tag{2.3.19}$$

Compared with Eq.(2.3.8), one may consider that this is a contradiction because the Chern number is one-half of the quantization value, $C_1 = 1/2$. However, this term is contribution of one massive Dirac modes which can be realized on a surface of three-dimensional TI but cannot in two-dimensional bulk systems. In such systems, odd number of Dirac modes cannot exist but even number of them can exist, and therefore the coefficient of the action is quantized and the effective action of two-dimensional class A TI (or CI) is given by

$$S_{CS}[A_\mu] = \frac{N}{4\pi}\int dxdydt\varepsilon^{\mu\nu\lambda}A_\mu\partial_\nu A_\lambda, \tag{2.3.20}$$

$$\text{with} \quad N = C_1 \in \mathbb{Z}. \tag{2.3.21}$$

Here we comment that a two-dimensional tight-binding model, which has a pair of Dirac modes as the low-energy effective dispersion and has a nonzero Chern number $C_1 = \pm 1$, was proposed by Haldane in Ref.[42].

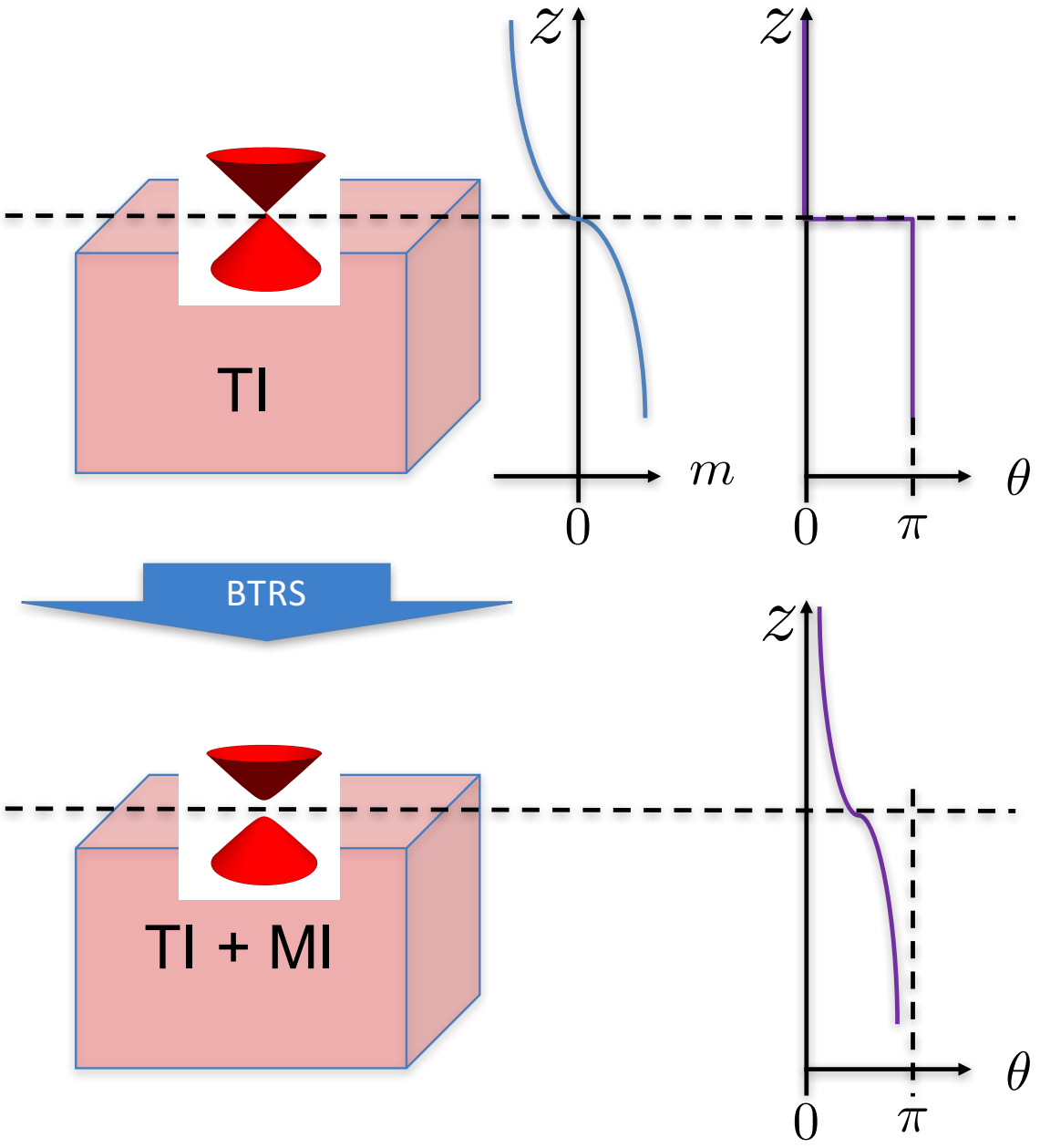

Figure 2.9: Three-dimensional TI, of which surface a two-dimensional massless Dirac fermions (upper figure), and, breaking the time-reversal-symmetry by doping magnetic impurities, they acquire mass and the surface spectrum becomes gapped and therefore the surface corresponds to "one-half of" the CI (lower figure).

Edge theory and Callan-Havey anomaly inflow — As yet we have derived the CS action Eq.(2.3.20) as the effective action of two-dimensional TIs from the chiral anomaly

in three-dimensional TIs, and we have seen that the QHE directly follows from the CS action, which is the effective action of the bulk CI. Now we derive the effect from the edge picture: we show that the existence of chiral modes is necessary for the cancelation of the gauge anomaly of the bulk CS action, and derive the QHE from the chiral edge modes. We consider a two-dimensional CI with a boundary, of which effective action is the CS action (2.3.20) with boundary:

$$S_{CS}[A] = \frac{C_1}{4\pi} \int_{\mathbb{R}\times M} A \wedge F, \tag{2.3.22}$$

where $M \subset \mathbb{R}^2$ corresponds to the domain of the sample. Now we perform the gauge transformation:

$$A \to A + d\chi, \tag{2.3.23}$$

where $\chi(x)$ is any smooth scalar function of the position x. Then the difference is given by

$$\begin{aligned} \delta S_{CS}[A;\chi] :=& S_{CS}[A + d\chi] - S_{CS}[A] \\ =& \frac{C_1}{4\pi} \int_{\mathbb{R}\times M} d\chi \wedge F, \\ =& \frac{C_1}{4\pi} \int_{\mathbb{R}\times \partial M} \chi F, \end{aligned} \tag{2.3.24}$$

where ∂M is the boundary of M, and we used the Stokes' formula. Then the CS action is not gauge invariant and the extra surface term appears. However, the number of the electrons in the whole system is preserved, and then the gauge symmetry must be preserved. This contradiction is resolved by existence of chiral edge mode, which is not gauge invariant owing to the ($(1+1)$-dimensional) chiral anomaly. Here the extra term due to the CS term is cancelled out by that due to the chiral edge mode. This mechanism is called the Callan-Havey anomaly inflow mechanism [43]. Indeed, using the similar technique to that for the derivation of Eq.(2.3.18), we find that the extra term due to the gauge transformation in the theory of C_1 left-moving chiral edge modes is given by

$$\begin{aligned} \delta S^L_{edge}[A_\mu;\chi] =& S^L_{edge}[A_\mu + \partial_\mu \chi] - S^L_{edge}[A_\mu] \\ =& -\frac{C_1}{4\pi} \int dt dx \chi F_{01} \end{aligned} \tag{2.3.25}$$

which compensates the extra term (2.3.24) (see Chapter 8 of [11] for the details of the derivation). Here we assumed that the shape of the edge is a straight line along x-axis, $\partial M = \mathbb{R}$.

Now we give the physical picture of Eq.(2.3.25) and derive the QHE. First we consider how the Noether's theorem is corrected by this extra term. The current is defined by the variation of the action with respect to the gauge field as

$$S^L_{edge}[A_\mu + \delta A_\mu] - S^L_{edge}[A_\mu] = \int dtdx \delta A_\mu j^\mu_L, \tag{2.3.26}$$

where $\delta A_\mu(x)$ is an arbitrary function. Then, by substitution of δA_μ in this equation to $\partial_\mu \chi$ and using Eq.(2.3.25), we obtain

$$-\frac{C_1}{4\pi}\int dtdx \chi F_{01} = \int dtdx \partial_\mu \chi j^\mu_L. \tag{2.3.27}$$

Moreover, integrating by parts and reminding that χ is an arbitrary function, we can derive the non-conservation of the current as

$$\partial_\mu j^\mu_L = \frac{C_1}{4\pi} E_x, \tag{2.3.28}$$

where $E_x = F_{01}$ is the electric field. By integrating over the space, $\int dx/L_x$, we obtain

$$\frac{dn_L}{dt} = \frac{C_1}{4\pi} E_x, \tag{2.3.29}$$

where n_L is the electron density and L_x is the sample size along the x-direction. This equation means that in the presence of electric field, the number of electrons in this edge mode increases. These electrons are pumped from the opposite edge mode, in which

$$\frac{dn_R}{dt} = -\frac{C_1}{4\pi} E_x. \tag{2.3.30}$$

These equations show that the difference in the chemical potentials of the two edges occures owing to the electric field and the electrons are pumped from an edge to the opposite edge as shown in Fig.2.10. Then, the net current along the y-direction occurs as

$$j_y = \frac{d(n_R - n_L)}{dt} = -\frac{C_1}{2\pi} E_x. \tag{2.3.31}$$

Then we have derived the QHE from the edge picture.

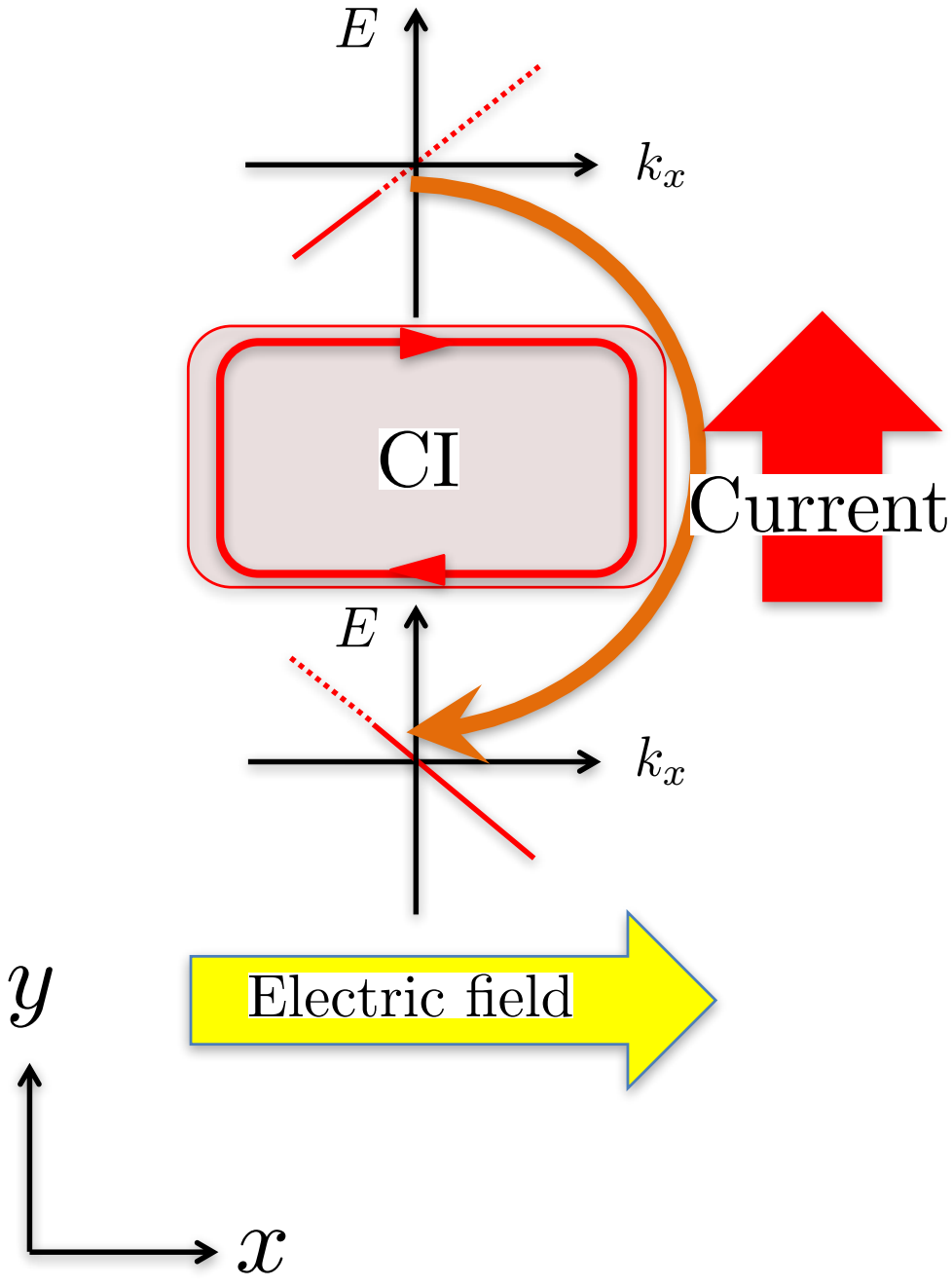

Figure 2.10: In the presence of electric field the electrons are pumped form an edge to the opposite edge, and the Hall current is generated.

3.1.2 Bulk and edge theories of QTHE

In the previous subsection we have discussed the bulk and edge theories of the QHE in CIs and described their relationship. In this subsection we discuss those of the QTHE in two-dimensional TSCs with broken time-reversal-symmetry. Here we note that electromagnetic responses cannot grasp the topological features of TSCs since the charge is not conserved in superconductors although thermal responses can since the energy is conserved. As mentioned above, although the QTHE is the transport phenomenon that is the thermal analog of the QHE, its theoretical formulations have more complicated and subtle points, which we will explain in this subsection.

First, we comment on the linear response theory. The calculation of the thermal Hall conductivity is technically involved, because not only the heat-current-heat-current four-point correlation function but also the "heat magnetization" contributes this coefficient as Smrcka and Streda mentioned in Ref.[44]. The heat magnetization is the thermal analog of the orbital magnetization, and we need an elaborate technique for its calculation. We will argue this point in Chapter 3.

Next, we move on the bulk topological action. By a similar method to that for the derivation of the CS action, we can derive the bulk effective action as follows. We start with the $(3+1)$-dimensional massive Dirac model in a curved spacetime (see Eq.(2.1.28))

$$S[\bar{\psi},\psi,e^{\alpha},m]=\int Vol\left[\frac{1}{2}\bar{\psi}\gamma^{\alpha}\nabla_{e_{\alpha}}\psi-\frac{1}{2}\overline{\nabla_{e_{\alpha}}\psi}\gamma^{\alpha}\psi-m\bar{\psi}\psi\right], \tag{2.3.32}$$

where ψ is a fermion field with a reality condition, i.e. Majorana fermions field, since we consider a superconducting system. Here we impose the condition of the torsion-free $T^{\alpha}=0$. From the action and using the same technique as that for the derivation of Eq.(2.3.19): i.e. deriving the θ-term by producing the chiral rotation (where the calculation of the Jacobian of the path integral measure is described, for instance, in Ref.[11]) and breaking the time-reversal-symmetry (see Fig.2.11), we find that the effective action of the surface is given by

$$S^{TSC}_{surface}[\Gamma]=\frac{1}{2}\frac{c}{96\pi}\int_{\mathbb{R}\times M}\mathrm{tr}\left[\Gamma\wedge d\Gamma+\frac{2}{3}\Gamma\wedge\Gamma\wedge\Gamma\right]. \tag{2.3.33}$$

Here $\mathbb{R}$ corresponds to the time axis, $M\subset\mathbb{R}^2$ is the domain of the sample, the constant c is in this case equal to $1/2$, which corresponds to the central charge of the edge

theory, which will be mentioned below, and Γ represent a matrix valued one-form whose elements are given by

$$(\Gamma)^{\mu}_{\ \nu} = \Gamma^{\mu}_{\ \nu\lambda} dx^{\lambda}, \tag{2.3.34}$$

where $\Gamma^{\mu}_{\ \nu\lambda\tau}$ is the Christoffel symbol defined in Sec.2.1. Here we impose the condition of the torsion-free. Like the case of the TI, it is the one-half of the two-dimensional class D TSC. Then, the effective action of the two-dimensional TSC is two times Eq.(2.3.33) :

$$S_{GCS}[\Gamma] = \frac{c}{96\pi} \int_{\mathbb{R}\times M} \mathrm{tr}\left[\Gamma \wedge d\Gamma + \frac{2}{3}\Gamma \wedge \Gamma \wedge \Gamma\right], \tag{2.3.35}$$

which is called the gravitational Chern-Simons (GCS) action.

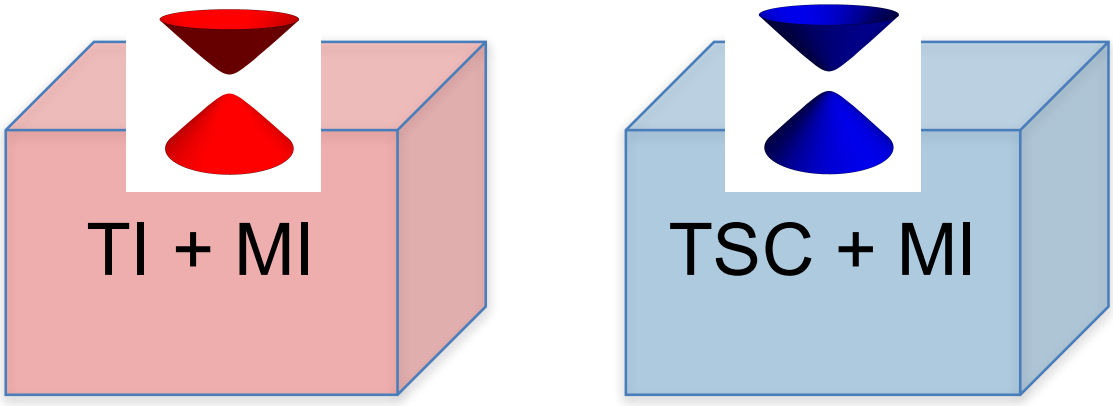

Figure 2.11: (left) Three-dimensional class AII TI with weekly broken time-reversal-symmetry by doping magnetic impurities, whose surface is "one-half" of the two-dimensional CI (or class A TI). (right) Three-dimensional class CI TSC with magnetic impurities, whose surface is "one-half" of the two-dimensional class D TSC.

As discussed in Sec.2.2.2, the effects of a thermal gradient is equivalent to an inhomogeneous background gravitational field. Then, one may consider that the QTHE can be derived directly form this action by variation method like the case of the QHE. However, this attempting does not work because this action is of too high order in derivatives of the metric [35].

Besides, we derive the effect from an edge picture. We consider the Lie derivative of the GCS action (2.3.35) with respect to the vector filed $X = X^{\mu}\partial_{\mu}$, like a gauge

transformation of the CS action above. By straightforward but hard calculation, we find that this Lie derivative is not qual to 0 but has a surface term given by

$$\begin{aligned}\delta_X S_{GCS}[\Gamma] =& \frac{c}{96\pi}\int_{\mathbb{R}\times M} d\left[(\partial_\mu X^\nu)(d\Gamma)^\mu{}_\nu\right] \\ =& -\frac{c}{96\pi}\int_{\mathbb{R}\times\partial M} X^\nu \partial_\mu (d\Gamma)^\mu{}_\nu,\end{aligned} \tag{2.3.36}$$

(see [43] for the calculation). This implies that the bulk energy-momentum tensor, which is the Noether current of the Lie derivative, is not conserved alone and we need counter term that comes from the edge theory such that

$$\delta_X S_{edge}[\Gamma] = \frac{c}{96\pi}\int_{\mathbb{R}^2} X^\nu \partial_\mu (d\Gamma)^\mu{}_\nu, \tag{2.3.37}$$

where we assume $\partial M = \mathbb{R}$, and the conservation law of the edge energy-momentum tensor is modified as

$$\nabla_\mu T_{edge}{}^\mu{}_\nu = \frac{c}{96\pi\sqrt{g}}\varepsilon^{\lambda\tau}\partial_\mu\partial_\lambda\Gamma^\mu{}_{\tau\nu}. \tag{2.3.38}$$

We cannot derive the QTHE directly from this equation since the right-hand-side is of too high order in derivatives of the metric; i.e. it is of higher order than a temperature gradient. However, this edge anomaly supports the existence of chiral edge mode with the central charge c [45], and then we can derive the QTHE from the consideration of the energy current along the edges. To see it, we consider a finite sample of the two-dimensional TSC with broken time-reversal-symmetry, and it has a chiral edge mode with the central charge c and the Fermi velocity v_F as shown in Fig.2.12. We apply temperature gradient in the y-direction to the sample. Then the difference in the amount of the right-moving and left-moving energy current (J_1 and J_2, respectively), and therefore the net current in the x-direction occurs. Now we calculate this value. The current in the x-direction is given by

$$\begin{aligned}J_x =& J_1 - J_2 \\ =& v_F E_1(T_1) - v_F E_2(T_2),\end{aligned} \tag{2.3.39}$$

where E_1 and E_2 are the total energy of the right-moving and left-moving edge modes, respectively, and T_1 and T_2 represent the temperature of the edges. In the linear order

in $\delta T := T_1 - T_2$, we obtain

$$\begin{aligned} J_x =& \frac{v_F}{2}\left(\frac{\partial E_1(T)}{\partial T} + \frac{\partial E_2(T)}{\partial T}\right)\delta T \\ =& \frac{v_F}{2} C_T \delta T \end{aligned} \tag{2.3.40}$$

where $T = (T_1 + T_2)/2$ is the mean value of the temperature and C_T is the specific heat of the one dimensional helical mode, which is the sum of the two chiral edge modes. By using the technique of the conformal field theory [46] we obtain the value of this specific heat as

$$C_T = \frac{\pi c}{3 v_F} T. \tag{2.3.41}$$

Therefore the net current is given by

$$J_x = \frac{\pi c}{6} T \delta T, \tag{2.3.42}$$

and then the thermal Hall coefficient is

$$\kappa_{xy} = c\frac{\pi T}{6}. \tag{2.3.43}$$

Then the QTHE has been derived from the chiral Majorana edge theory.

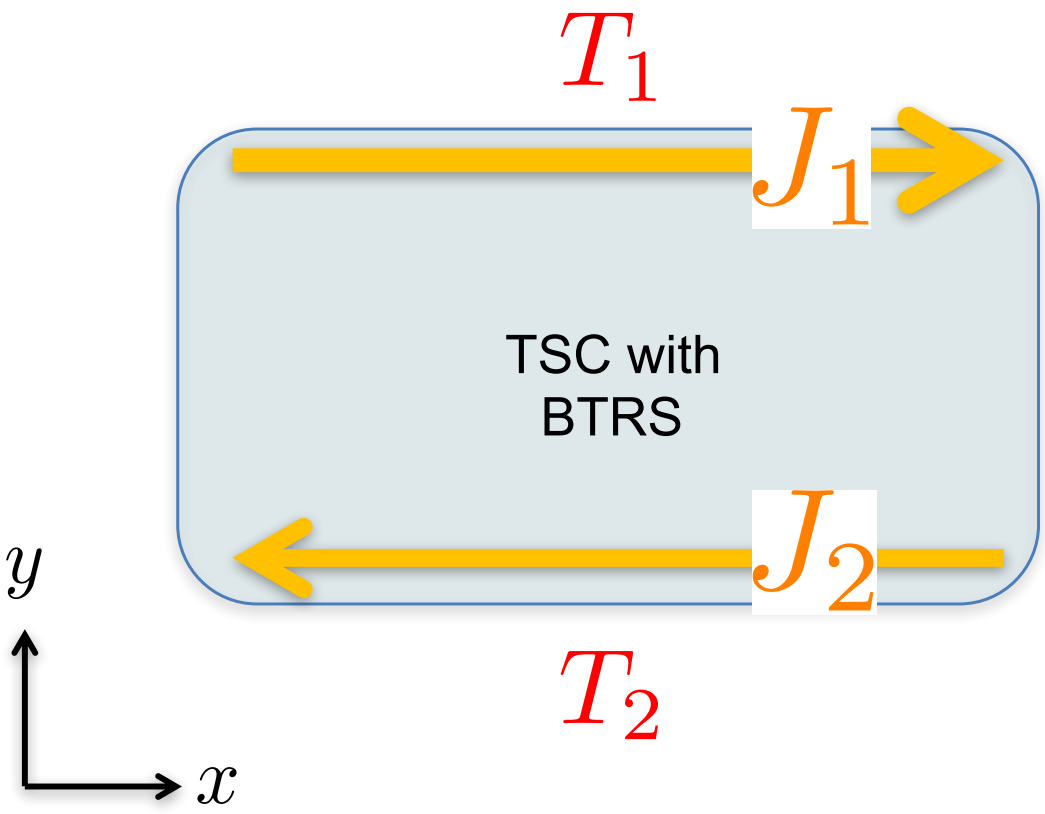

Figure 2.12: QTHE from edge picture. When temperature gradient is applied in the y-direction, the difference in the amount of the left-moving and right-moving energy current, and then the net current in the x-direction occurs.

3.1.3 Summary on QHE and QTHE

In this subsection, we have discussed the bulk and edge theories of the QHE and QTHE summarized in Fig.2.13. We have seen that the QHE can be derived by both bulk and edge theories, but the QTHE is more complicated. This point will be argued in Chapter 3.

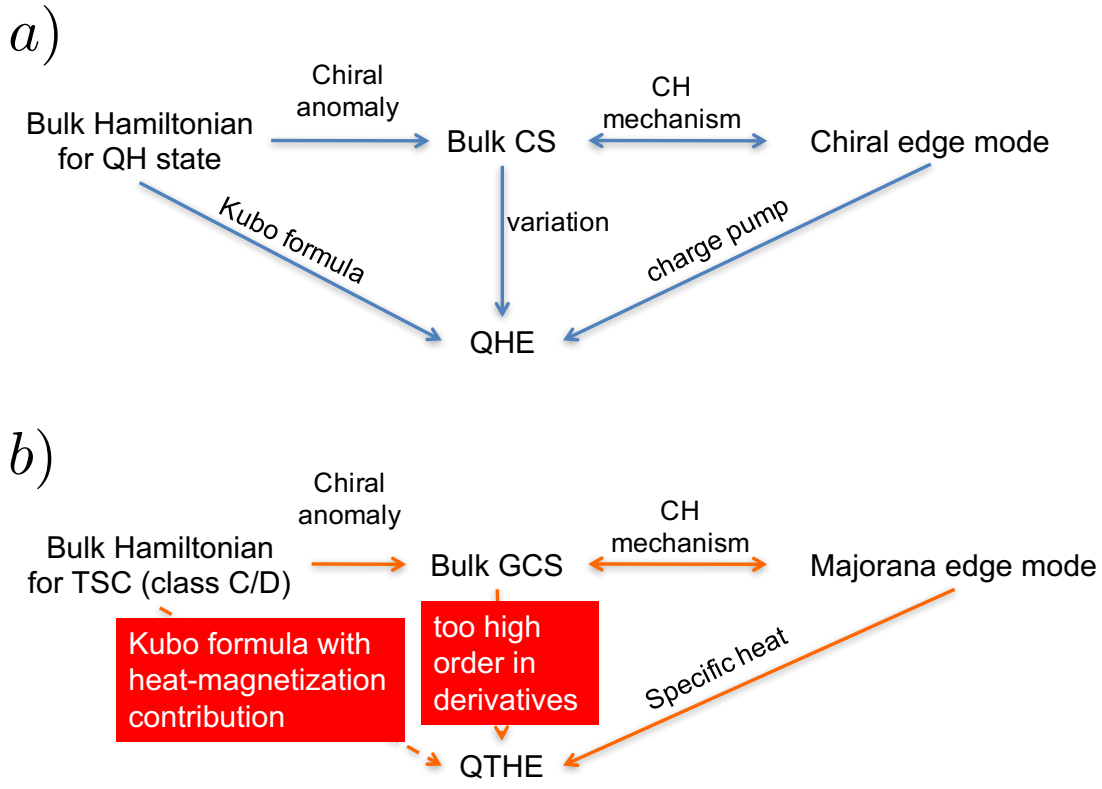

Figure 2.13: Bulk and edge theories of the QHE and QTHE.

3.2 Torsional chiral anomaly in Chern insulators

In the previous subsection, we have discussed the CS and GCS actions, which appear as the consequences of the chiral anomaly in the presence of field strength and curvature, respectively, and the topological responses due to these actions. Now, in this section, we argue the torsional analog of these actions, the torsional Chern-Simons (TCS) action, which is an effective action of the two-dimensional CI in the presence of torsions:

$$S_{TCS}[e^\alpha, \omega^\alpha{}_\beta] = \frac{\zeta_H}{2} \int_{\mathbb{R}\times M} \eta_{\alpha\beta} e^\alpha \wedge T^\beta, \tag{2.3.44}$$

or using the coefficients of the vielbeins and spin connection,

$$S_{TCS}[e^\alpha_\mu, \omega_\mu{}^\alpha{}_\beta] = \frac{\zeta_H}{2} \int_{\mathbb{R}\times M} d^2x dt \varepsilon^{\mu\nu\rho} \eta_{\alpha\beta} e^\alpha_\mu T^\beta_{\nu\rho}, \tag{2.3.45}$$

where $\mathbb{R}$ corresponds to the time axis and $M \subset \mathbb{R}^2$ is the domain of the sample. Here the coupling constant ζ_H has a mass dimension 2, where this point is different from

that in the cases of the CS (2.3.22) and GCS (2.3.35) actions [39].

By variation of this term with respect to the vielbein, we obtain the contribution to the energy-momentum tensor:

$$T^{\mu}_{\alpha} = \frac{1}{det(e)} \frac{\delta S_{TCS}}{\delta e^{\alpha}_{\mu}} = \frac{\zeta_H}{2} \eta_{\alpha\beta} \varepsilon^{\mu\nu\rho} T^{\beta}_{\nu\rho}. \tag{2.3.46}$$

Now we describe the physical interpretation of this contributions. In the presence of $T^{\bar{0}}_{20}$-type torsion, which corresponds to the temperature gradient as $T^{\bar{0}}_{i0} \sim -\partial_i \log T$ as mentioned in Sec.2.2.2, the energy current in the 1-direction is caused as $T^{1}_{\bar{0}} = \zeta_H T^{\bar{0}}_{20}$. This response is the thermal Hall effect [32]. We also discuss another type of the response called the Hall viscosity [47, 39, 37]. In the presence of $T^{\bar{1}}_{20}$, the momentum current is generated as $T^{1}_{\bar{1}} = \zeta_H T^{\bar{1}}_{20}$. As mentioned in Sec.2.2.3, we can realize this torsion by creating the inhomogeneity of the vector field as $T^{\bar{1}}_{20} = \partial_2 v^1$ (2.2.23) by shearing, rotating, or twisting the sample as shown in Fig.2.8. The momentum caused by these motions are shown in Fig.2.14.

The Hall viscosity has been discussed in 1995 by Avron et al. in quantum Hall systems by using the many-body Berry curvature generated by an adiabatic deformation of the metric of the real space [47]. Furthermore, recently, T. L. Hughes et al. have mentioned that the Hall viscosity can be described by the TCS action [39, 37].

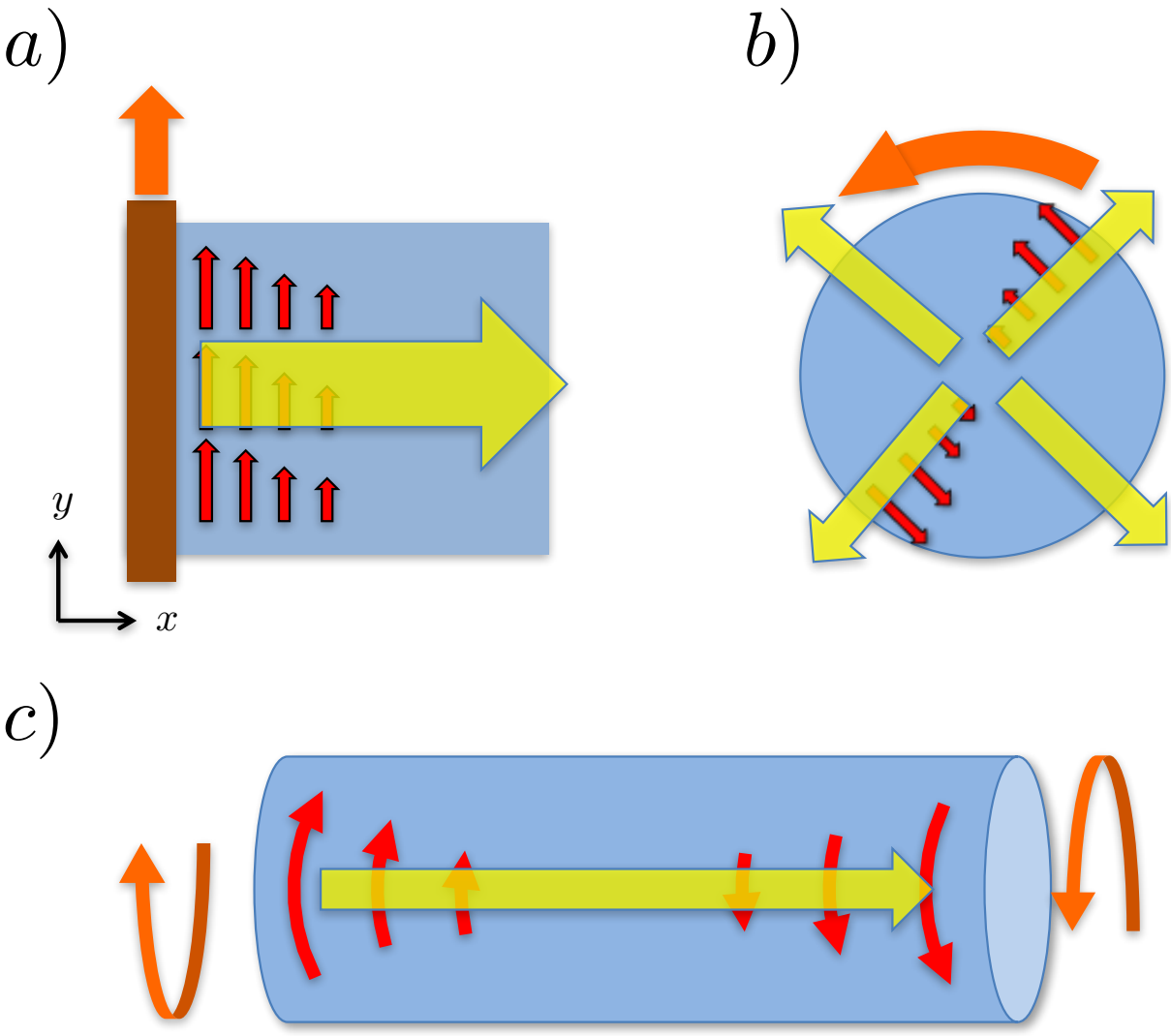

Figure 2.14: Hall viscosity due to the TCS term. The yellow arrows represent the momentum current. See also Fig.2.8.

3.3 Torsional chiral anomaly in Weyl semimetals

As described in Sec.1.2.1, the effective action of WSMs is the θ-term, which comes from the chiral anomaly in the presence of $U(1)$ gauge field. From this θ-term, we have derived the topological responses, the AHE and CME. In this section, we discuss their torsional analog, the torsional θ-term, or Nieh-Yan term [48, 49],

$$S_{T\theta}[e_\mu^\alpha, \omega_\mu{}^\alpha{}_\beta; \lambda_\mu] = \frac{\zeta_H}{4\pi}\int dx^3 dt |e(x)|\theta(x)\varepsilon^{\mu\nu\rho\lambda}\eta_{\alpha\beta}\left[T^\alpha_{\mu\nu}T^\beta_{\rho\lambda} - \eta_{\alpha\gamma}R^\alpha{}_{\gamma\mu\nu}e^\beta_\rho e^\gamma_\lambda\right] \quad (2.3.47)$$

with

$$\theta(x) = x^\mu \lambda_\mu. \tag{2.3.48}$$

Here $\pm\lambda_\mu$ are the energy and momentum of the Weyl points (see Sec.1.2.1) and ζ_H is the dimensional parameter (see Sec.2.3.2). From now on in this subsection, we will consider the case of $\omega_\mu{}^\alpha{}_\beta = 0$ for simplicity. Then, the contribution of the torsional θ-term to the energy-momentum tensor is

$$\begin{aligned} T^\mu_\alpha =& \frac{1}{|e|}\frac{\delta S_{T\theta}[e^\alpha_\mu]}{\delta e^\alpha_\mu} \\ =& \frac{\zeta_H}{2\pi}\varepsilon^{\mu\nu\rho\lambda}\eta_{\alpha\beta}\lambda_\nu T^\beta_{\rho\lambda}. \end{aligned} \tag{2.3.49}$$

Among the responses represented by this equation, the terms proportional to λ_i can be understood easily. Considering $\boldsymbol{\lambda} = (0, 0, \lambda_z)$, we obtain

$$\begin{aligned} T^\mu_\alpha =& \frac{2\lambda_z}{2\pi}\frac{\zeta_H}{2}\varepsilon^{\mu\rho\lambda}\eta_{\alpha\beta}T^\beta_{\rho\lambda} \\ =& \frac{1}{2\pi}\int_{-\lambda_z}^{\lambda_z} dk_z (2.3.46) \end{aligned} \tag{2.3.50}$$

This means that the contribution to the energy-momentum tensor of the torsional θ-term is the same as the integral of those of the CI layer between two Weyl nodes (see Fig.1.3) [33]. This situation is similar to the case of the AHE in WSMs described in Sec.1.2.1.1

On the other hand, the terms proportional to λ_0 represent intrinsically new phenomena. Especially, the phenomena represented by the $\alpha = a$ terms

$$T^i_a = \frac{\zeta_H}{2\pi}\varepsilon^{ijk}\lambda_0 T^a_{jk} \tag{2.3.51}$$

represents the generation of the momentum current caused by the dislocations, or TMF. Then, this effect is similar to the CME (Sec.1.2.1.2), which is the generation of the current caused by magnetic field, and therefore called the chiral heat effect [50].

4 Summary and motivations of our studies

We have introduced the formalism of the differential geometry in Sec.2.1. In Sec.2.2 we have shown that this formalism is useful for describing external forces to condensed

matter systems, such as applying a temperature gradient, making dislocation, twisting, and shearing. Furthermore, in Sec.2.3, we introduced its application to topological systems, such as the TIs, TSCs, WSMs, graphemes, and TCIs, and topological quantum transport phenomena related to quantum anomalies.

However, as mentioned in Sec.2.3.1, the theory on thermal transport phenomena in TSCs with broken time-reversal-symmetry remains unclear: the QTHE has been derived only from the chiral Majorana edge modes. Then, In Chapter.3, we will derive a general formula for the thermal Hall coefficient using the bulk Berry curvature, and the QTHE as a special case.

Moreover, geometrical responses in WSMs predicted in previous theoretical studies can be hardly observed in experiments. Indeed, in realistic lattice systems, momentum current is not conserved owing to broken translation symmetry, then, it is hard to observe the Hall viscosity or the chiral heat effect in WSMs (Sec.2.3.3). Accordingly, we will propose a new transport phenomena that is caused by dislocations in WSMs, referred to as the torsional chiral magnetic effect in Chapter 4. We will also propose experimental setups for its observation.

Chapter 3

Bulk approach for the thermal Hall effect in time-reversal-symmetry broken superconductor

In this chapter, we discuss the thermal Hall effect in superconductors with broken time-reversal-symmetry, by using the technique of the differential geometry described in the previous chapter. As introduced in Sec.2.3.1, the thermal Hall effect grasps the topological feature of two-dimensional TSCs with broken time-reversal-symmetry (i.e. class C and D TSCs in the topological periodic table [1]): the thermal Hall conductivity is quantized as $\kappa_{xy} = c\pi T/6$, where c is the central charge of the edge conformal field theory. This quantization has been derived from the edge conformal field theory [40]. On the other hand, from a bulk approach, the quantization of the thermal Hall conductivity has been derived in the case of two-dimensional Majorana fermions, which is related to two-dimensional spinless $p+ip$ superconductors [51]. [1] However, for more general cases of two-dimensional TSCs such as chiral d-wave superconductors and s-wave superconductors with the Rashba spin-orbit interaction [6, 7, 8], it has not been well understood how we can associate their TKNN numbers with the conformal field theory prediction mentioned above.

[1] In Ref. [51], it is shown that the thermal Hall conductivity of spinful Majorana fermions on the surface of a three-dimensional TSC is associated with the bulk TKNN number. Moreover, this model is related to that of spinless $p+ip$ superconductors via a unitary transformation: $c \equiv (\psi_\uparrow + i\psi_\downarrow)/\sqrt{2}, c^\dagger \equiv (\psi_\uparrow - i\psi_\downarrow)/\sqrt{2}$.

The reason is that it is complicated to calculate the thermal Hall coefficient because we have to calculate the value of the "heat (or energy) magnetization",[2] which contributes to the thermal Hall coefficient as well as the heat-current-heat-current four-point correlation function [44].

By solving this problem, we derive a formula for the thermal Hall coefficient of any superconductors with broken-time-reversal-symmetry at finite temperature, which can be applied even for nodal or three-dimensional superconductors (3.3.19). Furthermore, applying it to the two-dimensional TSC with broken time-reversal-symmetry, we derive that in the low-temperature limit, the thermal Hall coefficient is quantized as

$$\kappa_{xy} = \frac{C_1}{2}\frac{\pi T}{6}, \tag{3.0.1}$$

where C_1 is the Chern number of the BdG Hamiltonian of the superconductor. The edge theory of the TSC with the Chern number C_1 is the CFT with the central charge $c = C_1/2$. Therefore, this reproduces the results above. We note that it is one-half of the thermal Hall coefficient of the Chern insulators [52]:

$$\kappa_{xy}^{CI} = C_1\frac{\pi T}{6}. \tag{3.0.2}$$

We will show that this half-quantization is caused by the structure of the Nambu spinor and the particle-hole symmetry (PHS), which Bogoliubov-de Gennes (BdG) Hamiltonians generally have.

There are two important key points for the microscopic calculation of the thermal Hall conductivity: (i) we should take into account the energy conservation law properly, and (ii) the contributions from energy magnetization must be extracted to obtain transport currents as pointed out by Qin, Niu, and Shi [52].

For this purpose, we, first, clarify the symmetric properties which BdG Hamiltonians generally possess in Sec.3.1. Next, we define the energy current operator which preserves the continuity equation in Sec.3.2. Finally, we calculate the thermal Hall coefficients of TSCs by introducing gravitational fields which act as mechanical forces inducing heat currents, and by using the Kubo formula with corrections from energy magnetization contributions. The results in this chapter are based on Ref.[53].

[2]The chemical potential of the bogoliubov quasiparticles is measured from the fermi level, and set equal to 0. thus, the energy magnetization is equivalent to the heat magnetization.

1 Model, symmetry, and preliminaries

In this section, we introduce a model which describes 2D topological superconductors with broken time-reversal symmetry. The argument developed in this chapter is applicable to large classes of 2D topological superconductors such as chiral p-wave superconductors [40], chiral d-wave superconductors, and s-wave superconductors with the Rashba SOI under magnetic fields [6, 7, 8].

The Hamiltonian we start with is given by

$$\hat{\mathcal{H}} \equiv \int d^d r \hat{\psi}^\dagger(r) \frac{1}{2} H_{BdG}(r, \partial_r) \hat{\psi}(r), \tag{3.1.1}$$

where each operator has indices (a, s). $a(= \pm 1)$ is an index of the Nambu space and s is a spin index. $\hat{\psi}_{-1s}(r)$ and $\hat{\psi}_{1s}(r)$ are defined as $\hat{c}_s(r)$ and $\hat{c}_s^\dagger(r)$, respectively, where $\hat{c}_s(r)$ ($\hat{c}_s^\dagger(r)$) is an annihilation (creation) operator of an electron, and the BdG Hamiltonian H_{BdG} generally takes the form [54, 1]:

$$H_{BdG\, asa's'}(r, \partial_r) \equiv \begin{pmatrix} & (a'=-1) & (a'=+1) \\ (a=-1) & K_{ss'}(r, \partial_r) & -\Delta_{ss'}(r, \partial_r) \\ (a=+1) & \Delta^*_{ss'}(r, \partial_r) & -K^*_{ss'}(r, \partial_r) \end{pmatrix}, \tag{3.1.2}$$

where $K_{ss'}(r, \partial_r)$ and $\Delta_{ss'}(r, \partial_r)$ are operators including differential operators and functions of r. In the case where $K(r, \partial_r) = -\frac{1}{2m}\nabla^2 + V(r) - \mu$ and $\Delta(r, \partial_r) = -\hat{\Delta}(-i\partial_x - \partial_y)$ [$V(r)$ is a potential energy and $\hat{\Delta}$ is a complex constant], the model describes spinless chiral p-wave superconductors [40]. On the other hand, in the case where $K(r, \partial_r)_{ss'} = \{(-\frac{1}{2m}\nabla^2 + V(r))\delta_{ss'} - h\sigma_z + \boldsymbol{\sigma} \cdot \mathbf{g}(\partial_r)\}_{ss'}$ and $\Delta_{ss'}(r, \partial_r) = (-i\Delta\sigma_y)_{ss'}$ [h is a real constant, Δ is a complex constant, $\boldsymbol{\sigma} = (\sigma_x, \sigma_y, \sigma_z)$ are Pauli matrices, and $\mathbf{g}(\partial_r) = 2\lambda(-i\partial_y, i\partial_x, 0)$], the model describes s-wave superconductor with the Rashba spin-orbit interaction (SOI) [6, 7, 8].

For the derivation of the formula for the thermal Hall conductivity, it is useful to clarify the symmetry of our system. The BdG Hamiltonian is Hermitian and preserves the PHS:

$$H_{BdG\, as\, a's'} = -H^*_{BdG\, -as\, -a's'}. \tag{3.1.3}$$

Consequently, if $f_{as}(r)$ is the solution for the eigenvalue E, $f^*_{-as}(r)$ is the solution for the eigenvalue $-E$. As a result, if the system is periodic, the eigenfunctions for H_{BdG} can

be written as the form $f_{kn\,as}(r) = e^{ikr}u_{kn\,as}(r)$, where $u_{kn\,as}(r)$ has the same periodicity as the system, and the eigenenergys and eigenfunctions can preserve the symmetries

$$E_{kn} = -E_{-k-n}, \quad f_{kn\,as}(r) = f^*_{-k-n\,-as}(r). \tag{3.1.4}$$

We take $E_{nk}\,(n = 1, 2, 3\cdots)$ positive and $E_{nk}\,(n = -1, -2, -3\cdots)$ negative, and normalize the eigenfuctions so that

$$\sum_{as}\int d^d r f^*_{kn\,as}(r) f_{kn\,as}(r) = 1. \tag{3.1.5}$$

Now, we obtain the expressions for correlation functions of creation and annihilation operators of Bogoliubov quasiparticles, which are utilized in the following calculations. We introduce annihilation (creation) operators of Bogoliubov quasiparticles:

$$\hat{\psi}_{kn} \equiv \sum_{as}\int d^d r f^*_{kn\,as}(r)\hat{\psi}_{as}(r). \tag{3.1.6}$$

By using the symmetry Eq.(3.1.4), we can derive the symmetry of these operators

$$\hat{\psi}_{kn} = \hat{\psi}^\dagger_{-k-n} \tag{3.1.7}$$

and the anticommutation relations:

$$\left\{\hat{\psi}_{kn}, \hat{\psi}^\dagger_{k'n'}\right\} = \delta_{kk'}\delta_{nn'}, \tag{3.1.8}$$

$$\left\{\hat{\psi}_{kn}, \hat{\psi}_{k'n'}\right\} = \left\{\hat{\psi}^\dagger_{kn}, \hat{\psi}^\dagger_{k'n'}\right\} = \delta_{k-k'}\delta_{n-n'}. \tag{3.1.9}$$

(Note that the latter is nonzero.) Since the Hamiltonian can be transformed into $\hat{\mathcal{H}} = \frac{1}{2}\sum_{kn} E_{kn}\hat{\psi}^\dagger_{kn}\hat{\psi}_{kn} = \sum_{kn,n>0} E_{kn}\hat{\psi}^\dagger_{kn}\hat{\psi}_{kn} + (\mathrm{c-number})$, we get the expressions for correlation functions:

$$\langle\hat{\psi}_{kn}\hat{\psi}_{k'n'}\rangle = f(E_{k'n'})\delta_{n-n'}\delta_{k-k'} = (1 - f(E_{kn}))\delta_{n-n'}\delta_{k-k'}, \tag{3.1.10}$$

$$\langle\hat{\psi}^\dagger_{kn}\hat{\psi}_{k'n'}\rangle = f(E_{k'n'})\delta_{nn'}\delta_{kk'}, \tag{3.1.11}$$

$$\langle\hat{\psi}_{kn}\hat{\psi}^\dagger_{k'n'}\rangle = (1 - f(E_{k'n'}))\delta_{nn'}\delta_{kk'}, \tag{3.1.12}$$

$$\langle\hat{\psi}^\dagger_{kn}\hat{\psi}^\dagger_{k'n'}\rangle = (1 - f(E_{k'n'}))\delta_{n-n'}\delta_{k-k'} = f(E_{kn})\delta_{n-n'}\delta_{k-k'}, \tag{3.1.13}$$

where the function $f(E) = 1/(e^{\beta E} + 1)$ is the Fermi distribution function at the temperature $T = 1/\beta$ and the chemical potential $\mu = 0$, and $\langle\hat{X}\rangle$ is the the statical average

of the operator $\hat{X}$: $\langle\hat{X}\rangle \equiv \mathrm{Tr}\left[e^{-\beta\hat{\mathcal{H}}}\hat{X}\right]/\mathrm{Tr}\left[e^{-\beta\hat{\mathcal{H}}}\right]$. Applying Wick's theorem, we get the expression for the four-point correlation function:

$$\begin{aligned}\langle\hat{\psi}^\dagger_{k_1n_1}\hat{\psi}_{k_2n_2}\hat{\psi}^\dagger_{k'_1n'_1}\hat{\psi}_{k'_2n'_2}\rangle &= f(E_2)f(E_{2'})\delta_{12}\delta_{1'2'} \\ &+ f(E_1)(1-f(E_2))(\delta_{12'}\delta_{21'}-\delta_{1-1'}\delta_{2-2'}),\end{aligned} \tag{3.1.14}$$

where E_1, δ_{12} and δ_{1-2} are the abbreviations for $E_{k_1n_1}$, $\delta_{k_1k_2}\delta_{n_1n_2}$ and $\delta_{k_1-k_2}\delta_{n_1-n_2}$ respectively. Note that the last term of Eq.(3.1.14), $-\delta_{1-1'}\delta_{2-2'}$, does not appear in the four-point correlation function of the systems of ordinary fermions, and is inherent for the Nambu spinor. This term plays an important role for the derivation of the half-quantized thermal Hall conductivity as shown in the following.

2 Energy current operator

In general, for the microscopic argument on transport phenomena, it is important to define correctly the "charge" and "current" field operators which satisfy the continuity equation. Therefore, in this section, to consider thermal transport, we define the energy density operator and the energy current operator. To apply the linear response theory, we introduce a gravitational field which gives rise to mechanical forces inducing heat current flow [34].

First, we, for simplicity, restrict the form of the BdG Hamiltonian to

$$H_{BdG}(r,\partial_r) = \sum_{ij} A_{ij}\partial_i\partial_j + \sum_i\{B_i(r)i\partial_i + i\partial_i B_i^\dagger(r)\} + C(r). \tag{3.2.1}$$

A_{ij} is a constant Hermitian [i.e. $(A^\dagger_{ij})_{as\,a's'} \equiv (A_{ij})^*_{a's'\,as} = (A_{ij})_{as\,a's'}$] matrix which preserves $A_{ij} = A_{ji}$, and the first term includes the kinetic energy and the superconducting gap which includes second-order differential operators. $C(r)$ is a Hermitian-matrix-valued function of r, and includes the periodic potentials, the superconducting gap, the Zeeman energy, and so on. $B_i(r)$ is a matrix-valued function of r which is raised by gauge potentials, the spin-orbit interactions, or superconducting gap which includes first-order differential operators. Now we can get the equation: $\sum_i\{B_i(r)i\partial_i + i\partial_i B_i^\dagger(r)\} = \sum_i\{\tilde{B}_i(r)i\partial_i + i\partial_i\tilde{B}_i(r)) + [\partial_i, \tilde{B'}_i(r)]\}$, where $\tilde{B}_i(r)$ and $\tilde{B'}_i(r)$ are Hermitian matrices: $B_i(r) = \tilde{B}_i(r) + i\tilde{B'}_i(r)$, and the last term of the RHS of the equation is noting but a Hermitian matrix, so it can be absorbed into $C(r)$. Therefore, we take

$B_i(r)$ Hermitian. Note that the Hamiltonians of the models mentioned above, the models of chiral p-wave (or d-wave) superconductors and s-wave superconductors with the Rashba SOI, are expressed in the form Eq.(3.2.1). From the the Hamiltonian Eq.(3.2.1), we define the velocity operator :

$$v_i \equiv i\left[H_{BdG}, r_i\right]. \tag{3.2.2}$$

v_i is Hermitian and preserves PHS:

$$v_{i\,asa's'} = +v^*_{i\,-as-a's'}. \tag{3.2.3}$$

(Note the sign "+").

Next, we define the energy density operator and the energy current operator. By using the method of integration by parts, the Hamiltonian $\hat{\mathcal{H}}$ can be rewritten as

$$\hat{\mathcal{H}} = \int d^d r\, \hat{h}(r), \tag{3.2.4}$$

where

$$\hat{h}(r) \equiv \frac{1}{2}\left\{-(\partial_i\hat{\psi})^\dagger(A_{ij}\partial_j\hat{\psi}) + \hat{\psi}^\dagger(B_i i\partial_i\hat{\psi}) + (B_i i\partial_i\hat{\psi})^\dagger\hat{\psi} + \hat{\psi}^\dagger(C\hat{\psi})\right\} \tag{3.2.5}$$

is the Hamiltonian density operator and Hermitian [i.e $\hat{h}^\dagger(r) = \hat{h}(r)$]. Here $(\partial_i\hat{\psi})^\dagger(A_{ij}\partial_j\hat{\psi})$ is the abbreviation for $\sum_{ij\,asa's'}(\partial_i\hat{\psi}_{as})^\dagger\{(A_{ij})_{as\,a's'}\partial_j\hat{\psi}_{a's'}\}$. A similar abbreviation is used for other terms. Therefore, in the presence of a gravitational field $\phi(r)$ (see Sec.2.2.2). The Hamiltonian density operator and the Hamiltonian of the whole system are transformed into

$$\hat{h}_\phi(r) \equiv (1+\phi(r))\hat{h}(r), \tag{3.2.6}$$

$$\hat{\mathcal{H}}_\phi \equiv \int d^d r \hat{h}_\phi(r) = \int d^d r \hat{\psi}^\dagger H_\phi \hat{\psi}, \tag{3.2.7}$$

where

$$H_\phi(r,\partial_r) \equiv \frac{1}{2}\left[\sum_{ij} A_{ij}\partial_i(1+\phi)\partial_j + \sum_i\{(1+\phi)B_i(r)i\partial_i\right. \tag{3.2.8}$$

$$\left. + i\partial_i(1+\phi)B_i(r)\} + (1+\phi)C(r)\right]. \tag{3.2.9}$$

Note the scaling relation $H_\phi|_{\phi=0} = \frac{1}{2}H_{BdG}$.

Now we define the energy current operator of the system with a gravitational field as follows,

$$\hat{j}_{E\phi i}(r) \equiv \frac{1}{2}\left[\frac{1}{2}(1+\phi(r))\left\{(v_i\hat{\psi})^\dagger(2H_\phi\hat{\psi})+h.c.\right\}\right.$$
$$\left.-\varepsilon_{ijk}\partial_j\left\{(1+\phi(r))^2\hat{\Lambda}_k\right\}\right], \tag{3.2.10}$$

where

$$\hat{\Lambda}_i \equiv \frac{1}{8i}\varepsilon_{ijk}(v_j\hat{\psi})^\dagger(v_k\hat{\psi}).$$

The last term of Eq.(3.2.10) is indispensable for preserving the scaling law [52]:

$$\hat{j}_{E\phi i}(r) = (1+\phi(r))^2\hat{j}_{Ei}(r), \tag{3.2.11}$$

where

$$\hat{j}_{Ei}(r) \equiv \hat{j}_{E\phi i}(r)\Big|_{\phi=0} = \frac{1}{2}\left\{\frac{1}{2}(v_i\hat{\psi})^\dagger(H_{BdG}\hat{\psi})+h.c.-\varepsilon_{ijk}\partial_j\hat{\Lambda}_k\right\}. \tag{3.2.12}$$

We can check that the scaling law Eq. (3.2.11) actually holds by a straightforward calculation with paying attention to $H_\phi = (1+\phi)\frac{1}{2}H_{BdG} - \frac{i}{4}(\partial_i\phi)v_i$.

These Hamiltonian density and energy current operators Eqs. (3.2.6) and (3.2.10) indeed satisfy the continuity equation:

$$\frac{\partial\hat{h}_\phi(r)}{\partial t} \equiv -i\left[\hat{h}_\phi(r),\hat{\mathcal{H}}_\phi\right] = -\sum_i\frac{\partial\hat{j}_{\phi i}(r)}{\partial r_i}. \tag{3.2.13}$$

We present a brief proof of the continuity equation (3.2.13) in the following. By noting the equations

$$\dot{\hat{\psi}} = -i\left[\hat{\psi},\hat{\mathcal{H}}_\phi\right] = -2iH_\phi\hat{\psi} \tag{3.2.14}$$

and

$$v_i = 2iA_{ij}\partial_j - 2B_i, \tag{3.2.15}$$

we can get

$$\dot{\hat{h}}_\phi = (1+\phi)\{-\frac{1}{2}(v_i\hat{\psi})^\dagger(\partial_iH_\phi\hat{\psi}) - (B_i\partial_i\hat{\psi})^\dagger(H_\phi\hat{\psi}) - i(C\hat{\psi})^\dagger(H_\phi\hat{\psi})\} \tag{3.2.16}$$
$$+ h.c.\,. \tag{3.2.17}$$

On the other hand, by noting the equation

$$\partial_i(1+\phi)v_i = 4i\left[H_\phi - \frac{i}{2}B_i(1+\phi)\partial_i - \frac{1}{2}(1+\phi)C\right], \tag{3.2.18}$$

we get the equation:

$$\begin{aligned}
\partial_i\hat{j}_{E\phi i} =& \frac{1}{4}\left[\left\{\partial_i(1+\phi(r))v_i\hat{\psi}\right\}^\dagger(2H_\phi\hat{\psi}) + ((1+\phi(r))v_i\hat{\psi})^\dagger(\partial_i 2H_\phi\hat{\psi})\right] && (3.2.19)\\
&+ h.c. && (3.2.20)\\
=&(1+\phi)\{\frac{1}{2}(v_i\hat{\psi})^\dagger(\partial_i H_\phi\hat{\psi}) + (B_i\partial_i\hat{\psi})^\dagger(H_\phi\hat{\psi}) + i(C\hat{\psi})^\dagger(H_\phi\hat{\psi})\} && (3.2.21)\\
&+ h.c.\,. && (3.2.22)
\end{aligned}$$

Therefore, we obtain the continuity equation Eq.(3.2.13).

Using the energy current operator Eq.(3.2.10) satisfying the conservation law, we calculate the thermal Hall conductivity in the next section.

3 Thermal Hall conductivity

In this section, we calculate the thermal Hall conductivity of superconductors using the procedure which was introduced by Qin, Niu and Shi [52], with a particular attention to the symmetry of the eigenfunction Eq.(3.1.4) and compare the result with the case of normal metals and band insulators.

The thermal Hall conductivity is given as follows:

$$\kappa_{xy}^{tr} = \kappa_{xy}^{Kubo} + \frac{2M_E^z}{TV}. \tag{3.3.1}$$

The first term is given by the usual Kubo formula [34], and M_E^z is the gravitomagnetic energy (heat) magnetization, which characterizes the circulation of the energy (heat) flow.

From now on, we use a bra-ket notation:

$$\langle f|\mathcal{O}|g\rangle \equiv \sum_{asa's'}\int d^dr f_{as}^*(r)\mathcal{O}_{asa's'}(r,\partial_r)g_{a's'}(r). \tag{3.3.2}$$

Now we introduce new operators, which are the Fourier transforms of the field

operators, and expand them in the operators $\hat{\psi}_{kn}$ and $\hat{\psi}^{\dagger}_{kn}$:

$$\hat{h}_{-q} \equiv \int d^d r e^{-i(-q)r} \hat{h}(r) = \sum_{kn\,k'n'} \hat{\psi}^{\dagger}_{kn} \hat{\psi}_{k'n'} h_{-q\,kn\,k'n'}, \tag{3.3.3}$$

$$\hat{j}_{E\,q\,i} \equiv \int d^d r e^{-iqr} \hat{j}_{Ei}(r) = \sum_{kn\,k'n'} \hat{\psi}^{\dagger}_{kn} \hat{\psi}_{k'n'} j_{E\,q\,x\,kn\,k'n'}, \tag{3.3.4}$$

where

$$h_{-q\,kn\,k'n'} \equiv \frac{1}{2} \langle f_{kn} | \frac{H_{BdG} e^{iqr} + e^{iqr} H_{BdG}}{2} | f_{k'n'} \rangle + \mathcal{O}(q^2) \qquad (as \quad q \to 0), \tag{3.3.5}$$

$$\begin{aligned} j_{E\,q\,j\,kn\,k'n'} \equiv \frac{1}{2} \Bigg[& \frac{\langle H_{BdG} f_{kn} | e^{-iqr} | v_j f_{k'n'} \rangle + \langle v_j f_{kn} | e^{-iqr} | H_{BdG} f_{k'n'} \rangle}{2} \\ & - \frac{1}{8i} \sum_i \Big\{ \langle \partial_i v_j f_{kn} | e^{-iqr} | v_i f_{k'n'} \rangle + \langle v_j f_{kn} | e^{-iqr} | \partial_i v_i f_{k'n'} \rangle \\ & - \langle \partial_i v_i f_{kn} | e^{-iqr} | v_j f_{k'n'} \rangle - \langle v_i f_{kn} | e^{-iqr} | \partial_i v_j f_{k'n'} \rangle \Big\} \Bigg], \end{aligned} \tag{3.3.6}$$

which can be obtained by noting the two identities:

$$A_{ij} \partial_i e^{iqr} \partial_j = \frac{A_{ij} \partial_i \partial_j e^{iqr} + e^{iqr} A_{ij} \partial_i \partial_j}{2} + \mathcal{O}(q^2) \tag{3.3.7}$$

and

$$e^{-iqr} B_i i \partial_i + i \partial_i B_i e^{-iqr} = \frac{e^{-iqr}(B_i i \partial_i + i \partial_i B_i) + (B_i i \partial_i + i \partial_i B_i) e^{-iqr}}{2}. \tag{3.3.8}$$

Note that the coefficients for the expansion, $h_{-q\,kn\,k'n'}$ and $j_{E\,q\,j\,kn\,k'n'}$, preserve the symmetries

$$h_{-q\,kn\,k'n'} = -h_{-q\,-k'\,-n'\,-k\,-n}, \tag{3.3.9}$$

$$j_{E\,q\,j\,kn\,k'n'} = -j_{E\,q\,j\,-k'\,-n'\,-k\,-n}, \tag{3.3.10}$$

which follow form $H_{BdG\,as\,a's'} = -H^{*}_{BdG\,-as\,-a's'}$ and $v_{i\,asa's'} = v^{*}_{i\,-as\,-a's'}$, and Eq.(3.1.4): $f_{kn\,as}(r) = f^{*}_{-k\,-n\,-as}(r)$.

The first term of Eq.(3.3.1) is give by

$$\kappa^{Kubo}_{xy} = \frac{1}{VT^2} \int_0^{\infty} dt e^{-0t} \langle \hat{J}_{Ey}; \hat{J}_{Ex}(t) \rangle, \tag{3.3.11}$$

where $\hat{J}_{Ei} \equiv \hat{j}_{E\,q\,i}\Big|_{q=0}$, $\langle \hat{a}; \hat{b} \rangle \equiv 1/\beta \int_0^\beta d\lambda \langle \hat{a}(-i\lambda)\hat{b} \rangle$, $\hat{a}(t) \equiv e^{i\hat{\mathcal{H}}t}\hat{a}e^{-i\hat{\mathcal{H}}t}$, and V is the volume of the system. By the formula for the four-point correlation function (3.1.14) and the symmetry of the coefficient (3.3.10), we get

$$\kappa_{xy}^{Kubo} = -\frac{1}{VT^2} \sum_{\substack{kn\,k'n' \\ (kn)\neq(k'n')}} \frac{f(E_{kn}) - f(E_{k'n'})}{i(E_{kn} - E_{k'n'})^2} \times J_{Ey\,kn\,k'n'}(J_{Ex\,k'n'\,kn} - J_{Ex\,-k-n\,-k'-n'}) \tag{3.3.12}$$

$$= -\frac{2}{VT^2} \sum_{\substack{kn\,k'n' \\ (kn)\neq(k'n')}} \frac{f(E_{kn}) - f(E_{k'n'})}{i(E_{kn} - E_{k'n'})^2} J_{Ey\,kn\,k'n'} J_{Ex\,k'n'\,kn}, \tag{3.3.13}$$

where $J_{Ei\,kn\,k'n'} \equiv j_{E\,q\,j\,kn\,k'n'}\big|_{q=0}$. The factor 2 in front of Eq.(3.3.13) is a result of the PHS.

Moreover, by calculating in the manner similar to Ref. [52], we obtain

$$\kappa_{xy}^{Kubo} = \frac{1}{4TV} \sum_{kn} \mathrm{Im} \left\langle \frac{\partial u_{kn}}{\partial k_x} \middle| (H_{BdG\,k} + E_{kn})^2 \middle| \frac{\partial u_{kn}}{\partial k_y} \right\rangle f(E_{kn}), \tag{3.3.14}$$

where $H_{BdG\,k} \equiv e^{-ikr} H_{BdG} e^{ikr}$.

Next we calculate the gravitational magnetization M_E^z. It is the solution of the differential equation

$$2M_E^z - T\frac{\partial M_E^z}{\partial T} = \frac{\beta}{2i} \left\{ \frac{\partial}{\partial q_x} \langle \hat{h}_{-q}; \hat{j}_{E\,q\,y} \rangle - \frac{\partial}{\partial q_y} \langle \hat{h}_{-q}; \hat{j}_{E\,q\,x} \rangle \right\} \Big|_{q\to 0}. \tag{3.3.15}$$

with a boundary condition $\lim_{T\to 0} T\frac{\partial M_E^z}{\partial T} = 0$. In order to evaluate it, we also carry out a calculation similar to Ref. [52], with paying attention to the last extra term of Eq.(3.1.14) and the symmetries (3.3.10). We get

$$M_E^z = -\frac{1}{4} \sum_{kn} \left[\frac{1}{2} \mathrm{Im} \left\langle \frac{\partial u_{kn}}{\partial k_x} \middle| (H_{BdG\,k} + E_{kn})^2 \middle| \frac{\partial u_{kn}}{\partial k_y} \right\rangle f(E_{kn}) - 2E_{kn}^2 \mathrm{Im} \left\langle \frac{\partial u_{kn}}{\partial k_x} \middle| \frac{\partial u_{kn}}{\partial k_y} \right\rangle f(E_{kn}) + 4\mathrm{Im} \left\langle \frac{\partial u_{kn}}{\partial k_x} \middle| \frac{\partial u_{kn}}{\partial k_y} \right\rangle \int_0^{E_{kn}} x f(x) dx \right]. \tag{3.3.16}$$

In the end, we obtain an expression for the thermal Hall coefficient:

$$\kappa_{xy}^{tr} = -\frac{1}{TV} \int dE E^2 \sum_{\substack{kn \\ E_{kn}\le E}} \mathrm{Im} \left\langle \frac{\partial u_{kn}}{\partial k_x} \middle| \frac{\partial u_{kn}}{\partial k_y} \right\rangle f'(E), \tag{3.3.17}$$

or using the Berry curvature of the BdG Hamiltonian,

$$b_z(k,n) \equiv 2\mathrm{Im}\left\langle \frac{\partial u_{kn}}{\partial k_x} \middle| \frac{\partial u_{kn}}{\partial k_y} \right\rangle, \tag{3.3.18}$$

$$\kappa_{xy}^{tr} = -\frac{1}{2TV}\int dE E^2 \sum_{\substack{kn \\ E_{kn}\leq E}} b_z(k,n) f'(E), \tag{3.3.19}$$

Moreover, by using the Sommerfeld expansion, we obtain an expression in the low-temperature limit:

$$\kappa_{xy}^{tr} = \frac{C_1(0)}{2}\frac{\pi T}{6}, \tag{3.3.20}$$

where $C_1(E)$ is the TKNN number, which is an integer when the energy E lies in the energy gap [2, 55], and it is given by,

$$C_1(E) \equiv \sum_n \int \frac{d^2k}{2\pi} b_z(k,n) H(E - E_{kn}), \tag{3.3.21}$$

where $H(x)$ is the Heaviside step function.

It is notable that the quantization value $\frac{1}{2}\frac{\pi T}{6}C_1(0)$ is exactly one half of the value of the Chern insulator (or the IQHE state). In the case of spineless chiral p-wave superconductors, the TKNN number $C_1(0)$ is equal to ± 1[56], and thus, this result is in agreement with the result obtained from the conformal field theory with central charge $c = 1/2$ for the edge state [40, 51].

4 Summary

We have derived the formula for the thermal Hall coefficient of any superconductors with broken time-reversal-symmetry at finite temperature from bulk calculations. Applying it to two-dimensional TSCs with broken time-reversal-symmetry, we have demonstrated that their thermal Hall conductivity is quantized: $\kappa_{xy} = \frac{C_1}{2}\frac{\pi T}{6}$, where C_1 is the TKNN number of the BdG Hamiltonian. Our approach, solely, relies on bulk calculations, without referring to the Majorana edge theory. This value $\frac{C_1}{2}\frac{\pi T}{6}$ is one half of the thermal Hall conductivity in the case of the Chern insulator (or the IQHE state). In the derivation of this result, the PHS, which BdG Hamiltonians generally possess, plays an important role. Our result is in perfect agreement with that obtained from the conformal field theory which describes the edge state of two-dimensional TSCs.

Chapter 4

Torsional chiral magnetic effect in a Weyl semimetal with a topological defect

In this chapter, we propose a torsional response raised by lattice dislocation in WSMs akin to the CME referred to as the torsional chiral magnetic effect (TCME): a fictitious magnetic field arising from screw or edge dislocation induces charge current. First, in Sec.4.1, we investigate this effect from the method based on the linear response theory of curved spacetime describe in Chapter 2. We also describe this effect from other methods based on the calculation of the ground state wave functions in the presence of dislocations in Sec.4.2. Furthermore, in Secs.4.3 and 4.4, we perform a tight-binding simulation, and confirm that the TCME exists even for realistic lattice systems, which vanishes in real solid state materials as mentioned in Sec.1.2.1.2. In Sec.4.5, we also propose the experimental setups for the detection of this effect via SQUID and nonlocal resistivity measurements in WSM materials. These results are based on Ref.[20].

1 Linear response theory based on field theory in curved space-time

In this section, using the linear response theory with the Cartan formalism described in Chapter 2, we investigate the TCME in WSMs due to dislocation. Furthermore we

describe the physical interpretations of the TCME.

1.1 Calculation from the linear response theory

First, in Sec.4.1.1.1, we derive Berry-phase formulae for the charge and current density corrections due to magnetic fields and TMFs, which are expressed as the Berry curvature and intrinsic magnetic moment. These formulae can be applied to any materials. Furthermore we apply them to a linearized low energy effective model of a WSM and derive the torsional chiral magnetic effect in Sec.4.1.1.2.

1.1.1 Berry-phase formula

The effective action S_{eff} in the presence of the external fields, which we begin with, is defined as

$$S_{\text{eff}}[A_\mu, e_\mu^\alpha] := \log\left[\int \mathcal{D}\psi\mathcal{D}\psi^\dagger \exp\left(-S[\psi,\psi^\dagger,A_\mu,e_\mu^\alpha]\right)\right], \tag{4.1.1}$$

with

$$\begin{aligned} S[\psi,\psi^\dagger,A_\mu,e_\mu^\alpha] &:= \frac{1}{2}\int d\tau d^3r \left[\psi^\dagger(\tau,\boldsymbol{r})\hat{\mathcal{L}}\psi(\tau,\boldsymbol{r}) + c.c.\right], \\ \hat{\mathcal{L}} &:= |e(\boldsymbol{r})|[\partial/\partial\tau - \hat{H}(-i\nabla_a) - eA_0(\boldsymbol{r})], \end{aligned} \tag{4.1.2}$$

where ψ is the fermionic field, τ and $\boldsymbol{r}$ denote the imaginary time and spatial coordinate, respectively, and A_μ and e_μ^α are the vector potential and vielbein, respectively. Here $c.c.$ represents the complex conjugate combined with the change of the sign of the derivative operator $\partial/\partial\tau$. In Eq.(4.1.2), only the spatial components of the vielbein which cause the torsional magnetic field is included, $e_\mu^\alpha = \delta_0^\alpha\delta_\mu^0 + \delta_a^\alpha\delta_\mu^i e_i^a(\boldsymbol{r})$, while we consider both the spatial and temporal components of the vector potential. However, the temporal one is introduced only for the purpose of the probe field for the calculation of the charge density, which is set to be zero after the variation. Also, in Eq.(4.1.2), the Jacobian is given by $|e(\boldsymbol{r})| := \det e_i^a(\boldsymbol{r})$, and the covariant derivative is $-i\nabla_a := e_a^j(\boldsymbol{r})(-i\partial_j - eA_j(\boldsymbol{r}))$ with $a = \bar{i}$. The charge density and the current density are defined by,

$$j^\alpha(\boldsymbol{r}) := -\frac{e_\mu^\alpha(\boldsymbol{r})}{|e(\boldsymbol{r})|}\frac{\delta S_{\text{eff}}}{\delta A_\mu(\boldsymbol{r})}. \tag{4.1.3}$$

Using the gradient expansion method (the details of the calculation is described in Sec.4.7), the expressions for the charge and current density up to the first order of the magnetic field and the torsional magnetic field are given by,

$$\begin{aligned} j^0(\boldsymbol{r}) =& e\sum_n \int \frac{d^3\boldsymbol{\pi}}{(2\pi)^3}\,[n_F(\varepsilon_{n,\boldsymbol{\pi}}) \\ & - \boldsymbol{\Omega}^n(\boldsymbol{\pi})\cdot(e\boldsymbol{B}(\boldsymbol{r}) + \boldsymbol{T}^a(\boldsymbol{r})\pi_a) n_F(\varepsilon_{n,\boldsymbol{\pi}}) \\ & - \boldsymbol{m}^n(\boldsymbol{\pi})\cdot(e\boldsymbol{B}(\boldsymbol{r}) + \boldsymbol{T}^a(\boldsymbol{r})\pi_a) n_F'(\varepsilon_{n,\boldsymbol{\pi}})] \end{aligned} \tag{4.1.4}$$

$$\begin{aligned} \boldsymbol{j}(\boldsymbol{r}) =& e\sum_n \int \frac{d^3\boldsymbol{\pi}}{(2\pi)^3}\,[\boldsymbol{v}^n(\boldsymbol{\pi}) n_F(\varepsilon_{n,\boldsymbol{\pi}}) \\ & - (\boldsymbol{v}^n(\boldsymbol{\pi})\cdot\boldsymbol{\Omega}^n(\boldsymbol{\pi}))\,(e\boldsymbol{B}(\boldsymbol{r}) + \boldsymbol{T}^a(\boldsymbol{r})\pi_a) n_F(\varepsilon_{n,\boldsymbol{\pi}})]\,. \end{aligned} \tag{4.1.5}$$

Here, π^a is the mechanical (gauge invariant) momentum, n is the band index, $\varepsilon_{n,\boldsymbol{\pi}}$ is the energy, $v^{n,a}(\boldsymbol{\pi}) := \partial\varepsilon_{n,\boldsymbol{\pi}}/\partial\pi_a$ is the group velocity, and $n_F(\varepsilon)$ is the Fermi distribution function. The Berry curvature and intrinsic magnetic moment [57, 58] are given by

$$\Omega^{na}(\boldsymbol{\pi}) := -i\varepsilon^{abc}\left\langle \frac{\partial u^n_{\boldsymbol{\pi}}}{\partial\pi_b}\,\middle|\,\frac{\partial u^n_{\boldsymbol{\pi}}}{\partial\pi_c}\right\rangle \tag{4.1.6}$$

and

$$m^{na}(\boldsymbol{\pi}) := \frac{i}{2}\varepsilon^{abc}\left\langle \frac{\partial u^n_{\boldsymbol{\pi}}}{\partial\pi_b}\,\middle|\,[H_0(\boldsymbol{\pi}) - \varepsilon_{n,\boldsymbol{\pi}}]\,\middle|\,\frac{\partial u^n_{\boldsymbol{\pi}}}{\partial\pi_c}\right\rangle, \tag{4.1.7}$$

respectively, where H_0 is the Hamiltonian without external fields and $|u^n_{\boldsymbol{\pi}}\rangle$ is its Bloch wave function. The TMF is defined by $T^a_i := (1/2)\varepsilon^{ijk}T^a_{jk}$, like the magnetic field $B_i := (1/2)\varepsilon^{ijk}F_{jk}$.

When the TMF is absent, the Berry-phase formulae (4.1.4) and (4.1.5) reproduce the previous theoretical results. Indeed, the second term in Eq.(4.1.4) corresponds to the modification of the density of state due to the inter product of the Berry curvature and magnetic field, $e\boldsymbol{\Omega}^n\cdot\boldsymbol{B}$, and the third term the energy correction due to the coupling of the intrinsic magnetic moment and magnetic field, $\varepsilon_{n,\boldsymbol{\pi}} \to \varepsilon_{n,\boldsymbol{\pi}} - e\boldsymbol{m}^n\cdot\boldsymbol{B}$ [58]. Furthermore, the second term in Eq.(4.1.5) corresponds to the CME, which was derived from the kinetic equation with the Berry curvature by Son and Yamamoto [59]. On the other hand, the terms including the torsional magnetic field $\boldsymbol{T}^a$ are new terms, raising the TCME for Weyl semimetals. It is noted that the commutator of the covariant derivatives with both the vector potential and vielbein leads to the torsional magnetic field as well as the magnetic field, i.e. $-i[-i\nabla_a, -i\nabla_b] = eF_{ab} + T^c_{ab}(-i\nabla_c)$, justifying the analogy between the torsional field and the magnetic field.

1.1.2 Torsional chiral magnetic effect in Weyl semimetals

Now, we apply the Berry-phase formula (4.1.5) for the current correction due to the magnetic field and TMF to a model of a WSM and derive the TCME. We use the model of a pair of Weyl fermions with the opposite chirality, whose Weyl points are at $\boldsymbol{k} = \boldsymbol{\lambda}^L$ and $\boldsymbol{\lambda}^R$ in the momentum space, and Fermi energies are given by $E = v_F\lambda_0^L$ and $v_F\lambda_0^R$, respectively. Therefore the 4×4 Hamiltonian is given by

$$H(\boldsymbol{k}) := \begin{pmatrix} H_L(\boldsymbol{k}) & 0 \\ 0 & H_R(\boldsymbol{k}) \end{pmatrix} \tag{4.1.8}$$

with

$$H_s(\boldsymbol{k}) := v_F \left[\chi_s(\boldsymbol{k} - \boldsymbol{\lambda}^s) \cdot \boldsymbol{\sigma} - \lambda_0^s\right], \tag{4.1.9}$$

where $s = L$ or R is the index of the chirality and $\chi_{L(R)} = +1(-1)$, and σ^i is the Pauli matrix. The Berry energy, group velocity, and Berry curvature for the Hamiltonian are given by

$$\begin{aligned} \varepsilon^{s,\pm}(\boldsymbol{k}) &= v_F \left[\pm|\boldsymbol{k} - \boldsymbol{\lambda}^s| - \lambda_0^s\right] \\ \boldsymbol{v}^{s,\pm}(\boldsymbol{k}) &= \pm\frac{v_F(\boldsymbol{k} - \boldsymbol{\lambda}^s)}{|\boldsymbol{k} - \boldsymbol{\lambda}^s|} \\ \boldsymbol{\Omega}^{s,\pm}(\boldsymbol{k}) &= \pm\chi_s\frac{\boldsymbol{k} - \boldsymbol{\lambda}^s}{2|\boldsymbol{k} - \boldsymbol{\lambda}^s|^3}. \end{aligned} \tag{4.1.10}$$

Here $+(-)$ means the higher (lower) band of the Weyl cone.

Substituting Eq.(4.1.10) into Eq.(4.1.5), we obtain that the current density up to the first order of the magnetic field and the TMF is given by

$$\boldsymbol{j}(\boldsymbol{r}) = \left[\frac{e^2 v_F(\lambda_0^R - \lambda_0^L)}{4\pi^2}\boldsymbol{B} + \frac{e v_F(\lambda_a^R - \lambda_a^L)\Lambda}{4\pi^2}\boldsymbol{T}^a\right], \tag{4.1.11}$$

at zero temperature and up to the linear order in $\lambda_\mu^{L(R)}$, where the details of the calculations are described in Sec.4.7. Here, The vector representation of the TMF, $\boldsymbol{T}^a$, is defined by $(\boldsymbol{T}^a)_i := (1/2)\varepsilon^{ijk}T^a_{jk}$. For the derivation of Eq.(4.1.11), we introduced a momentum cutoff scheme $|\boldsymbol{k} - \boldsymbol{\lambda}^s| < \Lambda$ for the Weyl node of the chirality s. Physically, Λ corresponds to the momentum range from the Weyl points in which the cone structures of the band of the lattice system is approved.

The first term represents the CME in the presence of the chiral chemical potential (i.e. $\lambda_0^L \neq \lambda_0^R$), and then reproduces the previous result for the CME [59]. On the

other hand, the second term in Eq.(4.1.11) is a new one, which raises the TCME; i.e. the current is generated by the TMF for the pair of Weyl points which are shifted in the momentum space due to broken time-reversal symmetry. This point is in sharp contrast to the usual CME, which requires breaking inversion symmetry.

1.2 Physical interpretations

Now we discuss the consequences and physical pictures of the TCME. The TCME is realized in two types of lattice dislocations. (a) *case of edge dislocation*: $j^x \propto \Delta\lambda_z\, T_x^z$, and (b) *case of screw dislocation*: $j^z \propto \Delta\lambda_z T_z^z$, with $\Delta\lambda_a := \lambda_a^L - \lambda_a^R$. Their schematic pictures are shown in Fig.4.1. These responses can be understood with the following semiclassical picture: *Case* (a): Edge dislocation is regarded as the (0,1,0)-"surface" of the extra lattice plane made up of the blue and green atoms in Fig.4.1.a, which harbors a chiral Fermi arc, when two Weyl points are shifted in the k_z-direction. The electrons in the Fermi arc state are the very origin of the current induced by the edge dislocation. *Case* (b): There is a chiral Fermi arc mode on the dislocation line. The electrons in the mode rotate around the screw dislocation line, and due to the screw dislocation the rotating motion causes the current along the Burgers vector.

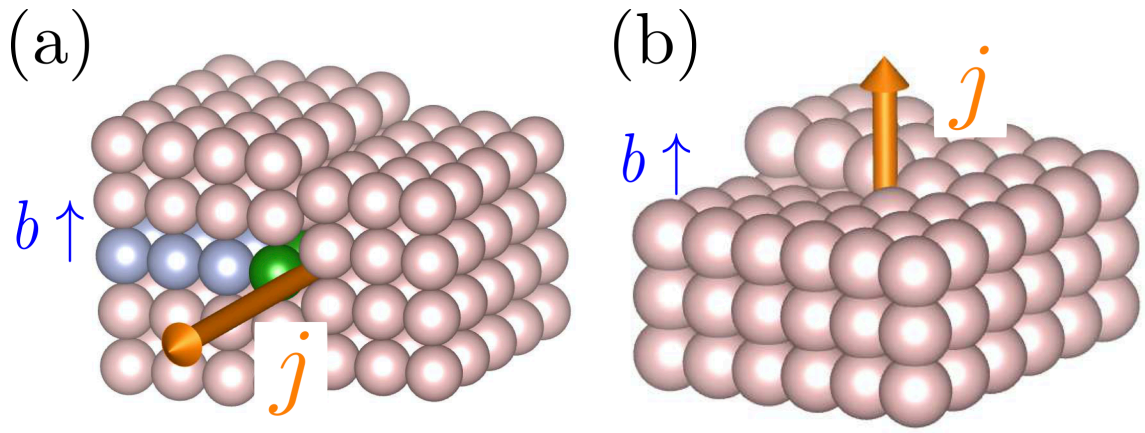

Figure 4.1: Ground state current j induced by (a) edge and (b) screw dislocation with the Burgers vector b. Reproduced form Ref.[20].

The situation is similar to that of the three-dimensional integer quantum Hall state (3DIQHS) [60] with dislocation which is the staking of quantum Hall state layers char-

acterized by the vector $\boldsymbol{G}_c = (2\pi n_c/a)\hat{n}$, where n_c, a, and $\hat{n}$ are the first Chern number, the lattice constant, and the unit vector along the staking direction. In the 3DIQHS, there are one dimensional n chiral modes along the dislocation line, when the topological number, $n = \boldsymbol{b}_g \cdot \boldsymbol{G}_c/2\pi$, is nonzero [61]. This condition for the chiral modes is similar to that for the TCME, $\boldsymbol{b}_g \cdot (\boldsymbol{\lambda}^L - \boldsymbol{\lambda}^R) \neq 0$.

2 Spectral asymmetry and ground state current in the presence of screw dislocation

In this section, we confirm the TCME due to dislocation by using an alternative approach other than the linear response theory based on Eq.(4.1.11). Our approach here is to calculate explicitly the spectrum and the eigenstates of the Weyl Hamiltonian with dislocation and the ground state current. We also show that the quasi-localized modes along the envelope of the bulk spectrum contribute to the effect. In this section, we describe the summary and the details of the calculations are described in Sec.4.8.

For simplicity, we set $v_F = e = 1$ and assume $\lambda_0^L = \lambda_0^R = 0$, and the Weyl points lie symmetrically on the k_z-axis, $\boldsymbol{\lambda}^L = -\boldsymbol{\lambda}^R = \lambda\hat{z}$. In the presence of the screw dislocation at $x = y = 0$ along z-axis, of which Burgers vector is $\boldsymbol{b}_g = -b_g\hat{z}$, the vielbeins are given by $e_{\bar{x}}^z = -b_g y/2\pi\rho^2$, $e_{\bar{y}}^z = b_g x/2\pi\rho^2$, and $e_a^\mu = \delta_a^\mu$ for others, with $\rho = \sqrt{x^2+y^2}$ [62]. Even with the dislocation, k_z remains a good quantum number. Then, when k_z is fixed, the Hamiltonian is equivalent to that of two-dimensional massive Dirac model in the presence of the magnetic flux at the origin, whose amplitude is $\Phi_{k_z} = k_z b_g$,

$$
\begin{aligned}
H_{s,k_z}^{\text{screw}} &= \chi_s \left[H_{k_z}^{\perp} + m_{k_z}^s \sigma^z \right], \\
H_{k_z}^{\perp} &= \left(-\mathrm{i}\partial_x - \frac{\Phi_{k_z} y}{2\pi\rho^2} \right) \sigma^x + \left(-\mathrm{i}\partial_y + \frac{\Phi_{k_z} x}{2\pi\rho^2} \right) \sigma^y,
\end{aligned}
\tag{4.2.1}
$$

with the mass $m_{k_z}^s = k_z - \chi_s\lambda$. The equivalence of a screw dislocation and momentum-dependent magnetic field has also been pointed out in Refs. [63, 33].

The spectrum of H_{s,k_z}^{screw} consists of two types of eigenstates: one with the eigenenergies satisfying $|E| > |m_{k_z}^s|$ and the other one with $E = \pm m_{k_z}^s$. The former does not contribute to the ground state current owing to the one-to-one correspondence between $E^+ > |m_{k_z}^s|$ and $E^- < -|m_{k_z}^s|$ modes as $E^+ = -E^-$, and between the states of Weyl nodes with the opposite chiralities. On the other hand, the latter does con-

tribute owing to asymmetry, i.e. the absence of one-to-one correspondence between $E = m^s_{k_z}$ and $E = -m^s_{k_z}$ modes. This asymmetry is called the parity anomaly [64, 42]. The asymmetric spectrum consists of discrete modes whose wavefunctions exhibit power-law decay, and continuum scattering modes which spread over the whole system [65, 66] The schematic picture of the density-of-state of the full spectrum is shown in Fig.4.2. Moreover, the ground state current calculated from the asymmetric spectrum is $J^z = -L_z b_g \Lambda\lambda/2\pi^2$, which coincides with the expression obtained directly from the linear response theory (4.1.11) as the details of the derivation is described in Sec.4.8.

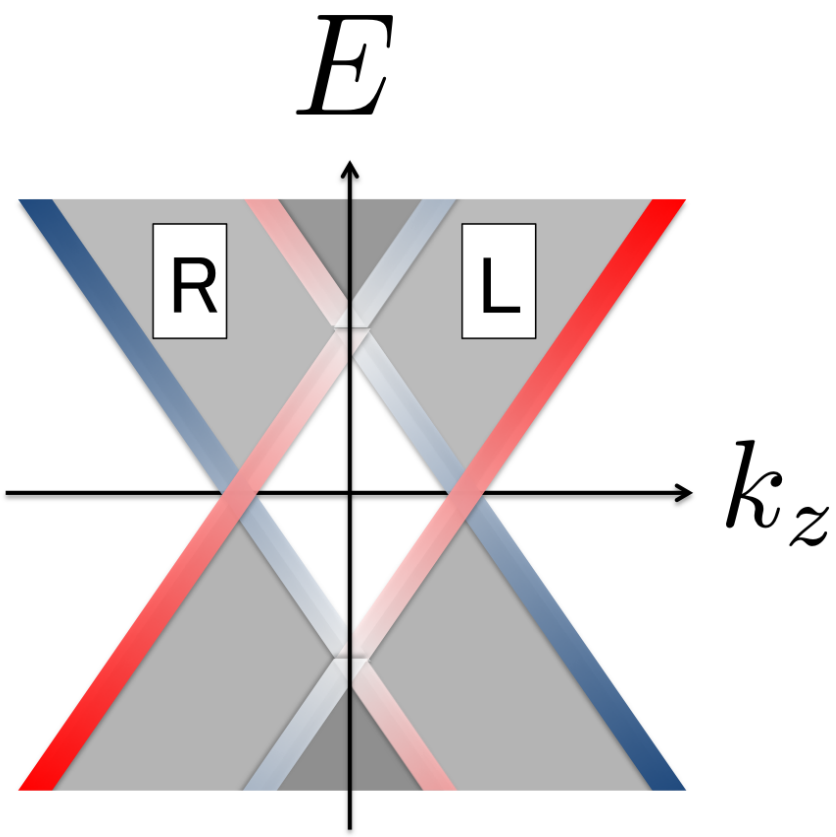

Figure 4.2: The red and blue lines along $E = \pm m^s_{k_z}$ represent the relatively higher (lower) density-of-state compared with that of the opposite energy $E = \mp m^s_{k_z}$.

3 Numerical calculation

In this section, we confirm the spectrum asymmetry and the TCME for realistic lattice models by numerical calculations. We use the tight-binding model of WSMs [16]

generalized to the case with dislocation,

$$H = \sum_{\boldsymbol{r}} \left[\mathrm{i}t \sum_{i=x,y,z} c^{\dagger}_{\boldsymbol{r}+\hat{i}+\delta_{i,z} b_g \Theta(\boldsymbol{r})} \Gamma^i c_{\boldsymbol{r}} + r \left(3 c^{\dagger}_{\boldsymbol{r}} \Gamma^4 c_{\boldsymbol{r}} - \sum_{i=x,y,z} c^{\dagger}_{\boldsymbol{r}+\hat{i}+\delta_{i,z} b_g \Theta(\boldsymbol{r})} \Gamma^4 c_{\boldsymbol{r}} \right) + \frac{d}{2} c^{\dagger}_{\boldsymbol{r}} \Gamma^{12} c_{\boldsymbol{r}} \right] + h.c., \tag{4.3.1}$$

where the 4×4-matrices, Γ^i, satisfy the $SO(5)$ Clifford algebra $\{\Gamma^i, \Gamma^j\} = 2\delta_{ij}$ [67], $\Gamma^{ij} := [\Gamma^i, \Gamma^j]/2i$, $\boldsymbol{r} = (x, y, z)$ and $\hat{i}$ denote the position of the atoms and the x^i-direction unit vector, respectively, and t, r, and d are the real parameters, and we suppose the lattice constant as 1 and lattice size $L_x \times L_y \times L_z$. We introduced a pair of screw dislocations along z-direction with opposite Burgers vector at $\pm \boldsymbol{l}^{dis} = \pm(l_x^{dis}, 0)$ as shown in Fig.4.3, by sliding the hopping directions in the first and third terms of Eq. (4.3.1) as $\Theta(\boldsymbol{r}) = -1$ for the region $x = 0$, $-l_x^{dis} < y < l_x^{dis}$, while $\Theta(\boldsymbol{r}) = 0$ for other regions.

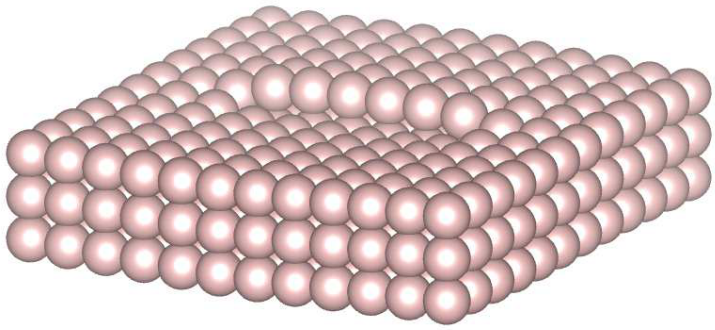

Figure 4.3: Setup for the numerical calculation: lattice with a pair of screw dislocations with opposite Burgers vectors. Reproduced from Ref.[20].

Now, we numerically diagonalized this model and obtained the spectrums and current. Here the material parameters are set as $t = r = 1$ and $d = 3.6$. The lattice constant is 1 and the amplitudes of the Burgers vectors is set as $b_g = 1$. For the calculation, we imposed the open boundary condition along the $x-$ and $y-$directions and periodic boundary condition along the $z-$direction, and set $L_x = L_y = 4l_x^{dis} = 38$ and $L_z = 100$.

As shown in Fig.4.4.a-c, we obtained the asymmetric spectrum in agreement with the analytic calculation. The asymmetric modes are localized at the dislocation line.

The quasi-localized chiral modes are not isolated from the bulk but easily mixed with the bulk modes (Fig.4.4.a-c).

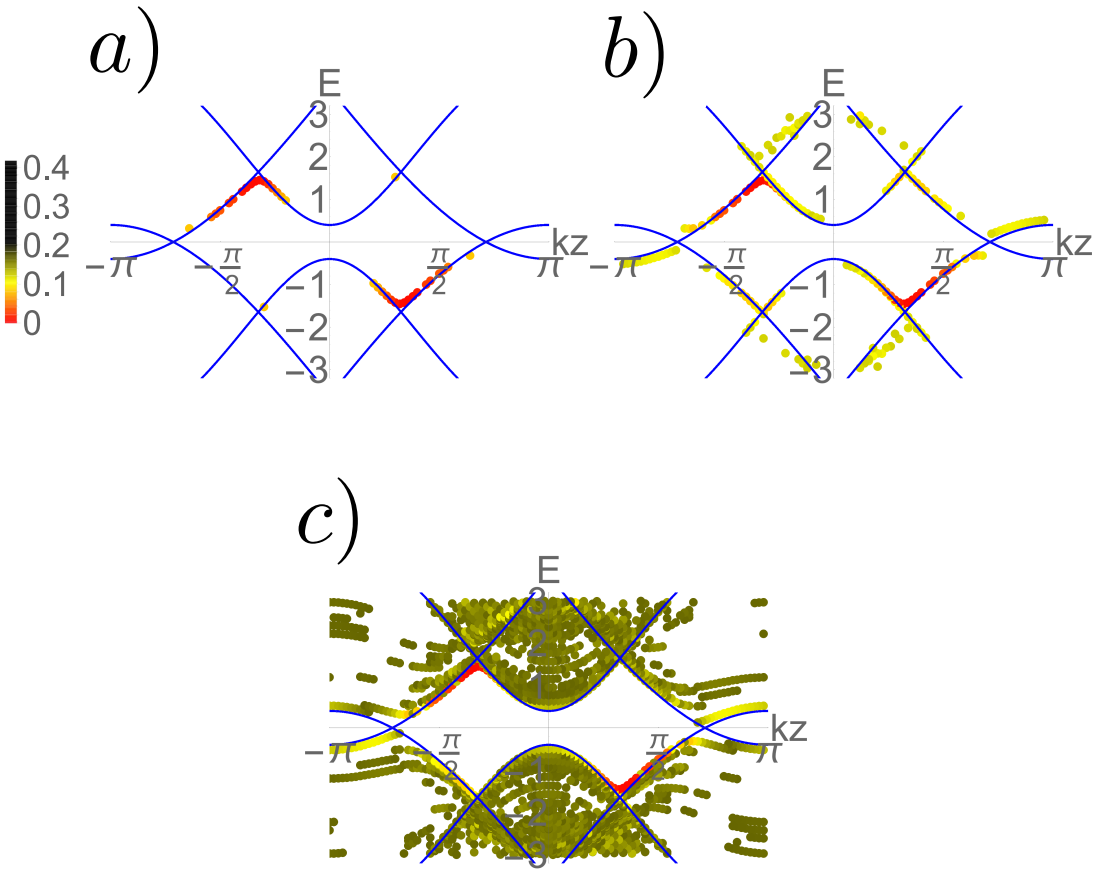

Figure 4.4: Numerical result for the spectrum of the WSMs with a pair of screw dislocations. The blue curves are the envelope of the bulk spectrum. The colors represent the expectation value of $|\boldsymbol{\rho}-\boldsymbol{l}^{dis}|^2/L_xL_y$ (see the color scale bar). In the figures (a,b,c), the modes with this value smaller than 0.1, 0.15, and 0.2 are plotted. Reproduced from [20].

We also show the current density at zero temperature in Fig.4.5. We obtained the upward current along the screw dislocation and downward current along the anti-screw dislocation due to the TCME. The total current per the unit length toward z-direction due to one dislocation line is $J^z/L_z = 0.087$, which is calculated by the summation of the current density in the $x > 0$ half-plane, and this value is in the same order as that estimated from the linear response theory (4.1.11), $J^z/L_z \sim 0.1$. For the estimation,

we set the cutoff as $\Lambda \sim 1/(\text{lattice constant}) = 1$.

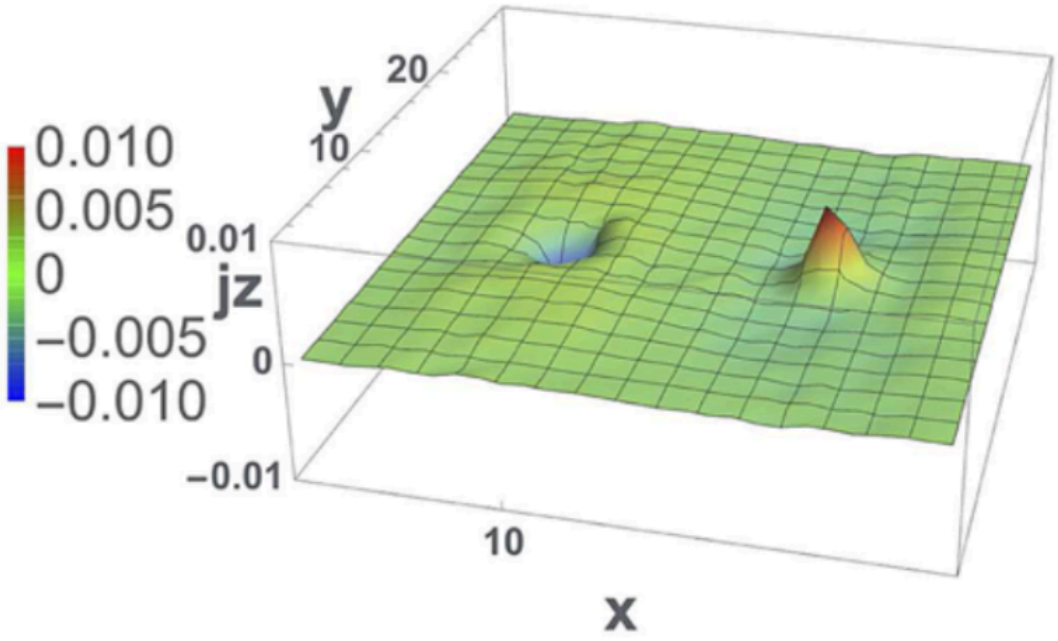

Figure 4.5: Current density along z-direction, $j_z(x, y)$. Reproduced from Ref.[20].

4 Comment on no-go theorem of the chiral magnetic effect

The existence of the TCME in the realistic lattice system may seem to contradict with the no-go theorems of the ground state current [16, 17]. However, they prohibit the *total* current, but not the *local* current density. Therefore, the current along the dislocation line can exist. In the following sentences in this section, we show this point from an argument that is the extension of that presented in Ref. [16].

We start with a general Hamiltonian of electrons in solids (set $e = 1$ in this section):

$$H = \int d^3\boldsymbol{r}\ \frac{1}{2m}\left(-\mathrm{i}\nabla_i - A_i(\boldsymbol{\rho}, z)\right)^2 + V(\boldsymbol{\rho}, z), \tag{4.4.1}$$

where V is the potential term, in which the effect of the dislocation is included. Here $i = x, y, z$, $\boldsymbol{r} = (\boldsymbol{\rho}, z)$, and $\boldsymbol{\rho} = (x, y)$, and we impose the periodicity in the z-direction:

$$A_i(\boldsymbol{\rho}, z) = A_i(\boldsymbol{\rho}, z + a), V(\boldsymbol{\rho}, z) = V(\boldsymbol{\rho}, z + a). \tag{4.4.2}$$

Suppose ψ is one eigenfunction of the Hamiltonian and define the Bloch wave function $\psi_{n,k_z}(\boldsymbol{\rho}, z) = e^{\mathrm{i}k_z z} u_{n,k_z}(\boldsymbol{\rho}, z)$, whose energy is ε_{n,k_z}. The total current along the z-direction is given by

$$\begin{aligned} J_z =& \sum_n \int_{BZ} \frac{dk_z}{2\pi} \int d^3\boldsymbol{r}\ \psi^*_{n,k_z}(\boldsymbol{\rho}, z) \frac{\delta H}{\delta A_z} \psi_{n,k_z}(\boldsymbol{\rho}, z) n_F(\varepsilon_{n.k_z}) \\ =& -\sum_n \int_{BZ} \frac{dk_z}{2\pi} \int d^3\boldsymbol{r}\ u^*_{n,k_z}(\boldsymbol{\rho}, z) \frac{\partial H_{k_z}}{\partial k_z} u_{n,k_z}(\boldsymbol{\rho}, z) n_F(\varepsilon_{n.k_z}), \end{aligned} \tag{4.4.3}$$

where $H_{k_z} = e^{-ik_z z} H e^{ik_z z}$ and n_F is the Fermi distribution function. Here we use the identity :

$$\begin{aligned} & \int d^3\boldsymbol{r}\ u^*_{n,k_z}(\boldsymbol{\rho}, z) \frac{\partial H_{k_z}}{\partial k_z} u_{n,k_z}(\boldsymbol{\rho}, z) \\ &= \frac{\partial}{\partial k_z} \int d^3\boldsymbol{r}\ u^*_{n,k_z}(\boldsymbol{\rho}, z) H_{k_z} u_{n,k_z}(\boldsymbol{\rho}, z) \\ &= \frac{\partial \varepsilon_{n,k_z}}{\partial k_z}, \end{aligned} \tag{4.4.4}$$

which follows from

$$\frac{\partial}{\partial k_z} \left[\int d^3r\ u^*_{n,k_z}(\boldsymbol{\rho}, z) u_{n,k_z}(\boldsymbol{\rho}, z) \right] = \frac{\partial}{\partial k_z} 1 = 0, \tag{4.4.5}$$

and then we can rewrite Eq. (4.4.3) into

$$\begin{aligned} J_z &= -\sum_n \int_{BZ} \frac{dk_z}{2\pi} \frac{\partial \varepsilon_{n,k_z}}{\partial k_z} n_F(\varepsilon_{n.k_z}) \\ &= -\frac{1}{2\pi} \sum_n \sum_{i=1,\ldots,i^{(n)}} \int_{\varepsilon_{n,k^{(n)}_{i-1}}}^{\varepsilon_{n,k^{(n)}_i}} d\varepsilon\ n_F(\varepsilon) \end{aligned} \tag{4.4.6}$$

Here for each region $k \in (k^{(n)}_{i-1}, k^{(n)}_i)$, $\varepsilon_{n,k}$ monotonically increases or decreases, and $k^{(n)}_0 = 0$ and $k^{(n)}_{i^{(n)}} = 2\pi/a$. We find that Eq.(4.4.6) is always equal to zero owing to the periodicity of the dispersion in the wave number space, $\varepsilon_{n,k=0} = \varepsilon_{n,k=2\pi/a}$. Therefore, we found that the *total* current along the z-direction is zero. In the above derivation, it is essential that the integrand with respect to k_z can be rewritten into the total

derivative with respect to k_z, and this key factor follows from the fact that the integral over the real space of $|u_{n,k_z}(\boldsymbol{\rho}, z)|^2$ is equal to 1, which results in Eq. (4.4.5). Instead, without the integration over the real space,

$$\frac{\partial}{\partial k_z}\left[u^*_{n,k_z}(\boldsymbol{\rho}, z)u_{n,k_z}(\boldsymbol{\rho}, z)\right] \neq 0. \tag{4.4.7}$$

Then, in the case of *local* current, the above argument in the case of the *total* current does not hold. Hence, the local current is not always zero, unlike the total current. Therefore, the TCME occurs as the generation of a local current along and near a dislocation line.

5 Experimental implications

In this section, we present two experimental setups to observe the TCME, for which $Eu_2Ir_2O_7$ [68] and $YbMnBi_2$[69] are candidate materials: a SQUID measurement and nonlocal transport phenomenon. We also comment on effects of impurities and disorientation of the dislocation.

5.1 SQUID measurement

The first one is a scanning SQUID measurement, which can detect weak inhomogeneous magnetic fields [70, 71] (Fig.4.6). If there is a pair of dislocations, the circulating current occurs. The magnitudes of the current and the induced magnetic field are estimated as $I \sim 10^{-5}$A and $B \sim 10^{-7}$T, respectively, for both $Eu_2Ir_2O_7$ and $YbMnBi_2$. Here we used Eq.(4.1.11) and the material parameters, $v_F \sim 10^5 m/s$ and $a \sim 10$Å and set $b_g = a$ and $\lambda \sim \Lambda \sim 1/a$, where a is the lattice constant. Also, for the estimation of the magnitude of the magnetic field, we used a typical value of inter-distance between dislocations, 10^5Å [72]. It is feasible to detect $B \sim 10^{-7}$T via the scanning SQUID.

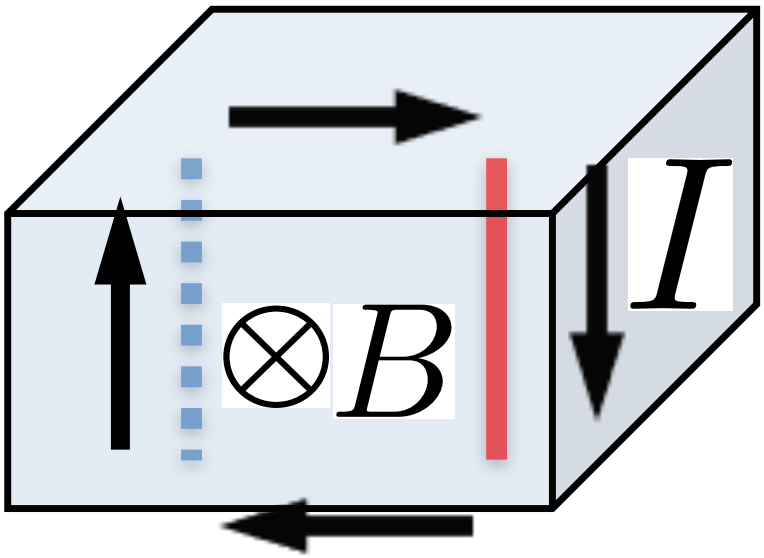

Figure 4.6: The current (shown as arrows and I) due to the TCME in the presence of a pair of dislocation lines. The thick red solid (blue dashed) line represents the (anti-)dislocation line. We can detect the magnetic field, B, via a scanning SQUID measurement.

5.2 Nonlocal transport phenomenon

The second one is a nonlocal transport phenomenon, which was observed in quantum Hall materials [73, 74]. The experimental setup is shown in Fig.4.7. If the bulk contributions are completely negligible and there are only the chiral modes at the dislocation lines, $V_{34} := V_3 - V_4 = 0$ despite $I_{12} \neq 0$, then, the nonlocal resistivity $R_{12,34} := V_{34}/I_{12}$ is equal to zero [73]. On the other hand, if the nonlocal transport is negligible, $V_{34} > V_{3'4'}$ holds for $L_1 L_3 < L_1 L_{3'}$ when $I_{12} \neq 0$. Therefore, if $R_{12,34} < R_{12,3'4'}$ is observed, it is the fingerprint of the chiral current due to the TCME. The effect can be discriminated from any previously reported conventional transport induced by dislocation [75, 76, 77, 72, 78, 79, 80, 81, 82, 83].

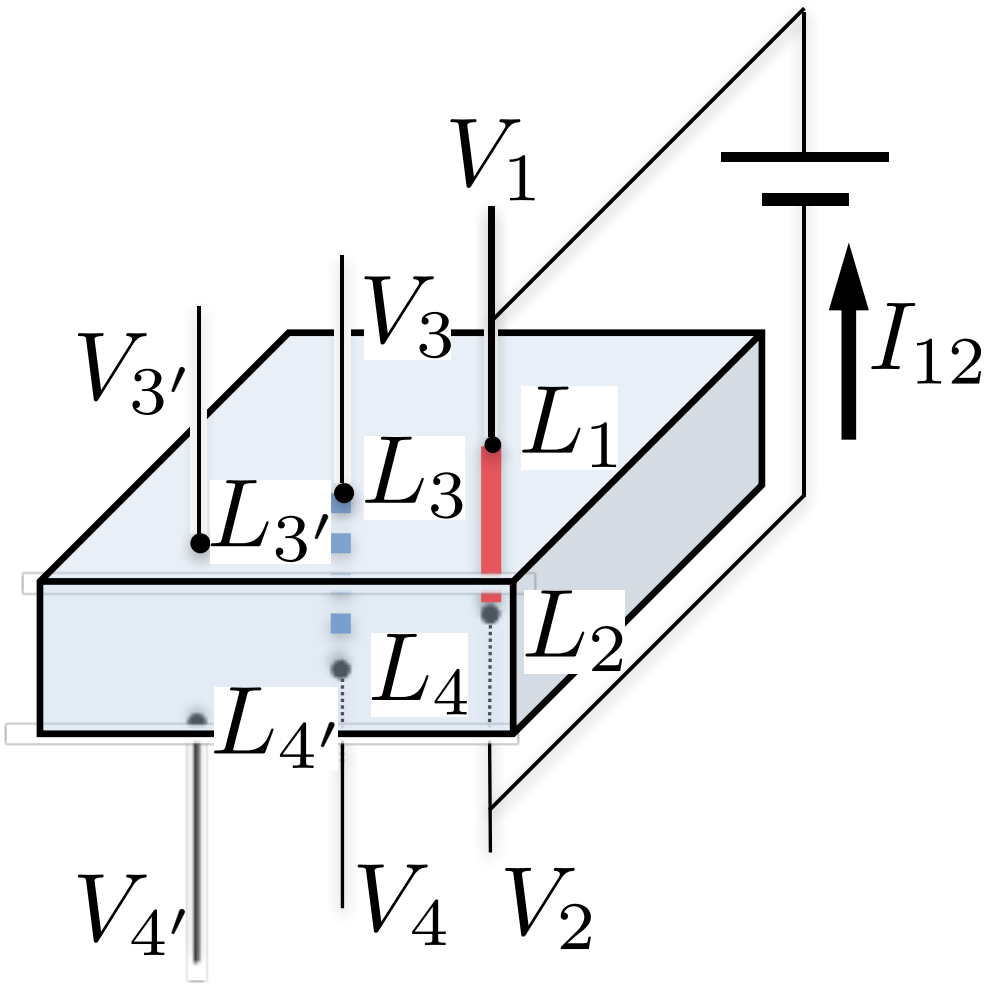

Figure 4.7: Experimental setup for the nonlocal transport due to the TCME. The thick red solid (blue dashed) line represents the (anti-)dislocation line. The leads are attached at the black points, $L_i (i = 1, 2, 3, 4, 3', 4')$. The line L_1L_2, L_3L_4, and $L_{3'}L_{4'}$ are parallel and have the same length. Here we suppose $L_1L_3 < L_1L_{3'}$. V_i is the voltage at L_i, and I_{12} is the current. Reproduced from Ref.[20].

5.3 Comment on impurity and disorientation effects

We also comment on effects of impurities and disorientation of the dislocation. First, the current due to the TCME is expected to be robust against weak disorder. It is because that Eq.(4.1.11) is independent of the scattering time, like the intrinsic contribution to the anomalous Hall effect [41]. More precisely, the current is due to the edge modes

in the Fermi arc on the surface of WSMs, and these modes are supported by the Weyl points, which are protected by the Chern number, and hence, robust againt weak disorder.

Next, in real experimental setups, it is difficult to align the dislocation line orthogonal (parallel) to the line connecting the Weyl nodes exactly in the case (a) (case (b)). Even when they are not orthogonal (parallel), as long as they are not parallel (orthogonal), the current parallel to the dislocation line still exists. Supposing that the dislocation line is parallel to the z-axis, the current is given by $J^z = ev_F L_z \Lambda(\boldsymbol{\lambda}^R - \boldsymbol{\lambda}^L) \cdot \boldsymbol{b}_g / 4\pi^2$ in the both cases (a) and (b).

6 Summary

In this chapter, we have discussed the TCME in WSMs caused by dislocation using the formalism of the differential geometry described in Chapter 2. We have also confirmed that this effect can occur and is experimentally observable in realistic materials, from the calculation of the ground state in the presence of dislocations and the numerical calculation of the tight-binding model. Furthermore, we have proposed the experimental setups to observe it.

7 Appendix: Derivation of torsional responses from linear response theory

In this section, we derive the Berry-phase formulae for the correction to the charge and current densities due to TMFs and magnetic fields (4.1.4) and (4.1.5), and the torsional chiral magnetic effect in WSMs (4.1.11).

The derivation consists of two steps: first we derive the expression for the Green function in the presence of the gauge field and vielbein using the gradient expansion (4.7.4), and next we calculate the current density by using Eq.(4.7.4) and obtain Eq.(4.7.21), which is equivalent to Eq.(4.1.11).

First, we calculate the single-electron Green function. The Green function in the

presence of the gauge field and vielbein which is defined by

$$
\begin{aligned}
&G(\tau_1, \boldsymbol{r}_1, \tau_2, \boldsymbol{r}_2) \\
&:= \frac{\int \mathcal{D}\psi \mathcal{D}\psi^\dagger \psi(\tau_1, \boldsymbol{r}_1)\psi^\dagger(\tau_2, \boldsymbol{r}_2) \exp\left(-S[\psi, \psi^\dagger, A_i, e_i^a]\right)}{\int \mathcal{D}\psi \mathcal{D}\psi^\dagger \exp\left(-S[\psi, \psi^\dagger, A_i, e_i^a]\right)}.
\end{aligned} \tag{4.7.1}
$$

Then, the following differential equation holds :

$$
\begin{aligned}
&\frac{1}{2}\Big[\hat{\mathcal{L}}(\varepsilon_N, \boldsymbol{r}_1, -\mathrm{i}\partial_{\boldsymbol{r}_1}) G(\varepsilon_N, \boldsymbol{r}_1, \boldsymbol{r}_2) \\
&+ G(\varepsilon_N, \boldsymbol{r}_1, \boldsymbol{r}_2) \overleftarrow{\hat{\mathcal{L}}}^*(-\varepsilon_N, \boldsymbol{r}_2, -\mathrm{i}\partial_{\boldsymbol{r}_2})\Big] = \delta^{(3)}(\boldsymbol{r}_1 - \boldsymbol{r}_2),
\end{aligned} \tag{4.7.2}
$$

with $\hat{\mathcal{L}}(\varepsilon_N, \boldsymbol{r}, -\mathrm{i}\partial_{\boldsymbol{r}}) := |e(\boldsymbol{r})|[\mathrm{i}\varepsilon_N - H(-\mathrm{i}\nabla_a)] - eA_0]$, and $|e(\boldsymbol{r})| := \det e_i^a(\boldsymbol{r})$ Here $\varepsilon_N = (2N+1)\pi T$ is the Fermionic Matsubara frequency with the temperature T, and $G(\varepsilon_N, \boldsymbol{r}_1, \boldsymbol{r}_2) := \int_0^\beta G(\tau, \boldsymbol{r}_1, 0, \boldsymbol{r}_2) e^{-\mathrm{i}\varepsilon_N \tau} d\tau$ is the Fourier component of the Green function. Now, using the spatial Wigner transformation defined as $\tilde{f}(\boldsymbol{R}, \boldsymbol{p}) := \int d^3\boldsymbol{r} e^{-\mathrm{i}\boldsymbol{r}\cdot\boldsymbol{p}} f(\boldsymbol{R} + \boldsymbol{r}/2, \boldsymbol{R} - \boldsymbol{r}/2)$, Eq. (4.7.2) is rewritten into

$$
\begin{aligned}
&\frac{1}{2}\Big[\hat{\mathcal{L}}(\varepsilon_N, \boldsymbol{R}, \boldsymbol{p}) e^{\frac{\mathrm{i}}{2}(\overleftarrow{\partial_{\boldsymbol{R}}}\overrightarrow{\partial_{\boldsymbol{p}}} - \overleftarrow{\partial_{\boldsymbol{p}}}\overrightarrow{\partial_{\boldsymbol{R}}})} \tilde{G}(\varepsilon_N, \boldsymbol{R}, \boldsymbol{p}) \\
&+ \tilde{G}(\varepsilon_N, \boldsymbol{R}, \boldsymbol{p}) e^{\frac{\mathrm{i}}{2}(\overleftarrow{\partial_{\boldsymbol{R}}}\overrightarrow{\partial_{\boldsymbol{p}}} - \overleftarrow{\partial_{\boldsymbol{p}}}\overrightarrow{\partial_{\boldsymbol{R}}})} \hat{\mathcal{L}}(\varepsilon_N, \boldsymbol{R}, \boldsymbol{p})\Big] = 1.
\end{aligned} \tag{4.7.3}
$$

In the gradient expansion up to the first order in $\partial_i A_j$ or $\partial_i e_j^a$, the Green function becomes

$$
\begin{aligned}
&\tilde{G}(\varepsilon_N, \boldsymbol{R}, \boldsymbol{p}) = \tilde{G}^{(0)}(\varepsilon_N, \boldsymbol{R}, \boldsymbol{p}) + \tilde{G}^{(1)}(\varepsilon_N, \boldsymbol{R}, \boldsymbol{p}) + \cdots, \\
&\tilde{G}^{(0)}(\varepsilon_N, \boldsymbol{R}, \boldsymbol{p}) = \frac{1}{|e(\boldsymbol{R})|} \left[\mathcal{L}_0(\varepsilon_N, \boldsymbol{\pi})\right]^{-1}_{\pi_a = e_a^i(\boldsymbol{R})(p_i - eA_i(\boldsymbol{R}))}, \\
&\tilde{G}^{(1)}(\varepsilon_N, \boldsymbol{R}, \boldsymbol{p}) \\
&= \frac{\mathrm{i}}{2|e(\boldsymbol{R})|} \mathcal{L}_0^{-1}(\varepsilon_N, \boldsymbol{\pi}) \frac{\partial \mathcal{L}_0(\varepsilon_N, \boldsymbol{\pi})}{\partial \pi_a} \mathcal{L}_0^{-1}(\varepsilon_N, \boldsymbol{\pi}) \frac{\partial \mathcal{L}_0(\varepsilon_N, \boldsymbol{\pi})}{\partial \pi_b} \\
&\cdot \mathcal{L}_0^{-1}(\varepsilon_N, \boldsymbol{\pi}) \left[eF_{ab}(\boldsymbol{R}) + T_{ab}^c(\boldsymbol{R})\pi_c\right]\Big|_{\pi_a = e_a^i(\boldsymbol{R})(p_i - eA_i(\boldsymbol{R}))}.
\end{aligned} \tag{4.7.4}
$$

Here $\pi_a := e_a^i(\boldsymbol{R})(p_i - eA_i(\boldsymbol{R}))$ is the gauge-invariant mechanical momentum, while p_i is the canonical momentum, and the field strength and the torsion with the indices of the local orthogonal coordinate are, respectively, defined as $F_{ab} := e_a^i e_b^j F_{ij}$ and $T_{ab}^c := e_a^i e_b^j T_{ij}^c$. The free Lagrangian is defined as $\mathcal{L}_0(\varepsilon_N, \boldsymbol{\pi}) := \mathrm{i}\varepsilon_N - H(\boldsymbol{\pi})$.

Next, using Eq. (4.7.4), we calculate the current density and derive Eq.(4.1.5). The current density are defined by $j^a(\boldsymbol{r}) := -(e_i^a(\boldsymbol{r}))/|e(\boldsymbol{r}))|)(\delta S_{\rm eff}/\delta A_i(\boldsymbol{r}))$. Therefore

$$
\begin{aligned}
&j^{\bar{1}}(\boldsymbol{R}) \\
&= \frac{e_i^{\bar{1}}}{|e(\boldsymbol{R})|} \left. \frac{\int \mathcal{D}\psi\mathcal{D}\psi^\dagger \psi^\dagger(\tau,\boldsymbol{r}_1)\frac{1}{2}\frac{\delta\hat{\mathcal{L}}}{\delta A_i}\psi(\tau,\boldsymbol{r}_2)e^{-S}}{\int \mathcal{D}\psi\mathcal{D}\psi^\dagger e^{-S}} \right|_{\boldsymbol{r}_1,\boldsymbol{r}_2\to\boldsymbol{R},} + c.c. \\
&= \frac{eT}{2}\sum_N \mathrm{Tr}\left[\left. \frac{\partial \mathcal{L}_0(\epsilon_N,\boldsymbol{\pi})}{\partial \pi_{\bar{1}}} \right|_{\pi_a = e_a^i(\boldsymbol{r}_2)(-\mathrm{i}\partial_{r_2^i} - eA_i(\boldsymbol{r}_2))} \right. \\
&\left. G(\varepsilon_N,\boldsymbol{r}_2,\boldsymbol{r}_1)]\right|_{\boldsymbol{r}_1,\boldsymbol{r}_2\to\boldsymbol{R}} + c.c. \\
&= \frac{eT}{2}\sum_N \int \frac{d^3p}{(2\pi)^3}\mathrm{Tr}\left[\left. \frac{\partial \mathcal{L}_0(\epsilon_N,\boldsymbol{\pi})}{\partial \pi_{\bar{1}}} \right|_{\pi_a = e_a^i(\boldsymbol{R})(p_i - eA_i(\boldsymbol{R}))} \right. \\
&\left. e^{\frac{\mathrm{i}}{2}(\overleftarrow{\partial_{\boldsymbol{R}}}\overrightarrow{\partial_{\boldsymbol{p}}} - \overleftarrow{\partial_{\boldsymbol{p}}}\overrightarrow{\partial_{\boldsymbol{R}}})}\tilde{G}(\varepsilon_N,\boldsymbol{R},\boldsymbol{p})\right] + c.c.
\end{aligned}
\tag{4.7.5}
$$

Here Tr means the trace over the band indices, we used that $\delta\hat{\mathcal{L}}/\delta A_i = e|e(\boldsymbol{r})|e_a^i(\boldsymbol{r})\partial L_0/\partial\pi_a$ and the second line does not depend on τ due to imaginary time-translation symmetry. Note that $\boldsymbol{\pi}$ of the third line is the operator though that of the fourth one is the c-number. Using Eq.(4.7.4), up to the first order in $\partial_i A_j$ or $\partial_i e_j^a$, the expression of the current density becomes

$$
j^{\bar{1}}(\boldsymbol{R}) = j^{\bar{1}(0)}(\boldsymbol{R}) + j^{\bar{1}(1)}(\boldsymbol{R}),
\tag{4.7.6}
$$

with the zeroth-order terms,

$$
\begin{aligned}
&j^{\bar{1}(0)}(\boldsymbol{R}) \\
&= \frac{eT}{2}\sum_N \int \frac{d^3p}{(2\pi)^3}\mathrm{Tr}\left[\left. \frac{\partial \mathcal{L}_0(\epsilon_N,\boldsymbol{\pi})}{\partial \pi_{\bar{1}}} \right|_{\pi_a = e_a^i(\boldsymbol{R})(p_i - eA_i(\boldsymbol{R}))} \right. \\
&\left. \tilde{G}^{(0)}(\varepsilon_N,\boldsymbol{R},\boldsymbol{p})\right] + c.c.
\end{aligned}
\tag{4.7.7}
$$

and the first-order terms,

$$
\begin{aligned}
& j^{\bar{1}(1)}(\boldsymbol{R}) \\
& = \frac{eT}{2}\sum_N \int \frac{d^3p}{(2\pi)^3}\mathrm{Tr}\left[\left.\frac{\partial \mathcal{L}_0(\epsilon_N,\boldsymbol{\pi})}{\partial \pi_{\bar{1}}}\right|_{\pi_a=e_a^i(\boldsymbol{R})(p_i-eA_i(\boldsymbol{R}))}\right. \\
& \left.\tilde{G}^{(1)}(\varepsilon_N,\boldsymbol{R},\boldsymbol{p})\right] \\
& + \frac{\mathrm{i}eT}{4}\sum_N \mathrm{Tr}\left[\left.\frac{\partial \mathcal{L}_0(\epsilon_N,\boldsymbol{\pi})}{\partial \pi_{\bar{1}}}\right|_{\pi_a=e_a^i(\boldsymbol{R})(p_i-eA_i(\boldsymbol{R}))}\right. \\
& \left.(\overleftarrow{\partial_{\boldsymbol{R}}}\overrightarrow{\partial_{\boldsymbol{p}}} - \overleftarrow{\partial_{\boldsymbol{p}}}\overrightarrow{\partial_{\boldsymbol{R}}})\tilde{G}^{(0)}(\varepsilon_N,\boldsymbol{R},\boldsymbol{p})\right] + c.c.. \qquad (4.7.8)
\end{aligned}
$$

The zeroth-order terms (4.7.7) can be rewritten as

$$
j^{\bar{1}(0)}(\boldsymbol{R}) = e\sum_n \int \frac{d^3\pi}{(2\pi)^3} v^{n,\bar{1}}(\boldsymbol{\pi}) n_F(\varepsilon_{n,\boldsymbol{\pi}}). \qquad (4.7.9)
$$

For the derivation, we inserted the identity, $1_{\boldsymbol{\pi}} = \sum_n |u^n_{\boldsymbol{\pi}}\rangle \langle u^n_{\boldsymbol{\pi}}|$, between $\partial\mathcal{L}_0/\partial\pi_{\bar{1}}$ and $\tilde{G}^{(0)}$ in Eq.(4.7.7), and used the formula, $\sum_{N=-\infty}^{\infty}[1/(\mathrm{i}\varepsilon_N - t) + 1/(-\mathrm{i}\varepsilon_N - t)] = (1 - 2n_F(t))/T$, for the summation over the Matsubara frequency, and $\int d^3p = |e(\boldsymbol{R})|\int d^3\pi$. Here, n is the band index, $\varepsilon_{n,\boldsymbol{\pi}}$ is the energy, $v^{n,a}(\boldsymbol{\pi}) := \partial\varepsilon_{n,\boldsymbol{\pi}}/\partial\pi_a$ is the group velocity, $n_F(\varepsilon) := 1/(e^{\varepsilon/T}+1)$ is the Fermi distribution function, and $|u^n_{\boldsymbol{\pi}}\rangle$ is the Bloch state. This term corresponds to the summation of all contributions to the current from the electrons in the occupied states in the absence of magnetic and torsional magnetic field.

Now, we move on the calculation of Eq.(4.7.8). The sum of the second term of Eq.(4.7.8) and its complex conjugate is zero, since $[\cdots]^* = [\cdots]|_{\varepsilon_N\to-\varepsilon_N}$. Then, by using Eq.(4.7.4), we obtain

$$
\begin{aligned}
& j^{\bar{1}(1)}(\boldsymbol{R}) \\
& = \frac{\mathrm{i}eT}{4}\sum_N \int \frac{d^3\pi}{(2\pi)^3}\mathrm{Tr}\left[\frac{\partial \mathcal{L}_0(\varepsilon_N,\boldsymbol{\pi})}{\partial \pi_{\bar{1}}}\mathcal{L}_0^{-1}(\varepsilon_N,\boldsymbol{\pi})\frac{\partial \mathcal{L}_0(\varepsilon_N,\boldsymbol{\pi})}{\partial \pi_a}\right. \\
& \left.\mathcal{L}_0^{-1}(\varepsilon_N,\boldsymbol{\pi})\frac{\partial \mathcal{L}_0(\varepsilon_N,\boldsymbol{\pi})}{\partial \pi_b}\mathcal{L}_0^{-1}(\varepsilon_N,\boldsymbol{\pi})\right][eF_{ab}(\boldsymbol{R}) + T^c_{ab}(\boldsymbol{R})\pi_c] \\
& + c.c.. \qquad (4.7.10)
\end{aligned}
$$

Moreover, inserting the identities, $1_{\boldsymbol{\pi}} = \sum_n |u^n_{\boldsymbol{\pi}}\rangle \langle u^n_{\boldsymbol{\pi}}|$, we obtain

$$
\begin{aligned}
&j^{\bar{\mathrm{l}}(1)}(\boldsymbol{R}) \\
&= \frac{-\mathrm{i}eT}{4} \sum_{N,n,m,l} \int \frac{d^3\pi}{(2\pi)^3} \left\langle n \left| \frac{\partial H}{\partial \pi_{\bar{\mathrm{l}}}} \right| m \right\rangle \left\langle m \left| \frac{\partial H}{\partial \pi_a} \right| l \right\rangle \\
&\times \left\langle l \left| \frac{\partial H}{\partial \pi_b} \right| n \right\rangle \frac{1}{(\mathrm{i}\varepsilon_N - \varepsilon_n)(\mathrm{i}\varepsilon_N - \varepsilon_m)(\mathrm{i}\varepsilon_N - \varepsilon_l)} \\
&\times [eF_{ab}(\boldsymbol{R}) + T^c_{ab}(\boldsymbol{R})\pi_c] + c.c.,
\end{aligned} \tag{4.7.11}
$$

where the indices $\boldsymbol{\pi}$ are omitted like $\varepsilon_n := \varepsilon_{n,\boldsymbol{\pi}}$ and $|n\rangle := |u^n_{\boldsymbol{\pi}}\rangle$. There are three types of contributions to the summation over the band indices n, m, l: (a) all the three are the same, (b) two of them are the same and the other is different, and (c) each one is different respectively. However the contribution (a) is found to be zero because of the antisymmetry of $[eF_{ab}(\boldsymbol{R}) + T^c_{ab}(\boldsymbol{R})\pi_c]$ under $a \leftrightarrow b$. Moreover, the contribution (c) is also zero, since our model of the WSM, Eq.(4.1.8), consists of two two-band Hamiltonians independent of each other, and then the overlap of three or more bands is zero. Therefore, we have only to consider the contribution (b), and then obtain

$$
\begin{aligned}
&j^{\bar{\mathrm{l}}(1)}(\boldsymbol{R}) \\
&= \frac{-\mathrm{i}e}{4} \sum_n \int \frac{d^3\pi}{(2\pi)^3} \left[eF_{ab} + T^c_{ab}\pi_c\right] \left(M_{\bar{\mathrm{l}}ab} + M_{ab\bar{\mathrm{l}}} + M_{b\bar{\mathrm{l}}a}\right) \\
&+ c.c.,
\end{aligned} \tag{4.7.12}
$$

with

$$
\begin{aligned}
M_{abc} &:= v^n_a n'_F(\varepsilon_n) \langle n, b \,|\, (\varepsilon_n - H) \,|\, n, c\rangle \\
&\quad + v^n_a \langle n, b \,|\, n_F(H) \,|\, n, c\rangle - v^n_a n_F(\varepsilon_n) \langle n, b \,|\, n, c\rangle ,
\end{aligned} \tag{4.7.13}
$$

where we used the abridged notation, $|n, a\rangle := \left|\frac{\partial u^n_{\boldsymbol{\pi}}}{\partial \pi_a}\right\rangle$. For the derivation of Eqs.(4.7.12) and (4.7.13) we used the formulae

$$
\sum_{N=-\infty}^{\infty} \frac{1}{(\mathrm{i}\varepsilon_N - t)^2(\mathrm{i}\varepsilon_N - s)} = \frac{tn'_F(s) - sn'_F(t) + n_F(s) - n_F(t)}{T(t-s)^2}, \tag{4.7.14}
$$

$$
\left\langle n \left| \frac{\partial H}{\partial \pi_a} \right| m \right\rangle = (\varepsilon^m - \varepsilon^n) \langle n \,|\, m, a\rangle , \tag{4.7.15}
$$

for $n \neq m$, and

$$\sum_m f(\varepsilon_m) \langle n, b \,|\, n, c \rangle = \langle n, b \,|\, f(H) \,|\, n, c \rangle \tag{4.7.16}$$

for any function f. Moreover, using the relationship $(M_{abc})^* = M_{acb}$, we obtain

$$\begin{aligned} & j^{\bar{1}(1)}(\boldsymbol{R}) \\ & = \frac{-\mathrm{i}eT}{2} \sum_n \int \frac{d^3\pi}{(2\pi)^3} \left[eF_{\bar{2}\bar{3}} + T^d_{\bar{2}\bar{3}} \pi_d \right] \varepsilon^{abc} M_{abc}, \end{aligned} \tag{4.7.17}$$

where ε^{abc} is the antisymmetric symbol. Furthermore, since $v^n_a n'_F(\varepsilon_n) = \partial n_F(\varepsilon_n)/\partial \pi_a$ and only antisymmetric parts of M_{abc} contribute, using integration by parts, we find

$$\begin{aligned} & j^{\bar{1}(1)}(\boldsymbol{R}) \\ & = \mathrm{i}e \sum_n \int \frac{d^3\pi}{(2\pi)^3} \left[eF_{\bar{2}\bar{3}} + T^d_{\bar{2}\bar{3}} \pi_d \right] \varepsilon^{abc} v^n_a n_F(\varepsilon_n) \langle n, b \,|\, n, c \rangle \\ & + \frac{\mathrm{i}e}{2} \sum_n \int \frac{d^3\pi}{(2\pi)^3} T^a_{\bar{2}\bar{3}} \varepsilon^{abc} \varepsilon_n n_F(\varepsilon_n) \langle n, b \,|\, n, c \rangle . \end{aligned} \tag{4.7.18}$$

Using the Berry curvature is defined by $\Omega^n_a := -\mathrm{i}\varepsilon^{abc} \langle n, b | n, c \rangle$, and the vector representation of the TMF, $\boldsymbol{T}^a$, is defined by $T^a_i := (1/2)\varepsilon^{ijk} T^a_{jk}$, it can be rewritten as

$$\begin{aligned} & j^{\bar{1}(1)}(\boldsymbol{R}) \\ & = -e \sum_n \int \frac{d^3\pi}{(2\pi)^3} \left(\boldsymbol{v}^n \cdot \boldsymbol{\Omega}^n \right) (eB_{\bar{1}} + T^a_{\bar{1}} \pi_a) n_F(\varepsilon_n) \\ & - \frac{e}{2} \sum_n \int \frac{d^3\pi}{(2\pi)^3} \Omega^n_a T^a_{\bar{1}} \varepsilon_n n_F(\varepsilon_n). \end{aligned} \tag{4.7.19}$$

It is noted that the term containing $B_{\bar{1}}$ is equal to the expression for the CME derived by Son and Yamamoto [59], and the others are new terms that represent the current induced by the torsion. Neglecting the last term, which is, as we will discuss later, less important than the others in the case of WSMs, Eq.(4.7.19) can also shortly derived from the substitution of the magnetic field or the field strength in the absence of the vielbein, $-\mathrm{i}[(-\mathrm{i}\partial_2 - eA_2), (-\mathrm{i}\partial_3 - eA_3)] = eB_1$ with the field strength in the presence of the vielbein, $-\mathrm{i}[-\mathrm{i}\nabla_{\bar{2}}, -\mathrm{i}\nabla_{\bar{3}}] = eB_{\bar{1}} + T^a_{\bar{1}}(-\mathrm{i}\nabla_a)$, where $[U, V] := UV - VU$ is the commutator. This justifies the analogy between the TMF and the magnetic field.

Finally, we substitute the energy, group velocity, and Berry curvature of the model of the WSM, (4.1.8), into Eq.(4.7.19) and derive Eq.(4.1.11). We characterize the four

bands of the Hamiltonian (4.1.8) as $n = (s, \pm)$, with $s = L$ or R, where s is the index of the chirality and $+(-)$ means the higher (lower) band of the Weyl cone. Then, their energy, group velocity, and Berry curvature are given by

$$\begin{aligned}
\varepsilon^{s,\pm}(\boldsymbol{k}) &= v_F\left[\pm|\boldsymbol{k}-\boldsymbol{\lambda}^s| - \lambda_0^s\right] \\
\boldsymbol{v}^{s,\pm}(\boldsymbol{k}) &= \pm\frac{v_F(\boldsymbol{k}-\boldsymbol{\lambda}^s)}{|\boldsymbol{k}-\boldsymbol{\lambda}^s|} \\
\boldsymbol{\Omega}^{s,\pm}(\boldsymbol{k}) &= \pm\chi_s\frac{\boldsymbol{k}-\boldsymbol{\lambda}^s}{2|\boldsymbol{k}-\boldsymbol{\lambda}^s|^3}.
\end{aligned} \tag{4.7.20}$$

Using Eqs.(4.7.19) and (4.7.20), we obtain

$$\begin{aligned}
&j^{\bar{1}(1)}(\boldsymbol{R}) \\
&= \left[\frac{e^2 v_F(\lambda_0^R - \lambda_0^L)}{4\pi^2}B_{\bar{1}}(\boldsymbol{R}) + \frac{e v_F(\lambda_a^R - \lambda_a^L)\Lambda}{4\pi^2}T^a_{\bar{1}}(\boldsymbol{R})\right],
\end{aligned} \tag{4.7.21}$$

at zero temperature and up to the linear order in $\lambda_\mu^{L(R)}$. For the derivation of Eq.(4.7.21), we introduced a momentum cutoff scheme $|\boldsymbol{k}-\boldsymbol{\lambda}^s| < \Lambda$ for the Weyl node of the chirality s. Physically, Λ corresponds to the momentum range from the Weyl points in which the cone structures of the band of the lattice system is approved. Note that the last term of Eq.(4.7.19) yields second(or more)-order contributions in $\lambda_\mu^{L(R)}$, and then less important as mentioned before. Eq.(4.7.21) is the correction of current due to the TMF and magnetic field and is equivalent to Eq.(4.1.11), then the derivation of Eq.(4.1.11) has been completed.

8 Appendix: Analytical calculation on ground state current in the presence of screw dislocation

In this section, we describe the details of the results on the properties of the wave functions of the electrons in WSMs in the presence of a screw dislocation and the derivation of the TCME from them, which are summarized in Sec.4.2. Here we calculate the ground state current raised by the TCME in the case of screw dislocation, by calculating directly the eigenstates of the Hamiltonian with the torsion. This is an alternative approach for the derivation of the TCME, which does not rely on Eq.(4.1.11).

For this purpose, we, first, analyze the spectrum of the Hamiltonian (4.2.1),

$$
\begin{aligned}
H^{\rm screw}_{s,k_z} &= \chi_s \left[H^{\perp}_{k_z} + m^s_{k_z} \sigma^z \right], \\
H^{\perp}_{k_z} &= \left(-{\rm i}\partial_x - \frac{\Phi_{k_z} y}{2\pi\rho^2} \right) \sigma^x + \left(-{\rm i}\partial_y + \frac{\Phi_{k_z} x}{2\pi\rho^2} \right) \sigma^y .
\end{aligned} \tag{4.8.1}
$$

where $m^s_{k_z} = k_z - \chi_s \lambda$, $\Phi_{k_z} = k_z b_g$, $\rho = \sqrt{x^2+y^2}$, $\chi_{L(R)} = +1(-1)$, and σ^i is the Pauli matrix.

For the calculation of the spectrum, it is useful to clarify the symmetry of the eigenstates of $H^{\perp}_{k_z}$. Suppose $|\kappa\rangle_{k_z}$ the eigenstate of $H^{\perp}_{k_z}$ with eigenvalue κ. Since $\{H^{\perp}_{k_z}, \sigma^z\} = 0$, where $\{U, V\} := UV + VU$ is the anticommutator, the state $\sigma^z |\kappa\rangle_{k_z}$ is also the eigenstate with eigenvalue $-\kappa$. Therefore, we can choose the eigenfunctions to preserve the doublet structure,

$$
|-\kappa\rangle_{k_z} = \sigma^z |\kappa\rangle_{k_z} , \tag{4.8.2}
$$

for $\kappa \neq 0$. On the other hand, there is no double structure in the zero eigenstates. Since the hermitian operator σ^z maps zero eigenstates of $H^{\perp}_{k_z}$ to zero eigenstates of $H^{\perp}_{k_z}$, then we can choose the zero eigenstates also as eigenstates of σ^z, denoted by $|0_{i,\sigma_i}\rangle_{k_z}$ with $\sigma^z |0_{i,\sigma_i}\rangle_{k_z} = \sigma_i |0_{i,\sigma_i}\rangle_{k_z}$ and $\sigma_i = \pm 1$. There is another symmetrical property between the eigenstates of $H^{\perp}_{k_z}$ with different k_z. Since the transformation $k_z \to -k_z$ corresponds to the flip of the direction of the effective magnetic field,

$$
\Theta H^{\perp}_{k_z} \Theta^{-1} = H^{\perp}_{-k_z} \tag{4.8.3}
$$

holds, where $\Theta = {\rm i}\sigma^y K$ is the time-reversal operator for spin-1/2 fermions and K is the complex conjugation operator [84]. Therefore we can impose $|\kappa\rangle_{-k_z} = \Theta |\kappa\rangle_{k_z}$ and $|0_{i,-\sigma_i}\rangle_{-k_z} = \Theta |0_{i,\sigma_i}\rangle_{k_z}$, because of $\{\sigma^z, \Theta\} = 0$.

The eigenstates of $H^{\rm screw}_{s,k_z}$ can be constructed from $|\kappa\rangle_{k_z}$ and $|0_{\sigma_i}\rangle_{k_z}$. Indeed,

$$
|\psi^{L,\pm}_{k_z}(\kappa)\rangle := c^{L,\pm}_{k_z,1}(\kappa) |\kappa\rangle_{k_z} + c^{L,\pm}_{k_z,2}(\kappa) |-\kappa\rangle_{k_z} , \tag{4.8.4}
$$

with $\kappa > 0$, and $|0_{\sigma_i}\rangle_{k_z}$ are the full spectrum of $H^{\rm screw}_{L,k_z}$, with eigenvalues $\pm\sqrt{\kappa^2 + (m^L_{k_z})^2}$ and $\sigma_i m^L_{k_z}$, respectively. Here the coefficients are given by

$$
\begin{aligned}
c^{L,\pm}_{k_z,1}(\kappa) =& \frac{\pm {\rm sgn}(m^L_{k_z}) \left[(\kappa^2 + (m^L_{k_z})^2)^{1/2} \pm \kappa \right]^{1/2}}{(4(\kappa^2 + (m^L_{k_z})^2))^{1/4}}, \\
c^{L,\pm}_{k_z,2}(\kappa) =& \frac{\left[\kappa^2 + (m^L_{k_z})^2)^{1/2} \mp \kappa \right]^{1/2}}{(4(\kappa^2 + (m^L_{k_z})^2))^{1/4}}.
\end{aligned} \tag{4.8.5}
$$

Moreover, $|\psi^{R,\pm}_{k_z}(\kappa)\rangle := \Theta\,|\psi^{L,\mp}_{-k_z}(\kappa)\rangle$ and $|0_{\sigma_i}\rangle_{k_z}$ are the eigenstates of $H^{\rm screw}_{R,k_z}$, with eigenvalues $\pm\sqrt{\kappa^2+(m^R_{k_z})^2}$ and $-\sigma_i m^R_{k_z}$, respectively.

Now, we calculate the ground state current in the presence of the screw dislocation. As yet, we have not distinguished discrete and continuum states. From now on, we use κ_i to express the discrete eigenvalues of $H^{\perp}_{k_z}$ and (κ, l) to label the continuum states, where κ is the continuum energy eigenvalue, and l is a discrete quantum number, e.g., the angular momentum. The current operator is defined by

$$\frac{\partial H^{\rm screw}_{s,k_z}}{\partial k_z} = \chi_s\sigma^z + \chi_s\left[-\frac{b_g y}{2\pi\rho^2}\sigma^x + \frac{b_g x}{2\pi\rho^2}\sigma^y\right]. \tag{4.8.6}$$

At least up to the first order in b_g, the correction to the current operator due to the dislocation, i.e. the second and third term above, does not contribute to the expectation value because these terms are odd under the transformation $x \to -x$ or $y \to -y$. Therefore, the current is the sum of the expectation values of $\chi_s\sigma^z$ for the occupied states which consist of discrete nonzero, discrete zero, and continuum states, and then we obtain,

$$\begin{aligned} J^z = &\sum_{s=L,R}\int_{|m^s_{k_z}|<\Lambda}\frac{L_z dk_z}{2\pi}\left[\sum_{\kappa_i>0}\langle\psi^{s,-}_{k_z}(\kappa_i)|\chi_s\sigma^z|\psi^{s,-}_{k_z}(\kappa_i)\rangle\right. \\ &+\sum_{i:\sigma_i\chi_s m^s_{k_z}<0}\langle 0_{i,\sigma_i}|\chi_s\sigma^z|0_{i,\sigma_i}\rangle_{k_z} \\ &\left.+\int_0^\infty d\kappa\sum_l\langle\psi^{s,-}_{k_z}(\kappa,l)|\chi_s\sigma^z|\psi^{s,-}_{k_z}(\kappa,l)\rangle\right] \\ =&\int_{|m^L_{k_z}|<\Lambda}\frac{L_z dk_z}{2\pi}\left[\sum_{\kappa_i\neq 0}\langle\kappa_i|\sigma^z|\kappa_i\rangle_{k_z}\right. \\ &\left.+\sum_i\langle 0_{i,\sigma_i}|\sigma^z|0_{i,\sigma_i}\rangle_{k_z}+\int_{-\infty}^{\infty}d\kappa\sum_l\langle\kappa,l|\sigma^z|\kappa,l\rangle_{k_z}\right], \end{aligned} \tag{4.8.7}$$

where L_z is the size of the system. Here we introduce the momentum cutoff scheme, $|m^s_{k_z}| < \Lambda$, i.e. the domain of the integration is the same as that used in the calculation of Eq.(4.2.1). The first term in the square braket is equal to zero, since $\sigma^z\,|\kappa_i\rangle_{k_z} = |-\kappa_i\rangle_{k_z}$ is orthogonal to $|\kappa_i\rangle_{k_z}$. The second term is the index of the Dirac operator, $H^{\perp}_{k_z}$, which is an integer and the difference in the number of its normalizable zero modes with $\sigma^3 = +1$ and $\sigma^3 = -1$. The index is given by

$$N_{k_z} := -{\rm sgn}(\Phi_{k_z})\left\lfloor\frac{|\Phi_{k_z}|}{2\pi}\right\rfloor \tag{4.8.8}$$

[65, 66]. The normalizable zero modes exhibit power-law decay for large distance from the dislocation; i.e. they behave like

$$|0_{i,-1}\rangle \propto \left(0, \frac{(x-\mathrm{i}y)^{i-1}}{\rho^{\Phi_{k_z}/2\pi}}\right), \tag{4.8.9}$$

for $\Phi_{k_z} > 0$, and

$$|0_{i,+1}\rangle \propto (\rho^{\Phi_{k_z}/2\pi}(x+\mathrm{i}y)^{i-1}, 0), \tag{4.8.10}$$

for $\Phi_{k_z} < 0$, where $i = 1, 2, \cdots, |N_{k_z}|$ [65, 66]. Now, we move on to the third term of Eq.(4.8.7). One may expect that it is equal to zero, since $\sigma^z |\kappa, l\rangle = |-\kappa, l\rangle$, is orthogonal to $|\kappa, l\rangle$ for almost all values of κ. However, the scattering states near $\kappa = 0$ (their amplitudes $\propto \cos(\kappa\rho + \delta_l)/\sqrt{\rho}$ with δ_l the phase shift) cause a delta function peak of $\langle \kappa, l|\sigma^z|\kappa, l\rangle_{k_z}$ at $\kappa = 0$. Indeed, from an explicit calculation [65], it has been shown that

$$\sum_l \langle \kappa, l|\sigma^z|\kappa, l\rangle_{k_z} = c_{k_Z}\delta(\kappa), \tag{4.8.11}$$

with

$$c_{k_z} = \frac{\Phi_{k_z}}{2\pi} - N_{k_z}, \tag{4.8.12}$$

and then the third term is equal to c_{k_z}. Substituting them into Eq.(4.8.7), we obtain

$$J^z = \int_{-\Lambda-\lambda}^{\Lambda-\lambda} \frac{L_z dk_z}{2\pi}\frac{\Phi_{k_z}}{2\pi} = -\frac{L_z b_g \Lambda\lambda}{2\pi^2}, \tag{4.8.13}$$

which is coincident with the expression obtained directly from Eq.(4.1.11) by the following reason. In the presence of the screw dislocation with the Burgers vector $-b_g\hat{z}$ the torsion is given by $T^z_z = T^z_{xy} = b_g\delta^{(2)}(x, y)$. Therefore, the total current derived from Eq.(4.1.11) is $J^z = -L_z e v_F(\lambda^R_z - \lambda^L_z)\Lambda b_g/4\pi^2$. In this section we have set $\lambda^L_z = -\lambda^R_z = \lambda$ and $e = v_F = 1$, and therefore we obtain $J^z = -L_z\lambda\Lambda b_g/2\pi^2$, which reproduces Eq.(4.8.13).

Chapter 5

Conclusion

This thesis reported theoretical studies on geometrical responses in topological materials. In this chapter we summarize this thesis.

In Chapter 1, we introduced topological materials: two-dimensional topological superconductors (TSCs) with broken time-reversal-symmetry and Weyl semimetals and superconductors (WSMs and WSCs). The energy spectra of these TSCs are fully gapped and they are characterized by the first Chern number. These points are similar to the case of Chern insulators. However unlike Chern insulators, they do not preserve the charge number and then the electromagnetic responses can hardly grasp their topological features. Therefore, we discussed thermal transport phenomena in Chapter 3. WSMs have one or more pairs of Weyl nodes in the Brillouin zones. A Weyl node is protected by the Chern number and cannot be gapped out by weak perturbations. We introduced exotic transport phenomena associated with the chiral anomaly in WSMs: the anomalous Hall effect, chiral magnetic effect, and negative longitudinal magnetoresistance. The chiral magnetic effect is the generation of a ground state current parallel to an applied magnetic field even in the absence of electric field. The theories on this effect contain subtle points: although, based on the linearized effective model for WSMs, this effect can be derived, it is proved that the net ground current is always zero in realistic lattice systems owing to the periodicity of spectrum in the Brillouin zones.

Chapter 2 is dedicated to the introduction of the theory of the differential geometry and its applications to condensed matter systems, especially topological systems. We introduced the concepts of the vielbeins and torsions. The vielbeins are more fundamental quantities that characterizes the curved space-time than the Riemannian metrics. The

torsions are the rotation of the vielbeins and then can be considered as field strengths or electromagnetic fields, while the vielbeins are vector potentials. Furthermore we showed that the theory of the differential geometry is useful for the descriptions of various condensed matter responses which are caused by applying a temperature gradient, twisting the sample, and making dislocations. We also introduced its applications to topological systems: two-dimensional TSCs with broken time-reversal-symmetry, Chern insulators, and WSMs. Here we introduced the theories on the thermal Hall effect in two-dimensional TSCs with broken time-reversal-symmetry. From the theories based on the chiral Majorana edge modes, it had been shown that the thermal Hall coefficient is quantized. However, there was no bulk linear response theory or bulk effective field theory that leads to this quantization. It is because that the formulation of the linear response theory for the thermal Hall effect has intricate points and the gravitational Chern-Simons action, which is the bulk effective action for two-dimensional TSCs, is of too high order in derivatives of the Riemannian metric to describe the thermal Hall effect. We also introduced the viscoelastic responses in Chern insulators and WSMs, based on the topological actions derived from the torsional chiral anomaly. In the presence of the torsions the effective action for Chern insulators is the torsional Chern-Simons action and from this action we can obtain the Hall viscosity, which is the generation of a dissipationless momentum current by shearing, rotating, or twisting the sample. On the other hand, that for WSMs is the torsional θ-term. From this action, we can derive the Hall viscosity and chiral heat effect. However, these viscoelastic responses can be hardly observed in experiments, since the momentum is not preserved in realistic lattice systems owing to broken translation symmetry.

In Chapter 3, we discussed the thermal Hall effect in superconductors with broken time-reversal-symmetry, including two-dimensional TSCs in the previous chapter as a special case. As described in the previous chapter, in previous studies the quantization of the thermal Hall effect in two-dimensional TSCs had been derived only from edge approaches but not from bulk approaches. The edge approaches are based on the chiral Majorana modes. Then, they work in the low temperature limit and for fully gapped systems. On the other hand, in this chapter, we studied the thermal Hall effect from the bulk linear response theory and derived the exact formula for the thermal Hall coefficient that is applicable to any superconductors with broken time-reversal-symmetry at finite temperature even when the superconductors have nodes.

In Chapter 4, we discussed a new torsional response in WSMs, referred to as the torsional chiral magnetic effect (TCME). As mentioned above, theoretical studies had revealed various types of viscoelastic responses due to topological actions associated with torsions. However they can be hardly observed in experiments owing to broken translation symmetry. On the other hand, the TCME is the generation of a current by a lattice dislocation, then can be detected in realistic systems. We investigated this effect from three approaches. First we argued the torsional responses in WSMs from the linear response theory based on a low-energy effective model of WSMs coupled with the vielbeins and $U(1)$-vector potentials. We discovered two types of torsional responses, of which physical interpretations are the generations of currents by edge and screw dislocations. Second we analytically calculated the ground state wave function in the presence of a screw dislocation. We showed that the asymmetric chiral modes localized along the dislocation line due to the parity anomaly are the origin of the TCME, i.e. the ground state current in the presence of the dislocation. Finally we performed a numerical calculation based on a tight-binding model of a WSM with screw dislocations. Here we showed that the asymmetric spectrum is realized even in lattice models, and the ground state current occurs. Therefore we establish that the TCME is possible in realistic solid state systems. We also discussed the no-go theorem of the chiral magnetic effect, and showed that the TCME avoids this theorem since it is the generation of a local current, which is not prohibited by this theorem. Finally, we proposed experimental setups for the detection of the TCME.

Bibliography

[1] A. P. Schnyder, S. Ryu, A. Furusaki, and A. W. W. Ludwig, Phys. Rev. B **78**, 195125 (2008).

[2] D. J. Thouless, M. Kohmoto, M. P. Nightingale, and M. den Nijs, Phys. Rev. Lett. **49**, 405 (1982).

[3] A. P. Mackenzie and Y. Maeno, Rev. Mod. Phys. **75**, 657 (2003).

[4] G. E. Volovik, *The Universe in a Helium Droplet* (Oxford University Press, 2003).

[5] G. Moore and N. Read, Nuclear Physics B **360**, 362 (1991).

[6] M. Sato, Y. Takahashi, and S. Fujimoto, Phys. Rev. Lett. **103**, 020401 (2009).

[7] M. Sato and S. Fujimoto, Phys. Rev. B **79**, 094504 (2009).

[8] M. Sato, Y. Takahashi, and S. Fujimoto, Phys. Rev. B **82**, 134521 (2010).

[9] H. Nielsen and M. Ninomiya, Nuclear Physics B **185**, 20 (1981).

[10] H. Nielsen and M. Ninomiya, Nuclear Physics B **193**, 173 (1981).

[11] K. Fujikawa and H. Suzuki, *Path Integrals and Quantum Anomalies* (Oxford University Press, 2004).

[12] Q. Li, D. E. Kharzeev, C. Zhang, Y. Huang, I. Pletikosic, A. V. Fedorov, R. D. Zhong, J. A. Schneeloch, G. D. Gu, and T. Valla, Nat Phys **12**, 550 (2016).

[13] D. E. Kharzeev, Progress in Particle and Nuclear Physics **75**, 133 (2014).

[14] K. Fukushima, D. E. Kharzeev, and H. J. Warringa, Phys. Rev. D **78**, 074033 (2008).

[15] F. Wilczek, Phys. Rev. Lett. **109**, 160401 (2012).

[16] M. M. Vazifeh and M. Franz, Phys. Rev. Lett. **111**, 027201 (2013).

[17] N. Yamamoto, Phys. Rev. D **92**, 085011 (2015).

[18] A. A. Zyuzin and A. A. Burkov, Phys. Rev. B **86**, 115133 (2012).

[19] Y. Ibe and H. Sumiyoshi, arXiv:1605.04567 (2016).

[20] H. Sumiyoshi and S. Fujimoto, Phys. Rev. Lett. **116**, 166601 (2016).

[21] H. Nielsen and M. Ninomiya, Physics Letters B **130**, 389 (1983).

[22] H.-J. Kim, K.-S. Kim, J.-F. Wang, M. Sasaki, N. Satoh, A. Ohnishi, M. Kitaura, M. Yang, and L. Li, Phys. Rev. Lett. **111**, 246603 (2013).

[23] F. Arnold, C. Shekhar, S.-C. Wu, Y. Sun, R. D. dos Reis, N. Kumar, M. Naumann, M. O. Ajeesh, M. Schmidt, A. G. Grushin, et al., Nature Communications **7**, 11615 EP (2016).

[24] P. Goswami, J. H. Pixley, and S. Das Sarma, Phys. Rev. B **92**, 075205 (2015).

[25] X. Huang, L. Zhao, Y. Long, P. Wang, D. Chen, Z. Yang, H. Liang, M. Xue, H. Weng, Z. Fang, et al., Phys. Rev. X **5**, 031023 (2015).

[26] N. W. Ashcroft and N. D. Mermin, *Solid state physics* (Thomson Learning, 2005).

[27] D. T. Son and B. Z. Spivak, Phys. Rev. B **88**, 104412 (2013).

[28] E. R. Schemm, R. E. Baumbach, P. H. Tobash, F. Ronning, E. D. Bauer, and A. Kapitulnik, Phys. Rev. B **91**, 140506 (2015).

[29] T. Yamashita, Y. Shimoyama, Y. Haga, T. Matsuda, E. Yamamoto, Y. Onuki, H. Sumiyoshi, S. Fujimoto, A. Levchenko, T. Shibauchi, et al., Nature Physics **11**, 17 (2015).

[30] H. Sumiyoshi and S. Fujimoto, Phys. Rev. B **90**, 184518 (2014).

[31] M. Nakahara, *Geometry, topology, and physics* (Institute of Physics Publishing, Bristol, Philadelphia, 2003).

[32] A. Shitade, Progress of Theoretical and Experimental Physics **2014**, 123I01 (2014).

[33] O. Parrikar, T. L. Hughes, and R. G. Leigh, Phys. Rev. D **90**, 105004 (2014).

[34] J. M. Luttinger, Phys. Rev. **135**, A1505 (1964).

[35] B. Bradlyn and N. Read, Phys. Rev. B **91**, 125303 (2015).

[36] Y. Hidaka, Y. Hirono, T. Kimura, and Y. Minami, Progress of Theoretical and Experimental Physics **2013** (2013).

[37] T. L. Hughes, R. G. Leigh, and O. Parrikar, Phys. Rev. D **88**, 025040 (2013).

[38] A. Shitade and T. Kimura, Phys. Rev. B **90**, 134510 (2014).

[39] T. L. Hughes, R. G. Leigh, and E. Fradkin, Phys. Rev. Lett. **107**, 075502 (2011).

[40] N. Read and D. Green, Phys. Rev. B **61**, 10267 (2000).

[41] N. Nagaosa, J. Sinova, S. Onoda, A. H. MacDonald, and N. P. Ong, Rev. Mod. Phys. **82**, 1539 (2010).

[42] F. D. M. Haldane, Phys. Rev. Lett. **61**, 2015 (1988).

[43] C. G. Callan and J. A. Harvey, Nuclear Physics B **250**, 427 (1985).

[44] L. Smrcka and P. Streda, Journal of Physics C: Solid State Physics **10**, 2153 (1977).

[45] L. Alvarez-Gaum é and E. Witten, Nuclear Physics B **234**, 269 (1984).

[46] T. Giamarchi, *Quantum physics in one dimension* (Oxford university press, 2004).

[47] J. E. Avron, R. Seiler, and P. G. Zograf, Phys. Rev. Lett. **75**, 697 (1995).

[48] H. T. Nieh and M. L. Yan, Journal of Mathematical Physics **23**, 373 (1982).

[49] O. Chandia and J. Zanelli, Phys. Rev. D **55**, 7580 (1997).

[50] T. Kimura and T. Nishioka, Progress of Theoretical Physics **127**, 1009 (2012).

[51] K. Nomura, S. Ryu, A. Furusaki, and N. Nagaosa, Phys. Rev. Lett. **108**, 026802 (2012).

[52] T. Qin, Q. Niu, and J. Shi, Phys. Rev. Lett. **107**, 236601 (2011).

[53] H. Sumiyoshi and S. Fujimoto, J. Phys. Soc. Jpn. **82**, 023602 (2013).

[54] A. Altland and M. R. Zirnbauer, Phys. Rev. B **55**, 1142 (1997).

[55] M. Kohmoto, Ann. Phys. (N.Y.) **160**, 343 (1985).

[56] G. E. Volovik, *The Universe in a Helium Droplet* (Clarendon Press, 2003).

[57] T. Thonhauser, D. Ceresoli, D. Vanderbilt, and R. Resta, Phys. Rev. Lett. **95**, 137205 (2005).

[58] D. Xiao, J. Shi, and Q. Niu, Phys. Rev. Lett. **95**, 137204 (2005).

[59] D. T. Son and N. Yamamoto, Phys. Rev. Lett. **109**, 181602 (2012).

[60] M. Kohmoto, B. I. Halperin, and Y.-S. Wu, Phys. Rev. B **45**, 13488 (1992).

[61] J. C. Y. Teo and C. L. Kane, Phys. Rev. B **82**, 115120 (2010).

[62] D. Edelen and D. Lagoudas, *Gauge theory and defects in solids* (North Holland, 1988).

[63] K.-I. Imura and Y. Takane, Phys. Rev. B **84**, 245415 (2011).

[64] R. Jackiw, Phys. Rev. D **29**, 2375 (1984).

[65] J. Kiskis, Phys. Rev. D **15**, 2329 (1977).

[66] Y. Aharonov and A. Casher, Phys. Rev. A **19**, 2461 (1979).

[67] S. Murakami, N. Nagaosa, and S.-C. Zhang, Phys. Rev. B **69**, 235206 (2004).

[68] A. B. Sushkov, J. B. Hofmann, G. S. Jenkins, J. Ishikawa, S. Nakatsuji, S. Das Sarma, and H. D. Drew, Phys. Rev. B **92**, 241108 (2015).

[69] S. Borisenko, D. Evtushinsky, Q. Gibson, A. Yaresko, T. Kim, M. N. Ali, B. Büchner, M. Hoesch, and R. J. Cava, arXiv: 1507.04847 (2015).

[70] D. Vasyukov, Y. Anahory, L. Embon, D. Halbertal, J. Cuppens, L. Neeman, A. Finkler, Y. Segev, Y. Myasoedov, M. L. Rappaport, et al., Nat Nano **8**, 639 (2013).

[71] Y. H. Wang, J. R. Kirtley, F. Katmis, P. Jarillo-Herrero, J. S. Moodera, and K. A. Moler, Science **349**, 948 (2015).

[72] Z. S. Basinski and J. S. Dugdale, Phys. Rev. B **32**, 2149 (1985).

[73] P. L. McEuen, A. Szafer, C. A. Richter, B. W. Alphenaar, J. K. Jain, A. D. Stone, R. G. Wheeler, and R. N. Sacks, Phys. Rev. Lett. **64**, 2062 (1990).

[74] J. K. Wang and V. J. Goldman, Phys. Rev. Lett. **67**, 749 (1991).

[75] J. Bardeen and W. Shockley, Phys. Rev. **80**, 72 (1950).

[76] S. C. Hunter and F. R. N. Nabarro, Proc. Roy. Soc. London A **220**, 542 (1953).

[77] Z. S. Basinski, J. S. Dugdale, and A. Howie, Phil. Mag. **8**, 1989 (1963).

[78] B. R. Watts, in *Basic Problems and Applications, volume 8 of Dislocations in Solids,* edited by F. R. N. Nabarro (North-Holland, 1989).

[79] B. R. Watts, J. Phys. F: Met. Phys. **18**, 1183 (1988).

[80] A. Bergmann, M. Kaveh, and N. Wiser, Phys. Rev. B **24**, 6807 (1981).

[81] A. U. Kasumov, C. H. V. Kopetskii, L. S. Kokhanchik, and V. N. Matveev, Sov. Phys. Solid State **23**, 151 (1981).

[82] A. S. Karolik and A. A. Luhvich, J. Phys.: Condensed Matter **6**, 873 (1994).

[83] K. Viswanathan and S. Chandrasekar, J. Appied Phys. **116**, 245103 (2014).

[84] J. J. Sakurai and J. J. Napolitano, *Modern Quantum Mechanics* (Addison-Wesley, 2010), 2nd ed.

Acknowledgment

First, I would like to express my sincere gratitude to my supervisor Prof. Satoshi Fujimoto for his continuous guidance and encouragement during my graduate course. Whenever I visited his office, he was always willing to spend time for discussions and gave me instructive and crucial advices, which were greatly helpful for my Ph.D project. I would like to thank Dr. Ken Shiozaki for helpful discussions. Due to his deep and broad knowledge on topological materials, I learned a lot from him. I would also like to thank Dr. Atsuo Shitade and Prof. Taro Kimura. They are two of the pioneers of the geometrical responses in condensed-matter contexts and my latest work in this thesis was in part motivated by discussions with them. I am deeply grateful to Prof. Shinsei Ryu for hosting my visit to the University of Illinois at Urbana-Champaign. It was stimulating to discuss on theories of topological phases with him and members of his group, where this topic was actively studied. I would like to thank Takuya Yamashita, Prof. Yuji Matsuda, and Prof. Takasada Shibauchi for the collaboration in the study on thermoelectric properties of the exotic superconductor. I am honored to contribute to this experimental project as a theorist.

I would like to thank the present and former faculty members in the condensed matter theory group at Kyoto University, Prof. Norio Kawakami, Prof. Ryusuke Ikeda, Prof. Hiroaki Ikeda, Prof. Youichi Yanase, Prof. Robert Peters, Prof. Masaki Tezuka, and Prof. Kazushi Aoyama for their support and guidance in various academic matters. Owing to my friends and colleagues, the five years I spent were comfortable and enjoyable. I am especially grateful to the colleagues, Kyosuke Adachi, Yuichiro Dan, Yohei Ibe, Koudai Iwahori, Fuyuki Matsuda, Masaya Nakagawa, Yasuharu Nakamura, Dr. Kazuto Noda, Takuya Nomoto, Dr. Masaru Sakaida, Prof. Yasuhiro Tada, Kazuaki Takasan, Rina Takashima, and Dr. Tsuneya Yoshida, and the friends in other groups, Takahiro M. Doi, Sho Fujibayashi, Souichiro Mohri, Kenta Moriyama, Takuei Nishio, Tokiro Numasawa, Yu Terada, and Shoichiro Tsutsui.

Over the past three years, I have been financially supported by Grant-in-Aid for Japan Society for the Promotion of Science (JSPS) fellows. I sincerely thank this financial support, without which I would not achieve the results reported in this thesis.

Finally, I would like to thank my parents and grandparents, Makoto Sumiyoshi, Mikiko Sumiyoshi, Kenzo Joso, Kiyoko Sumiyoshi, Yoshiko Joso, and the late Masuo Sumiyoshi, who supported my career in numerous ways.